ESTIMATION AND MITIGATION
OF UNMODELED ERRORS FOR A
PSEUDOLITE BASED REFERENCE SYSTEM

THESIS

Jeremiah A. Shockley, Captain, USAF

AFIT/GE/ENG/06-51

DEPARTMENT OF THE AIR FORCE
AIR UNIVERSITY

AIR FORCE INSTITUTE OF TECHNOLOGY

Wright-Patterson Air Force Base, Ohio

AFIT/GE/ENG/06-51

ESTIMATION AND MITIGATION OF UNMODELED ERRORS FOR A PSEUDOLITE BASED REFERENCE SYSTEM

THESIS

Presented to the Faculty

Department of Electrical and Computer Engineering

Graduate School of Engineering and Management

Air Force Institute of Technology

Air University

Air Education and Training Command

In Partial Fulfillment of the Requirements for the

Degree of Master of Science in Electrical Engineering

Jeremiah A. Shockley, B.S.E.E.

Captain, USAF

March 2006

AFIT/GE/ENG/06-51

ESTIMATION AND MITIGATION OF UNMODELED ERRORS FOR A PSEUDOLITE BASED REFERENCE SYSTEM

Jeremiah A. Shockley, B.S.E.E.

Captain, USAF

Approved:

_____   _____
Doctor John F. Raquet   3 MAR 06
Thesis Advisor   date
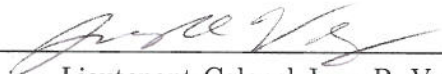
_____   _____
Doctor Peter S. Maybeck   1 mar 06
Committee Member   date

_____   _____
Lieutenant Colonel Juan R. Vasquez   1 Mar 06
Committee Member   date

AFIT/GE/ENG/06-51

Abstract

Current flight reference systems rely heavily on the Global Positioning System (GPS), causing susceptibility to GPS jamming. Additionally, an increasing number of tests involve jamming the GPS signal. A need exists to develop a system capable of GPS-level accuracy during these outages. One promising solution is a ground-based pseudolite system capable of delivering sub-centimeter level accuracy, yet operating at non-GPS frequencies. This thesis attempts to determine the unknown errors in the *Locata* system, one such pseudolite-based system, to achieve the accuracy required.

The development of a measurement simulation tool along with a Kalman filter algorithm provides confirmation of filter performance as well as the ability to process real data measurements and evaluate simulated versus real data comparatively. The simulation tool creates various types of measurements with induced noise, tropospheric delays, pseudolite position errors, and tropospheric scale-factor errors. In turn, the Kalman filter resolves these errors, along with position, velocity, and acceleration for both simulated and real data measurements, enabling error analysis to pinpoint both expected and unexpected error sources.

Simulated results confirmed the ability to render centimeter level solutions in a noisy environment, proper pseudolite position error estimation, and suitable tropospheric scale-factor estimation. Additionally, the simulation demonstrated the inability to conduct simultaneous estimation of both the pseudolite position errors and the tropospheric scale-factor.

Real data results indicate the algorithm renders a highly accurate (6cm) position solution after applying the low elevation tropospheric delay model substantiated in this thesis. Furthermore, the ability to resolve the pseudolite position errors and tropospheric scale-factor provide mitigation of previously unmodeled errors, and highlight the fact additional errors exist, which remain undetermined.

Acknowledgements

I would like to express my sincere appreciation to my faculty advisor, Dr. John Raquet, for his guidance and support throughout the course of this thesis effort. The insight and experience was certainly appreciated.

I also need to thank God for help in my daily struggle, my wife for her countless hours of support, and my daughter for having an understanding far beyond a normal eight year old. I plan to repay their time sacrifice with interest.

Jeremiah A. Shockley

Table of Contents

List of Figures

xi

xiii

List of Tables

ESTIMATION AND MITIGATION
OF UNMODELED ERRORS FOR A
PSEUDOLITE BASED REFERENCE SYSTEM

I. Introduction

1.1   Background

Pseudolite (or pseudo-satellite) applications have long been a background partner in navigation systems providing augmentation or assistance when needed. Many studies [8, 11, 14, 25] develop useful indoor and outdoor applications for pseudolites, yet none have become the frontrunner in the navigation field filled with legacy systems such as Very high frequency Omnidirectional Range (VOR) and LOng RAnge Navigation (LORAN-C), and dominated by the Global Positioning System (GPS). However, severe limitations prevent a single system from achieving both accuracy and robustness. Legacy systems linger on due to reliability and resistance to jamming, yet do not provide the accuracy of GPS. In turn, GPS is easily jammed and may provide poor quality solutions depending on location and geometry. An advanced navigation system is needed to both verify and to supplant GPS when dependable accuracy is required.

One of the most advanced navigation systems is the modern flight reference system operated by the 746th Test Squadron, Holloman AFB, NM, which is used to test and evaluate new flight navigation systems [6]. To be useful, a flight reference system should have an order of magnitude greater accuracy than the system under test, because the output from the reference system is regarded as the truth. Any degradation in reference system performance will invalidate the evaluation of the system under test. The flight reference system has evolved through the years from radar tracking, ground-based camera and aircraft transponders, to the current system

of differential GPS (DGPS) integrated with an inertial unit, barometric altimeter, and a ground transponder/interrogator system. The current reference system used by the 746th Test Squadron's Central Inertial Guidance Test Facility (CIGTF) is called the CIGTF Post-processing System (CPS) [6].

CPS currently faces two challenges: accuracy during periods of GPS jamming and accuracy when a GPS signal is available. Operation in the presence of GPS signal interference impedes CPS from using its most accurate sensor. When jamming denies CPS from using GPS measurements, it must rely on its other sensors, primarily the INS. INS accuracy degrades over time, causing the performance of CPS to suffer. Although post-processing techniques are applied to reduce the impact of INS errors, CPS cannot maintain centimeter level accuracy during periods of GPS jamming. The second challenge facing CPS is accuracy when GPS is available. As new systems become more accurate, CPS must also improve its accuracy to be a useful reference.

One technology potentially solving the challenges of reference system accuracy is the use of *LocataLites* [3]. The *LocataLite* term signifies the common term used throughout this research for pseudolites specifically created by the *Locata* Corporation. *LocataLites* are ground-based transmitters sending GPS-like signals which can be received with GPS receivers adapted for *LocataLite* signals, called a *Locata* [3]. *LocataLites* differ from standard pseudolites due to the inclusion of sophisticated transmission algorithms. *LocataLites* possess the flexibility of operating at various frequencies, allowing them to avoid GPS jamming signals.

Aiding with *LocataLites* potentially increases the accuracy of CPS or other flight reference systems when GPS jamming signals are present, and also during periods of normal GPS operation. More importantly, *LocataLites* potentially can provide CPS with a navigation source that maintains centimeter-level positioning accuracies during periods of GPS jamming. The increase in accuracy during normal (non-jamming) GPS operation is the result of CPS having access to two highly accurate sensors, as compared to just one when *LocataLites* are not used. A system that uses two sensors

with roughly the same accuracy can expect to see a $1/\sqrt{2}$ factor improvement in accuracy over just using one sensor. That is nearly a 30 percent improvement, assuming that both sensors are independent. The errors between GPS and *LocataLite* signals are not completely independent, but a practical system would still show substantial improvement over DGPS only navigation.

1.2   Problem Definition

The primary goal of this thesis is to estimate previously unmodeled errors in a ground based *LocataLite* system, specifically targeting low elevation tropospheric conditions and *LocataLite* position errors in order to obtain a position accuracy equivalent to or better than current DGPS accuracy. The primary application is to improve both the accuracy and robustness to jamming of a flight reference system with the inclusion of a *LocataLite* network, called a *LocataNet*.

1.3   Related Research

1.3.1   Pseudolite History.   Stone et al. [26] discusses the origins of the pseudolite and the many variations falling under the term pseudolite. One of the first projects known as the Integrity Beacon Landing System (IBLS) utilized two pseudolites to resolve carrier-phase DGPS integers for auto-landing aircraft. The project introduced many terms including: integrity beacons, Doppler marker, and simple pseudolite. The project also tested a pseudolite transceiver dubbed the synchrolite (originally known as the omni-marker). Further development led to the Local Area Augmentation System (LAAS) and pseudolites positioned at airports became Airport Pseudolites or APLs (commonly referred to as "apples"). The author also discusses potential uses for pseudolites such as open pit mining, Mars exploration, and formation flying spacecraft.

The term pseudolite originally referred to any device transmitting GPS satellite-like signals. However with the advent of new coding methods, pulsing schemes, and frequency plans, pseudolite signals become less like satellite signals everyday. For

navigation purposes the pseudolite signal intentionally differs from the GPS signal to prevent jamming and cross-correlation.

1.3.2 Pseudolite Navigation. Raquet et al. [25] conducted an early test of a pseudolite only flight reference system. This work was accomplished at Holloman AFB under the partnership of the 746th Test Squadron, NovAtel Communications, Stanford Telecom, and the University of Calgary. It involved an "inverted" mode of operation in which the position of the pseudolite is solved in relation to an array of five stationary Novatel receivers placed at known locations (via GPS) and one stationary Novatel PC card receiver with a laptop computer. The Stanford Telecom pseudolite transmitters comprised the fixed and mobile pseudolites transmitting on L1 using PRN 10 and PRN 8 Gold codes. The testing utilized two methods of testing known as pseudolite positioning with satellite reference (PPSR) and pseudolite positioning with pseudolite reference (PPPR). PPSR positioning comprises double differencing between two transmitters, the mobile pseudolite and a GPS satellite as the reference transmitter (analogous to the reference receiver in a typical case of relative positioning between two receivers). PPPR uses the same format, except the reference transmitter is a fixed pseudolite instead of a GPS satellite. Both methods utilized the same set of data collected in calculating solutions. This particular testing marked the first time the pseudolite itself was positioned using carrier-phase data in a double-differenced mode. Ambiguities were resolved to floating point with attempts at integer ambiguity resolution resulting in poorer solutions. A more thorough explanation of floating-point versus integer amiguities is in Section 2.4.7. This proof-of-concept addressed the many facets of pseudolite navigation in a novel new approach. The overall results showed double-differenced carrier-phase measurements with floating point ambiguity provided a position solution with accuracies on the order of 10-30cm [25].

NovAtel Communications and Stanford Telecom continued work with pseudolite navigation by conducting a follow-on test to duplicate some of the results from the

Holloman proof-of-concept test. They prototyped a GPS/pseudolite system allowing coverage during times of reduced GPS availability [6].

Henzler [15] proposed a pseudolite-only flight landing system very similar to the current *Locata* system discussed later in this document. Concepts such as the near-far problem of transmission power and time synchronization between pseudolites were addressed and configured in the system. However this initial system foregoes any tropospheric corrections or multipath error correction. In addition, the pseudolites were arranged near ground level parallel to the runway, unable to take advantage of better geometry formations by positioning. Unfortunately, the group could not conduct actual testing during landing and restricted themselves to flyovers.

Hung Kyu Lee, et al. [16] investigated pseudolite augmentation for GPS airborne applications and identified significant improvements in geometry which yielded increased accuracy in the vertical component. These simulations explore the optimal placement of the pseudolites and the improvements expected depending on the number of pseudolites used for augmentation.

NAVSYS [7] intended to go one step further and create a GPS/pseudolite precision approach and landing system capable of achieving Category II/III landing capability. In this system, the pseudolite broadcasts differential carrier ranging corrections as well as serving as a measurement source. Their tests included actual flight testing using a 737 flown by the NASA Langley Research Facility at Wallops Island, VA. They concluded that the pseudolite significantly improved geometry and yielded precision sufficient to meet CAT II/III accuracy requirements. Additionally, their findings indicated ground-based observations of temperature, pressure, and humidity were not sufficient to model the differential tropospheric group delay due to boundary layer effects during testing.

Monda et al. [20] experimented with an indoor pseudolite positioning system at the Navigation Systems Testing Laboratory at NASA's Johnson Space Center. They focused on real-time solutions using an extended Kalman filter to gain sub-

meter accuracies. Cycle slip detection and mitigation became the central theme in their testing. To mitigate this problem, a change in the reference pseudolite based on signal-to-noise ratio (SNR) values was instituted in which the pseudolite with the highest SNR may become the reference depending on a "trigger" value. They concluded real-time kinematic positioning would be possible if successfully detecting cycle slips in double-differenced measurements were resolved. Unfortunately, their experiments did not resolve this problem.

Bouska [6] simulated a pseudolite based reference system attempting to account for all facets of the problem including tropospheric modeling and pseudolite position errors. He also incorporated carrier-phase integer ambiguity resolution via the Fast Ambiguity Search Filter (FASF) developed by Chen and Lapachelle [9] and Least squares AMbiguity Decorrelation Adjustment (LAMBDA) developed by Teunissen [27]. His use of the extended Kalman filter [5] to estimate states consisting of position, velocity, acceleration, and double-differenced ambiguity, provided Monte-Carlo analysis of various pseudolite placement schemes and tropospheric models. He suggested centimeter level accuracies could be obtained with a pseudolite only system. Additionally, he integrated optimal smoothing techniques [5] and a weighted measurement covariance matrix to improve solutions. His research provides valuable insight into the concepts found later in this document, especially the error modeling aspects due to the requirement of finding the true errors for real data and the similarities to simulated data.

Although pseudolite signals are very similar to GPS signals, many assumptions made for GPS navigation cannot be applied to pseudolite operations. Section 2.6.1 details the differences between GPS and pseudolite systems. Dai et al. [11] addressed some of the challenges that pseudolites present by developing unique modeling strategies to deal with pseudolite error sources. They also analyzed the impact of pseudolite user geometry on differential pseudolite navigation.

Barnes, Rizos, and Wang [3] conducted indoor testing of the first prototype of the *LocataNet* in corporate offices and a steel manufacturing plant [2] to illustrate the effectiveness of *LocataNet* positioning through occlusions and high multipath environments. These initial tests solidified the carrier-phase positioning accuracy needed to proceed with further development and refinement of the system available today.

1.3.3 Tropospheric Modeling. Fukushima et al. [12] calculated the tropospheric delay for airport pseudolites (APLs) using double-differenced carrier-phase measurements from GPS and the APL. These measurements were compared with the theoretical tropospheric delay (Hopfield) [12] and radiosonde measurements obtained from the records of the Japan Meteorological Agency for the past year. The comparisons showed good agreement between the double-differencing technique and the theoretical calculations. The theoretical and radiosonde analysis showed larger deviations attributed to the distance between the APL and the radiosonde measurement locations, but they did not exceed 50cm at 10NM from the APL. This testing shows promise for tropospheric modeling at low elevation angles, especially for pseudolites. Most tropospheric models simply map the calculated vertical tropospheric delay to the slant range needed, disregarding anything with elevations less than 15 degrees.

Zhang [29] conducted tests to predict the residual tropospheric delays on GPS carrier phase observables using redundant measurements from a network of GPS reference receivers. He provides an extensive overview of current models and mapping functions in use today and the benefits and drawbacks of each. Additionally, he shows that double-differenced tropospheric delays are reasonably modeled as first-order Gauss-Markov processes. Although his testing uses elevations above 10 degrees, the results show accurate and stable results worth experimenting with elevations below 10 degrees.

Van Dierendonck [28] specifically postulates a formula for low-elevation tropospheric corrections for pseudolites used at airports. His method develops the differential tropospheric delay as a function of range, differential altitude, temperature,

pressure, and surface refractivity. Bouska used this formulation in creating and estimating the tropospheric delay for a pseudolite only network. The Van Dierendonck model is expressed as

$$\tau_{APL,u}(R_u, \Delta h_u) = \frac{\Delta\tau_{v,dry} + \Delta\tau_{v,wet}}{\sin(el_u)} = \frac{(\Delta\tau_{v,dry} + \Delta\tau_{v,wet})}{\Delta h_u} R_u$$

$$= \frac{77.6 P_s \times (42700 - h_s) \times 10^{-6}}{5 T_s \Delta h_u} \left[\left(1 - \frac{\Delta h_{APL}}{42700 - h_s}\right)^5 - \left(1 - \frac{\Delta h_{APL} + \Delta h_u}{42700 - h_s}\right)^5 \right] R_u$$

$$+ \frac{N_s \times (13000 - h_s) \times 10^{-6}}{5 \Delta h_u} \left[\left(1 - \frac{\Delta h_{APL}}{13000 - h_s}\right)^5 - \left(1 - \frac{\Delta h_{APL} + \Delta h_u}{13000 - h_s}\right)^5 \right] R_u$$

$$(1.1)$$

where

$$N_s = 2.277(10^{-6}) \frac{RH}{T_s^2} \left(10^{\frac{7.4475(T_s - 273\text{K})}{T_s - 38.3\text{K}}}\right) \tag{1.2}$$

and

$\tau_{APL,u}$ = tropospheric delay for mobile receiver (meters)

R_u = slant range between the pseudolite and user (meters)

Δh_u = the height of the user above the pseudolite (meters)

$\Delta\tau_{v,dry}$ = differential vertical dry delay (meters)

$\Delta\tau_{v,wet}$ = differential vertical wet delay (meters)

el_u = elevation angle in radians

Δh_{APL} = difference in height between pseudolites and reference receiver

h_s = height of reference receiver

P_s = surface pressure (millibars)

T_s = surface temperature (Kelvins)

RH = relative humidity (percent)

N_s = surface refractivity

Bouska and Raquet [4] discuss the effects of tropospheric reduction efforts relating to DGPS and differential pseudolite techniques. They offered two methods enhancing reduction of the residual tropospheric effects after applying differential techniques. The first, a weighted measurement covariance matrix, theorizes the errors in the tropospheric model will generally be proportional to the modeled tropospheric delay. The filter enhancement includes weighting the measurement covariance matrix R selectively, based on the predicted tropospheric delay for each measurement generated by the tropospheric model. In simulations, this simple method produced good results and significantly improved the carrier-phase ambiguity resolution capability. The second method estimates the tropospheric model error as an additional state in the Kalman filter. The error, expressed as a scale factor, is modeled as a first order Gauss-Markov process. This implementation improved simulated position accuracy by over 30 percent and assisted ambiguity resolution ability.

1.4   Scope

The development of an extended Kalman filter (EKF) to produce the floating point estimates of sub-centimeter level accuracy carrier-phase solutions is the focus of this research. These solutions will use real data captured from the *LocataNet* and compared to DGPS solutions taken simultaneously. The scope of this thesis includes verifying consistent accuracy of the *LocataNet* and improving the solution via modeling of the residual tropospheric error and eradication of biases.

All software development utilized the Matlab 7 environment. Implementation of derived models for the tropospheric errors via the EKF provide reduction of the dominant error sources in the *LocataNet*. This thesis does not address the design and implementation of pseudolite transmitters and receivers, nor does it attempt integer ambiguity resolution.

1.5   Assumptions

The following assumptions are made in this thesis:

a) Real-time integer ambiguity resolution is not required or possible because the current *LocataLite* system utilizes a frequency lock loop and the focus is the augmentation of a post-processed flight reference system.

b) The extended Kalman filter is not dependent upon a specific *LocataNet* system implementation.

c) All calculations use the Earth-Centered Earth-Fixed (ECEF) or East-North-Up (ENU) frame and World Geodetic Systems 1984 (WGS-84) coordinates.

d) No jamming analysis is required, because the *LocataLites* operate in the 2.4GHz industrial, scientific, and medical (ISM) band. The *LocataNet* can utilize transmitters and receivers operating at non-GPS frequencies and at much greater power levels than GPS, providing better resistance to jamming.

e) The sources of error present in the code and carrier-phase *LocataLite* measurements are assumed to be of similar characteristics to those available with high-quality GPS receivers.

f) The timing discrepancy between *LocataLites* is resolved via *TimeLoc*, which synchronizes timing for transmission between all *LocataLites* in the *LocataNet* [3].

1.6   Thesis Overview

Chapter 2 presents the background theory for this research through an in-depth review of Kalman filter methods, GPS fundamentals, pseudolite navigation, and *LocataLites*. The section on Kalman filtering includes the derivation of an extended Kalman filter. The section on *LocataLites* covers how *LocataLites* differ from conventional pseudolites, *TimeLoc*, and the *LocataNet*. Chapter 3 details *LocataLite* filter models, the modeling of tropospheric errors, and unknown system biases. Chapter 4 describes analysis of the effects of the implemented models for tropospheric errors and resolution of position errors. Chapter 5 summarizes the results and provides recommendations for future research for a *LocataLite*-based reference system.

II. Background

2.1   Overview

This chapter begins by providing a basic overview of Kalman filter theory, including the extension to extended Kalman filter (EKF) applications. The next section describes GPS operation and DGPS techniques. This is followed by a description of the challenges of pseudolite navigation. The last section provides the necessary background and differences in *LocataLites* versus conventional pseudolites. These sections closely follow the work of Bouska [6], since this thesis represents a continuation of his work using real measurements instead of simulation.

2.2   Kalman Filters

Deterministic analysis has been successfully applied to many systems, but it lacks adequacy when applied to particular problems of interest. The linear Kalman filter embodies an optimal recursive data processing algorithm [17], commonly applied when deterministic analysis proves insufficient. The optimality stems from the basic assumptions for the Kalman filter, including an adequate model of the real-world application in the form of a linear dynamics model driven by white Gaussian noise of known statistics. Then, linear measurements corrupted by white Gaussian noises of known statistics can be used for the basis of the optimal estimate by the Kalman filter [17]. The Kalman filter may produce sub-optimal results if either the dynamics or measurement model yields an inadequate representation of the real world [6]. The Kalman filter also constitutes the optimal estimator because it incorporates all available measurements, regardless of their accuracy, to compute the estimates of the variables of interest based on the system dynamics and measurement models, the statistical description of the system noises, measurement errors, and the model uncertainties [17].

When processing discrete-time measurements, a Kalman filter includes both a time propagation cycle and a measurement update cycle. The propagation cycle

2-1

computes an estimate of the system state based on its previous system state and its (imperfect) dynamics model. The update cycle then uses the noise-corrupted measurements to refine the system state estimates at the sample time. A complete derivation can be found in [17].

2.2.1   State and Measurement Model Equations.   The following development is similar to those found in [6,17]. The system dynamics assumptions require modeling as a linear system with a state equation of the form

$$\dot{\mathbf{x}}(t) = \mathbf{F}(t)\mathbf{x}(t) + \mathbf{B}(t)\mathbf{u}(t) + \mathbf{G}(t)\mathbf{w}(t) \qquad (2.1)$$

where

$$\mathbf{x}(t) = \text{the n-dimensional system state vector}$$
$$\mathbf{F}(t) = \text{the n-by-n state dynamics matrix}$$
$$\mathbf{B}(t) = \text{the n-by-r control input matrix}$$
$$\mathbf{u}(t) = \text{the r-dimensional control input}$$
$$\mathbf{G}(t) = \text{the n-by-s noise input matrix}$$
$$\mathbf{w}(t) = \text{the s-dimensional dynamics driving noise vector}$$

and

$$E\{\mathbf{w}(t)\} = \mathbf{0} \qquad (2.2)$$
$$E\{\mathbf{w}(t)\mathbf{w}^T(t+\tau)\} = \mathbf{Q}(t)\delta(\tau) \qquad (2.3)$$

where τ has units of time. Upper case bold letters indicate matrices, lower case bold letters indicate vectors, and normal or italics represent scalar variables. Random vectors are denoted by boldface sans serif type. For the purposes of this research no control inputs exist, so the $\mathbf{B}$ and $\mathbf{u}$ terms will be dropped from any subsequent equations.

At discrete times the solution to Equation (2.1) can be written as:

$$\mathbf{x}(t_{i+1}) = \mathbf{\Phi}(t_{i+1}, t_i)\mathbf{x}(t_i) + \left[\int_{t_i}^{t_{i+1}} \mathbf{\Phi}(t_{i+1}, \tau)\mathbf{G}(\tau)d\boldsymbol{\beta}(\tau) \right] \tag{2.4}$$

where $\boldsymbol{\beta}$ represents a vector valued Brownian motion process of diffusion $\mathbf{Q}(t)$ [17], and $\mathbf{\Phi}(t_{i+1}, t_i)$ denotes the state transition matrix from t_i to t_{i+1} and yields

$$\mathbf{\Phi}(t_{i+1}, t_i) = \mathbf{\Phi}(\Delta t) = e^{\mathbf{F}\Delta t} \text{ where } \Delta t \equiv t_{i+1} - t_i \tag{2.5}$$

which assumes a time-invariant $\mathbf{F}$ matrix. The equivalent discrete-time model is expressed by the following stochastic difference equation as

$$\mathbf{x}(t_{i+1}) = \mathbf{\Phi}(t_{i+1}, t_i)\mathbf{x}(t_i) + \mathbf{w}_d(t_i) \tag{2.6}$$

where

$$\mathbf{w}_d(t_i) = \int_{t_i}^{t_{i+1}} \mathbf{\Phi}(t_{i+1}, \tau)\mathbf{G}(\tau)\mathrm{d}\boldsymbol{\beta}(\tau) \tag{2.7}$$

The discrete-time white Gaussian dynamics driving noise has the statistics:

$$E\{\mathbf{w}_d(t_i)\} = \mathbf{0} \tag{2.8}$$

$$E\{\mathbf{w}_d(t_i)\mathbf{w}_d^T(t_i)\} = \mathbf{Q}_d(t_i) = \int_{t_i}^{t_{i+1}} \mathbf{\Phi}(t_{i+1}, \tau)\mathbf{G}(\tau)\mathbf{Q}(\tau)\mathbf{G}^T(\tau)\mathbf{\Phi}^T(t_{i+1}, \tau)d\tau \tag{2.9}$$

$$E\{\mathbf{w}_d(t_i)\mathbf{w}_d^T(t_j)\} = \mathbf{0}, \text{ t}_i \neq \text{t}_j \tag{2.10}$$

Typical problems of interest defined by a continuous-time dynamics process generate sampled-data (or discrete-time) measurements produced by sensors. Assuming the measurement model can be given as a linear, discrete-time system of the form

$$\mathbf{z}(t_i) = \mathbf{H}(t_i)\mathbf{x}(t_i) + \mathbf{v}(t_i) \tag{2.11}$$

The statistics of the measurement corruption noise are described by

$$E\{\mathbf{v}(t_i)\} = \mathbf{0} \tag{2.12}$$

$$E\{\mathbf{v}(t_i)\mathbf{v}^T(t_j)\} = \begin{cases} \mathbf{R}(t_i) & \text{for } t_i = t_j \\ \mathbf{0} & \text{for } t_i \neq t_j \end{cases} \tag{2.13}$$

The dynamics driving noise $\mathbf{w}_d(t_i)$ and the measurement corruption noise $\mathbf{v}(t_i)$ assumed to be independent, yielding

$$E\{\mathbf{w}_d(t_i)\mathbf{v}^T(t_j)\} = \mathbf{0} \text{ for all } t_i \text{ and } t_j \tag{2.14}$$

    2.2.2 Kalman Filter Equations.   The Kalman filter propagates forward in time from t_{i-1}^+ to t_i^-, starting from the last update cycle state and covariance estimates. The superscripts "+" and "−" denote the time after a measurement update and before a measurement update respectively. Propagating the filter from t_i to t_{i+1} is equivalent to propagating from t_{i-1} to t_i simply by incrementing the index. The initial conditions $\hat{\mathbf{x}}(t_0)$ and $\mathbf{P}(t_0)$ are used in the first propagation cycle. The propagation cycle is given by

$$\hat{\mathbf{x}}(t_i^-) = \boldsymbol{\Phi}(t_i, t_{i-1})\hat{\mathbf{x}}(t_{i-1}^+) \tag{2.15}$$

$$\mathbf{P}(t_i^-) = \boldsymbol{\Phi}(t_i, t_{i-1})\mathbf{P}(t_{i-1}^+)\boldsymbol{\Phi}^T(t_i, t_{i-1}) + \mathbf{G}_d(t_{i-1})\mathbf{Q}_d(t_{i-1})\mathbf{G}_d^T(t_{i-1}) \tag{2.16}$$

When measurements are available, the Kalman filter is updated by

$$\mathbf{A}(t_i) = \mathbf{H}(t_i)\mathbf{P}(t_i^-)\mathbf{H}^T(t_i) + \mathbf{R}(t_i) \tag{2.17}$$

$$\mathbf{K}(t_i) = \mathbf{P}(t_i^-)\mathbf{H}^T(t_i)\mathbf{A}(t_i)^{-1} \tag{2.18}$$

$$\mathbf{r}(t_i) = \mathbf{z}_i - \mathbf{H}(t_i)\hat{\mathbf{x}}(t_i^-) \tag{2.19}$$

$$\hat{\mathbf{x}}(t_i^+) = \hat{\mathbf{x}}(t_i^-) + \mathbf{K}(t_i)\mathbf{r}(t_i) \tag{2.20}$$

$$\mathbf{P}(t_i^+) = \mathbf{P}(t_i^-) - \mathbf{K}(t_i)\mathbf{H}(t_i)\mathbf{P}(t_i^-) \tag{2.21}$$

A properly designed filter has a zero-mean residual vector $\mathbf{r}(t_i)$ with the filter-computed covariance $\mathbf{A}(t_i)$ [6]. The outputs of the Kalman filter update cycle are $\hat{\mathbf{x}}(t_i^+)$ and $\mathbf{P}(t_i^+)$, which are then used in the next propagation cycle.

2.3 Extended Kalman Filters

The linear Kalman filter may become inadequate when either the state dynamics or measurement model contains nonlinearities. Methods choosing to ignore old data due to cumulative errors, or decreasing the filter's confidence in the adequacy of the filter model attempt to address the problem of nonlinearities. However, linearization of the measurement or dynamics model demonstrates a better way to deal with nonlinearities, thus enabling linearized estimation techniques.

A linearized Kalman filter consists of a first order Taylor series approximation to the nonlinear models, linearizing about a nominal trajectory that is normally pre-computed. The EKF differs from the linearized Kalman filter by re-linearizing about each state estimate as it progresses. This enables the EKF to handle larger degrees of nonlinearities more adequately. A complete derivation of EKFs can be found in [18].

2.3.1 State and Measurement Model Equations. Following the Kalman filter development in references [6, 18], a nonlinear system dynamics model takes the form

$$\dot{\mathbf{x}}(t) = \mathbf{f}[\mathbf{x}(t), t] + \mathbf{G}(t)\mathbf{w}(t) \tag{2.22}$$

The state dynamics vector definition becomes a possibly nonlinear function of the n-dimensional state vector $\mathbf{x}(t)$, and of the continuous time, t. The definitions of the n-dimensional state dynamics vector $\mathbf{x}(t)$ and the n-by-s noise distribution matrix $\mathbf{G}(t)$ remain unchanged from those seen in association with Equation (2.1). The dynamics driving noise vector $\mathbf{w}(t)$ also remains unchanged, given by Equations (2.2) and (2.3).

The nonlinear discrete-time measurement equation takes the form

$$\mathbf{z}(t_i) = \mathbf{h}[\mathbf{x}(t_i), t_i] + \mathbf{v}(t_i) \tag{2.23}$$

The m-dimensional measurement vector $\mathbf{z}(t_i)$ represents a linear or nonlinear function of the state vector and time $(\mathbf{h}[\mathbf{x}(t_i), t_i])$, corrupted by the linearly additive m-dimensional discrete-time noise input vector $\mathbf{v}(t_i)$. The discrete-time noise vector does not differ from that of the linear Kalman filter.

2.3.2   State and Measurement Model Linearization: the Linearized Kalman Filter.   If either the system or measurement model Equations (2.22) and (2.23) exhibit nonlinearities, linearization must occur in order to produce an optimal state estimate, to first order. Reference [18] demonstrates a perturbation technique of the state about a nominal or reference trajectory. Although the dynamics model remains linear for this research, the linearization of the dynamics model and measurement model are presented for completeness.

The nominal state trajectory generated from the initial condition appears as $\mathbf{x}_n(t_0) = \mathbf{x}_{n0}$ and the differential equation

$$\dot{\mathbf{x}}_n(t) = \mathbf{f}[\mathbf{x}_n(t), t] \tag{2.24}$$

which differs from the nonlinear state equation by being deterministic. The nominal measurements defined in a similar fashion by

$$\mathbf{z}_n(t_i) = \mathbf{h}[\mathbf{x}_n(t_i), t_i] \tag{2.25}$$

which is also deterministic by removing the last term in Equation (2.22). The perturbation state derivative $\delta\dot{\mathbf{x}}(t)$ formed by the subtraction of the nominal trajectory

(2.24) from the system model (2.22)

$$\delta\dot{\mathbf{x}}(t) \equiv [\dot{\mathbf{x}}(t) - \dot{\mathbf{x}}_{\mathrm{n}}(t)] = \mathbf{f}[\mathbf{x}(t), t] - \mathbf{f}[\mathbf{x}_{\mathrm{n}}(t), t] + \mathbf{G}(t)\mathbf{w}(t) \tag{2.26}$$

A Taylor series expansion of $\mathbf{f}[\mathbf{x}(t), t]$ about $\mathbf{x}_{\mathrm{n}}(t)$ yields

$$\mathbf{f}[\mathbf{x}(t), t] = \mathbf{f}[\mathbf{x}_{\mathrm{n}}, t] + \left.\frac{\partial \mathbf{f}[\mathbf{x}(t), t]}{\partial \mathbf{x}}\right|_{\mathbf{x} = \mathbf{x}_n(t)} [\mathbf{x}(t) - \mathbf{x}_n(t)] + h.o.t. \tag{2.27}$$

where "*h.o.t.*" represents the higher order terms in powers of $[\mathbf{x}(t) - \mathbf{x}_n(t)]$ greater than one [18]. Substituting Equation (2.27) into Equation (2.26), the $\mathbf{f}[\mathbf{x}_{\mathrm{n}}(t), t]$ term cancels to produce the perturbation equation. The first order approximation ignores the higher order terms, yielding

$$\dot{\delta\mathbf{x}}(t) = \mathbf{F}[t; \mathbf{x}_n(t)]\delta\mathbf{x}(t) + \mathbf{G}(t)\mathbf{w}(t) \tag{2.28}$$

This linearized dynamics equation can be implemented in a linearized Kalman filter with the n-by-n partial derivative matrix $\mathbf{F}[t; \mathbf{x}_n(t)]$ evaluated along a nominal trajectory and defined as

$$\mathbf{F}[t; \mathbf{x}_n(t)] = \left.\frac{\partial \mathbf{f}[\mathbf{x}(t), t]}{\partial \mathbf{x}}\right|_{\mathbf{x} = \mathbf{x}_n(t)} \tag{2.29}$$

If higher order terms of the Taylor series expansion prove negligible, the approximation remains valid.

The development of the measurement perturbation equation is formed in a similar way. The measurement perturbation $\delta\mathbf{z}(t)$ is formed by the subtraction of the nominal measurement Equation (2.25) from the measurement model Equation (2.23) to give

$$\delta\mathbf{z}(t_{\mathrm{i}}) \equiv [\mathbf{z}(t_i) - \mathbf{z}_n(t_i)] = \mathbf{h}[\mathbf{x}(t_i), t_i] - \mathbf{h}[\mathbf{x}_{\mathrm{n}}(t_i), t_i] + \mathbf{v}(t_i) \tag{2.30}$$

2-7

A Taylor series expansion of $\mathbf{h}[\mathbf{x}(t_i), t_i]$ about $\mathbf{x}_n(t)$ yields

$$\mathbf{h}[\mathbf{x}(t_i), t_i] = \mathbf{h}[\mathbf{x}_n(t_i), t_i] + \left. \frac{\partial \mathbf{h}[\mathbf{x}, t_i]}{\partial \mathbf{x}} \right|_{\mathbf{x}=\mathbf{x}_n(t_i)} [\mathbf{x}(t_i) - \mathbf{x}_n(t_i)] + h.o.t. \qquad (2.31)$$

When Equation (2.31) is substituted into Equation (2.30), the $\mathbf{h}[\mathbf{x}_n(t_i), t_i]$ term is cancelled to produce the perturbation equation. The first order approximation ignores the higher order terms which yields

$$\delta\mathbf{z}(t_i) \equiv \mathbf{H}[t_i; \mathbf{x}_n(t_i)]\delta\mathbf{x}(t_i) + \mathbf{v}(t_i) \qquad (2.32)$$

This linearized measurement equation can be implemented in the linearized Kalman filter with the m-by-n partial derivative matrix $\mathbf{H}[t_i; \mathbf{x}_n(t_i)]$ evaluated along a nominal trajectory and defined as:

$$\mathbf{H}[t_i; \mathbf{x}_n(t_i)] = \left. \frac{\partial \mathbf{h}[\mathbf{x}, t_i]}{\partial \mathbf{x}} \right|_{\mathbf{x}=\mathbf{x}_n(t_i)} \qquad (2.33)$$

This approximation is valid as long as the higher order terms of the Taylor series expansion in Equation (2.31) are negligible. The state and measurement perturbation equations are error state representations which must be added to the nominal state values to produce the total state estimate.

The equations developed in this section define the linearized Kalman filter. Real-world measurements $\mathbf{z}(t_i)$ are differenced with $\mathbf{z}_n(t_i)$ computed via Equation (2.25), and then fed into a linearized Kalman filter based on Equations (2.28) and (2.32), to generate estimates of $\delta\mathbf{x}(t)$. These can be added to $\mathbf{x}_n(t)$, generated as solutions to Equation (2.24), to estimate the total states. It is important to point out that the EKF relinearizes the model about the new estimate $\hat{\mathbf{x}}(t_i^+)$ and the corresponding trajectory. The relinearization process helps to validate the assumption that the deviations from the nominal trajectory are sufficiently small to use first order methods.

2.3.3 Extended Kalman Filter Equations. The EKF propagates forward in time t_{i-1} to t_i by integrating from the last update cycle, state and covariance estimates. The initial conditions $\hat{\mathbf{x}}(t_0)$ and $\mathbf{P}(t_0)$ generate the first propagation. The EKF propagation equations are defined by:

$$\dot{\hat{\mathbf{x}}} = \mathbf{f}[\hat{\mathbf{x}}(t|t_{i-1}), t] \tag{2.34}$$

$$\dot{\mathbf{P}}(t|t_{i-1}) = \mathbf{F}[t; \hat{\mathbf{x}}(t|t_{i-1})]\mathbf{P}(t|t_{i-1}) + \mathbf{P}(t|t_{i-1})\mathbf{F}^T[t; \hat{\mathbf{x}}(t|t_{i-1})] + \mathbf{G}(t)\mathbf{Q}(t)\mathbf{G}^T(t) \tag{2.35}$$

with $t|t_{i-1}$ denoting the value of a given variable at time t, conditioned on all the measurements up to and including time t_{i-1}. The term $\mathbf{F}[t; \hat{\mathbf{x}}(t|t_{i-1})]$ is the n-by-n partial derivative matrix:

$$\mathbf{F}[t; \hat{\mathbf{x}}(t|t_{i-1})] = \left.\frac{\partial \mathbf{f}[\mathbf{x}(t), t]}{\partial \mathbf{x}}\right|_{\mathbf{x} = \hat{\mathbf{x}}(t|t_{i-1})} \tag{2.36}$$

The differential equation initial conditions are given by:

$$\hat{\mathbf{x}}(t_{i-1}|t_{i-1}) \equiv \hat{\mathbf{x}}(t_{i-1}^+) \tag{2.37}$$

$$\mathbf{P}(t_{i-1}|t_{i-1}) \equiv \mathbf{P}(t_{i-1}^+) \tag{2.38}$$

After integrating equations (2.34) and (2.35) to the next sample time, the state and covariance estimates are defined as:

$$\hat{\mathbf{x}}(t_i^-) \equiv \hat{\mathbf{x}}(t_i|t_{i-1}) \tag{2.39}$$

$$\mathbf{P}(t_i^-) \equiv \mathbf{P}(t_i|t_{i-1}) \tag{2.40}$$

The EKF incorporates the measurements in the following update equations:

$$\mathbf{K}(t_i) = \mathbf{P}(t_i^-)\mathbf{H}^T[t_i; \hat{\mathbf{x}}(t_i^-)]\{\mathbf{H}[t_i; \hat{\mathbf{x}}(t_i^-)]\mathbf{P}(t_i^-)\mathbf{H}^T[t_i; \hat{\mathbf{x}}(t_i^-)] + \mathbf{R}(t_i)\}^{-1} \qquad (2.41)$$

$$\hat{\mathbf{x}}(t_i^+) = \hat{\mathbf{x}}(t_i^-) + \mathbf{K}(t_i)\{\mathbf{z}_i - \mathbf{h}[\hat{\mathbf{x}}(t_i^-), t_i]\} \qquad (2.42)$$

$$\mathbf{P}(t_i^+) = \mathbf{P}(t_i^-) - \mathbf{K}(t_i)\mathbf{H}[t_i; \hat{\mathbf{x}}(t_i^-)]\mathbf{P}(t_i^-) \qquad (2.43)$$

2.4 Global Positioning System

The following sections describe the Global Positioning System (GPS) with significant portions taken from [6, 19, 23]. GPS consists of a constellation of medium earth orbit satellites providing a continuous ranging source. The user calculates position, velocity, and time from the received signal. Differential GPS (DGPS) includes many different methods and techniques resulting in greater accuracy than standalone GPS.

2.4.1 *GPS Signal.*   The GPS signal contains both a code and carrier-phase component. The Coarse/Acquisition (C/A) code is available to civilian users and the precision (P) code (called P(Y) after encryption) is for the military. The carrier frequencies currently set at 1575.42 MHz and 1227.6 MHz are commonly known as the L1 and L2 frequencies, respectively [19]. The P(Y) code gets transmitted on both L1 and L2, yet C/A code is only available on the L1 frequency. The 1023-bit sequence C/A code repeats every millisecond and the P(Y) code repeats every 7 days per satellite. The chipping rates for the C/A and P(Y) codes are 1.023 MHz and 10.23 MHz, respectively. The code component of the GPS signal contains a pseudorandom noise (PRN) code unique to each satellite.

Civilian receivers track the C/A code on the L1 frequency. Military dual-frequency receivers track the P(Y) codes on both the L1 and L2 frequencies. Some civilian receivers use semi-codeless techniques used to obtain range information from the P(Y) code without actually decrypting it [23]. These high-precision civilian re-

ceivers used in CPS render the L2 carrier-phase information without really tracking the P(Y) code.

2.4.2 GPS Measurements. Typically, three raw measurements from a GPS receiver include code, Doppler, and carrier-phase. The code measurement, often called a "pseudorange," comprises the actual range corrupted by measurement errors (primarily the clock error). The Doppler measurement describes the frequency shift in the signal due to vehicle (and clock) dynamics, and the carrier-phase can be thought of as an integrated Doppler. The term "raw" is included to distinguish these measurements from the navigation processor outputs such as position, velocity, and acceleration. DGPS techniques will be distinguished based on using code, carrier-phase, or both.

2.4.3 Code Measurements. The code pseudorange represents the true range between the satellite and user plus the impact of a number of error sources. The calculation of the time difference between the transmission and reception time multiplied by speed of light (providing the range in meters) yields the pseudorange. The pseudorange measurement expressed in the equation below as

$$\rho = r + c(\delta t_u - \delta t_{sv}) + T + I + m_\rho + v_\rho \tag{2.44}$$

where

$$\rho = \text{GPS pseudorange measurement (meters)}$$

$$r = \text{true range from the user to satellite (meters)}$$

$$c = \text{speed of light (meters / second)}$$

$$\delta t_u = \text{receiver (user) clock error (seconds)}$$

$$\delta t_{sv} = \text{transmitter (satellite vehicle) clock error (seconds)}$$

$$T = \text{errors due to tropospheric delay (meters)}$$

$$I = \text{errors due to ionospheric delay (meters)}$$

$$m_\rho = \text{errors due to pseudorange multipath (meters)}$$

$$v_\rho = \text{errors in pseudorange due to receiver noise (meters)}$$

2.4.4 Carrier-Phase Measurements. For high precision solutions the carrier-phase measurement of the received signal offers greater accuracy. The carrier-phase measurement (expressed in cycles) is

$$\phi = \lambda^{-1}(r + c(\delta t_u - \delta t_{sv}) + T - I + m_\phi + v_\phi) + N \tag{2.45}$$

where

$$\phi = \text{carrier-phase measurement (cycles)}$$

$$\lambda = \text{carrier-phase wavelength (meters / cycle)}$$

$$N = \text{carrier-phase integer ambiguity (cycles)}$$

$$T = \text{errors due to tropospheric delay (meters)}$$

$$I = \text{errors due to ionospheric delay (meters)}$$

$$m_\phi = \text{errors due to carrier-phase measurement multipath (meters)}$$

$$v_\phi = \text{errors in carrier-phase measurement due to receiver noise (meters)}$$

The rest of the terms previously defined in Equation (2.44) do not differ, with the exception of the measurement noise and multipath, which become significantly smaller for the carrier-phase versus the code. Some sources of error do not affect the code and carrier-phase measurement in the same manner. The sign on the ionospheric delay term represents the phenomenon of code-carrier divergence, in which the ionosphere advances a carrier-phase measurement but delays a code measurement. Conversely, tropospheric delay affects both the code and carrier-phase by the same magnitude when expressed in equivalent units.

The carrier-phase integer ambiguity term introduces an error source present in carrier-phase measurements, but not in code measurements. The ambiguity term represents the unknown number of carrier-cycles present at the start of the signal integration [23]. Attaining the highest level of accuracy requires determining the unknown number of cycles (integer ambiguity) before signal integration.

2.4.5 Single Differencing. Differential GPS uses linear combinations of observations (code or carrier measurements) between receivers, satellites, or times to reduce the effect of some errors [24]. A single-difference may be between two satellites (∇) or between two receivers ($\triangle$). Figure 2.1 depicts the concept of a single-difference between two receivers.
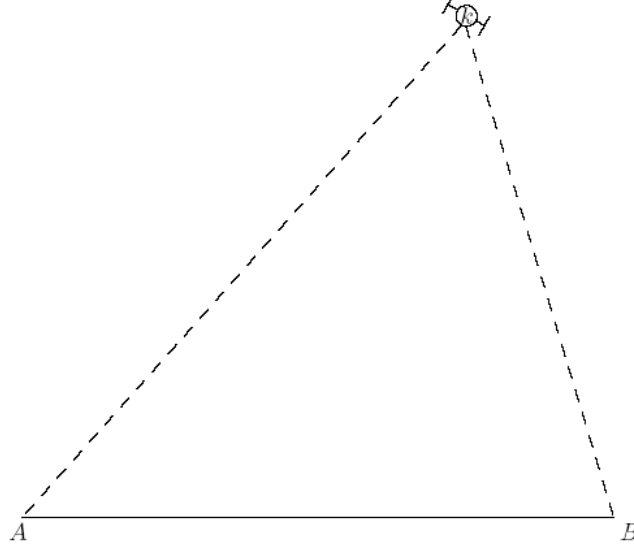
Figure 2.1:   Single-Difference GPS Between Receivers A and B and Satellite k

The single-differenced carrier-phase measurement between two receivers corresponding to the above figure is defined as

$$\Delta\phi_{AB}^k \equiv \phi_A^k - \phi_B^k \tag{2.46}$$

where ϕ_A^k represents the phase measurement between receiver A and satellite k, and ϕ_B^k represents the phase measurement between receiver B and satellite k.

This type of difference eliminates the satellite clock error and reduces the atmospheric errors. Combining the carrier-phase measurement Equation (2.45) with the single-difference Equation (2.46) yields

$$\begin{aligned}
\Delta\phi_{AB}^k = {} & \lambda^{-1}[r_A^k + c(\delta t_{u_A}^k - \delta t_{sv_A}^k) + T_A^k - I_A^k + m_{\phi A}^k + v_{\phi A}^k] + N_A^k \\
& - \lambda^{-1}[r_B^k + c(\delta t_{u_B}^k - \delta t_{sv_B}^k) + T_B^k - I_B^k + m_{\phi B}^k + v_{\phi B}^k] + N_B^k
\end{aligned} \tag{2.47}$$

2-14

Combining like terms yields

$$\Delta\phi_{AB}^{k} = \lambda^{-1}[(r_A^k - r_B^k) + c(\delta t_{u_A}^k - \delta t_{u_B}^k) - c(\delta t_{sv_A}^k - \delta t_{sv_B}^k) + (T_A^k - T_B^k)$$
$$- (I_A^k - I_B^k) + (m_{\phi A}^k - m_{\phi B}^k) + (v_{\phi A}^k - v_{\phi B}^k)] + (N_A^k - N_B^k) \qquad (2.48)$$

After eliminating the satellite clock term (due to synchronous measurements in which the satellite clock error is the same for both), differences represented as (Δ) transform the above equation to

$$\Delta\phi_{AB}^{k} = \lambda^{-1}(\Delta r_{AB}^k + c\Delta\delta t_{u_{AB}}^k + \Delta T_{AB}^k - I_{AB}^k + \Delta m_{\phi AB}^k + v_{\phi AB}^k) + \Delta N_{AB}^k \qquad (2.49)$$

The integer value ΔN_{AB}^k represents the difference in the carrier-phase ambiguity between the two receivers' measurements.

2.4.6 Double Differencing. Double differencing utilizes the combination of single differencing between satellites (transmitters) and single differencing between receivers. Because single differencing between receivers cancels the satellite clock error and single differencing between satellites cancels the receiver clock error, double differencing cancels both clock error terms.
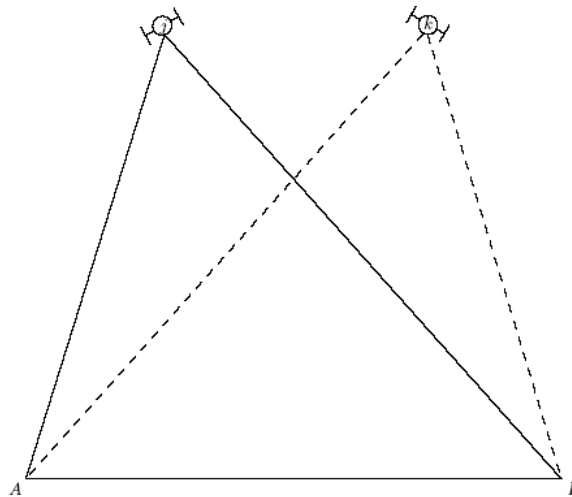
Figure 2.2:   Double-Difference Between Satellites j and k with Receivers A and B

Using the phase measurement in the following example, the double-differenced carrier-phase measurement is defined as:

$$\Delta\nabla\phi_{AB}^{kj} = \Delta\phi_{AB}^{k} - \Delta\phi_{AB}^{j} \qquad (2.50)$$

After substituting the single-differenced phase Equation (2.49) in the above equation:

$$\Delta\nabla\phi_{AB}^{k}j = \lambda^{-1}(\Delta r_{AB}^{k} + c\Delta\delta t_{u_{AB}}^{k} + \Delta T_{AB}^{k} - \Delta I_{AB}^{k} + \Delta m_{AB}^{k} + \Delta v_{AB}^{k} + \Delta N_{AB}^{k}$$
$$- \left[\lambda^{-1}(\Delta r_{AB}^{j} + c\Delta\delta t_{u_{AB}}^{j} + \Delta T_{AB}^{j} - \Delta I_{AB}^{j} + \Delta m_{\phi AB}^{j} + \Delta v_{\phi AB}^{j} + \Delta N_{AB}^{j}\right]$$
$$\qquad (2.51)$$

After cancelling the user clock error term, the double-difference operator $(\Delta\nabla)$ expresses the double-difference error terms, rendering:

$$\Delta\nabla\phi_{AB}^{kj} = \lambda^{-1}(\Delta\nabla r_{AB}^{kj} + \Delta\nabla T_{AB}^{kj} - \Delta\nabla I_{AB}^{kj} + \Delta\nabla m_{\phi AB}^{kj} + \Delta\nabla v_{\phi AB}^{kj}) + \Delta\nabla N_{AB}^{kj} \quad (2.52)$$

Differencing reduces the effects of correlated errors (such as atmospheric errors) at the expense of increasing the effects of uncorrelated errors (such as measurement noise and multipath). The single-difference increases the magnitude of the noise and multipath by a factor of $(\sqrt{2})$, while the double-difference increases the magnitude by a factor of 2. Although the integer ambiguity term $(\Delta\nabla N_{AB}^{kj})$ differs from the ambiguity term from the observation equation, it maintains its integer nature.

The double-differenced code measurement can be adapted from Equation (2.52) by dropping the ambiguity terms and expressing the range in terms of meters

$$\Delta\nabla\rho_{AB}^{kj} = \Delta\nabla r_{AB}^{kj} + \Delta\nabla T_{AB}^{kj} - \Delta\nabla I_{AB}^{kj} + \Delta\nabla m_{\rho AB}^{kj} + \Delta\nabla v_{\rho AB}^{kj} \qquad (2.53)$$

However, double-difference code measurements seldomly see practical use. Rather, direct estimation of the receiver clock error combined with single-difference measurements denote typical practice [6].

2.4.7 Carrier-Phase Ambiguity Resolution. Carrier-phase ambiguity resolution refers to the process of selecting the correct integer value for the phase ambiguity. Ambiguity resolution generally consists of two primary operations [24]. The first creates the ambiguity search space by the generation of candidate ambiguity sets. The second operation selects the correct ambiguity set. However, integer ambiguity resolution is not always possible due to measurement constraints or receiver properties. Since this research does not involve integer ambiguity resolution, no further development is necessary.

2.5 Pseudolites

The term pseudolite (short for "pseudo-satellite") refers to ground-based GPS-like transmitters. Pseudolites feature the flexibility to vary the location, power, and frequency of the transmitter. Pseudolites additionally provide signals for navigation purposes in adverse environments such as open-pit mining, warehouses, and GPS jammed environments where GPS signals often become unusable [23]. Many of the assumptions made with GPS navigation cannot be applied to pseudolites. This section begins with a discussion of differences between GPS and pseudolite navigation, then presents typical pseudolite applications, and ends with descriptions of the problems and sources of error in pseudolite measurements.

2.5.1 GPS-Pseudolite Differences. Many of the assumptions used in GPS processing differ for pseudolite navigation. These include:

- Expected ranges for pseudolites prove much more dynamic than for GPS operation and will affect receiver power levels.

- When using a static reference receiver, there exists no relative motion between the reference receiver and each pseudolite such as between a reference receiver and the orbiting GPS satellites. This results in measurement biases due to pseudolite location errors that do not average out over time. Also the multipath error between pseudolites and the reference receiver will have stronger time

correlations than the multipath experienced at the mobile receiver, when in motion.

- Pseudolites are not constrained to operate at the GPS L1 and L2 frequencies. Likewise, the code sequences and chipping rates may differ from those GPS satellites use.

- Due to the short ranges between pseudolite transmitters and receivers, the measurement model becomes more nonlinear, compared to GPS operation.

- Pseudolites do not bear an orbital or ephemeris error, but rather a position error dependent on the accuracy of the estimated phase center of the pseudolite antenna.

- Elimination of ionospheric delays stems from the fact pseudolite signals do not travel through the ionosphere.

- Tropospheric error reduction through single and double differencing yields smaller gains than for GPS due to uncommon signal paths between pseudolites and receivers.

2.5.2   Pseudolite Applications.   The four categories of pseudolite applications include direct positioning, digital data transmission, carrier-phase ambiguity resolution, and as a differential reference station [10]. Direct positioning using a network of pseudolites known as *LocataLites* describes the application addressed in this research.

Pseudolite direct positioning accomplished with both the code and carrier-phase measurements represents a method similar to conventional GPS positioning. The majority of work with pseudolites pertains to augmentation of GPS or GPS/INS. Pseudolites improve the overall geometry of the augmented system, providing greater positioning accuracy, reliability, availability, continuity, and integrity monitoring [22]. Additionally, GPS signals are typically weak or not present indoors, and pseudolites provide an indoor navigation source. This research specifically targets implementing pseudolites as the sole source of navigation.

Several methods exist to improve pseudolite positioning. Digital data transmission via pseudolite transmitters offers advantages such as GPS reference data requiring only slight modification of the GPS receiver [10]. Another method assists and speeds up the carrier-phase ambiguity resolution in a GPS system augmented by pseudolites, accomplished through the large changes in geometries of the pseudolite signal [22]. The Kinematic GPS Landing Systm (KGLS) at Stanford [10] exemplifies this technique. Lastly, when a pseudolite rebroadcasts a coherent replica of received GPS signals, it becomes a differential reference station [10]. This difference between the direct and reflected signal allows use of navigation methods.

2.5.3 Signal Interference and Near-Far Problem. The largest issues facing practical pseudolite applications are the signal interference and the associated near-far problem. While the distance from any GPS satellite to a receiver remains relatively constant, the ranges between a pseudolite and receiver vary greatly. The large dynamic difference in ranges results in large differences in received power levels. This may cause the automatic gain control in a receiver to adjust to the highest powered signal, which effectively jams all other pseudolites.

Pseudolites possess both a "near" and a "far" radius defined by the usable area. A pseudolite jams all other pseudolites within the near radius. The far radius identifies the distance within which a receiver must stay to maintain lock on a particular pseudolite. The transmission power determines the near and far radii, increasing or decreasing power increases or decreases the near and far radii by the same ratio. For practical systems a ratio of 1/10 typifies the relationship between the near and far radius [10], although this varies depending on the cross-correlation of the codes. Figure 2.3 shows an example of the near-far radii.
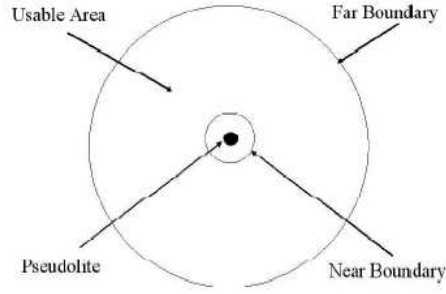
Figure 2.3:   Near-Far Problem [6]

Three categories represent the various techniques proposed to reduce the near-far problem—Time Division Multiple Access (TDMA), Frequency Division Multiple Access (FDMA), and Code Division Multiple Access (CDMA) [6].

TDMA occurs through the pulsing of the pseudolites, a process in which transmission only occurs at fixed intervals. Pulsed pseudolites operated at greater than 20-25 percent of a duty cycle effectively jam the GPS signal [6]. One proposal suggests operating two pseudolites, each pulsing at 10-12.5 percent of the duty cycle, to facilitate an integrated GPS/Pseudolite navigation system [6]. This arrangement still only allows the use of two pseudolites while maintaining GPS capability. If GPS is not of interest, 10 pseudolites could be used (given a 10 percent duty cycle each).

The second technique for interference reduction, FDMA implementation, modifies GPS signals with small frequency offsets. Elrod et. al [6] suggested offsetting the frequency to the first null of the GPS satellite signal in order to reduce cross-correlation with the GPS signal. It resembles a large Doppler offset most receivers handle easily.

CDMA demonstrations via concatenations of C/A codes showed through simulation a code length of 4092 (4 times that of C/A code) would provide a 6 dB enhancement, and thus double the far radius while maintaining the same near radius, according to Ndili [22]. By combining 20 C/A codes for a length of 20460 in addition

to operating at a P-code chipping rate would add a 23 dB enhancement. The longer the code length and higher the chipping rate, the larger the near-far ratio.

    2.5.4 Sources of Error. Pseudolite errors separate into measurement and measurement model errors. Both affect the accuracy of a pseudolite system and are apparent in the residual term formed by subtracting the measurement prediction from the measurement as shown by the following equation:

$$\mathbf{r}_i = \mathbf{z}_i - \mathbf{h}[\hat{\mathbf{x}}(t_i^-); t_i] \tag{2.54}$$

The next two subsections describe the errors present in pseudolite measurements and measurement models.

    2.5.4.1 Pseudolite Measurement Errors. Double differencing error reduction proves less effective for pseudolites than for the analogous GPS equations due to a different geometric configuration [6]. The measurement noise, multipath, and residual tropospheric error (i.e., the error after a tropospheric model application) define the remaining errors in a pseudolite carrier-phase measurement after a double-difference operation.

    The quality of the receiver determines the measurement noise associated with pseudolites (just like for a GPS measurement). Along with proper modeling in the navigation filter, improving the receiver design constitutes one of the ways to reduce the effect of measurement noise.

    Multipath dominates pseudolite applications as an error source [6]. Multipath mitigating techniques (such as antenna placement and choke-ring antennas) implemented in a pseudolite system offer less impact on pseudolite signals compared to satellite signals [6]. This also stems from the relative geometries in the transmitter-receiver setup in a pseudolite network.

Time-invariant or standing multipath represents a major concern for pseudolite applications, especially when the receiver remains in a static (non-moving) position. This contributes to a multipath error which is much more difficult to handle than the multipath error associated with satellite signals. The navigation filter assumes white (uncorrelated in time) error sources, and the more time-invariant the multipath becomes, the more this assumption becomes invalid. Removing this constant error from the corresponding measurements requires careful calibration. The use of carrier-phase measurements and antenna design appear promising in reducing multipath [6]. Multipath affects code measurements to a higher degree than carrier-phase measurements for both a pseudolite or satellite source. Antenna gain shaping helps to reduce multipath by adjusting the gain in the direction of large reflectors [6].

Precision pseudolite applications require accounting for the residual tropospheric error that exists after applying a tropospheric model. The amount that single and double differencing reduce the effect of tropospheric delay in GPS operation becomes a function of the baseline difference in the mobile receiver position. Pseudolite applications display the same characteristics as a very large baseline for which differencing may reduce, but not significantly remove, tropospheric delay.

2.5.4.2 Pseudolite Measurement Model Errors. Pseudolite measurement model errors include the effect of position errors in the location of the pseudolites in addition to the error due to linear approximations in the measurement model.

Analogous to the ephemeris or orbital errors in GPS satellite locations, imprecise locations comprise the source of errors of the pseudolite transmitters. Like tropospheric errors, single and double differencing impacts these position errors for pseudolites less than for GPS.

For outdoor pseudolite applications, static surveying techniques using carrier-phase DGPS can solve for the pseudolite positions within centimeters. Generally, this technique remains unusable indoors. Kee [8] presented a method to calculate the pseudolite positions using only the user's position information and the pseudolite

signals. This method proves advantageous because the location yields the phase center of the antenna instead of the physical center. The phase center of the antenna represents the true position and is not always the same as the physical center, which is commonly referenced as the true position.

The typical ranges between transmitters and receivers represent one of the biggest differences between GPS and pseudolite navigation. GPS signals travel 20,000 kilometers or more, while pseudolite signal ranges typically measure in meters (depending on signal power). As the ranges in pseudolite navigation become shorter, the signal waveform becomes more spherical than planar. Figure 2.4 depicts this relationship with a planar signal from a GPS satellite and a spherical signal from a pseudolite. In reality a GPS signal is spherical, but the large radius makes it essentially planar for a GPS user.
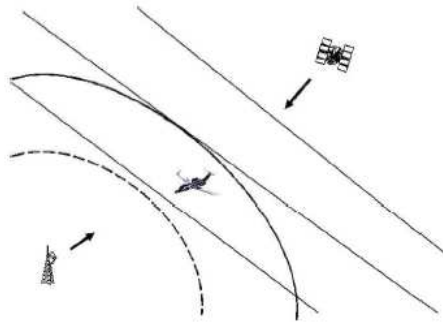
Figure 2.4:   Spherical and Planar Wavefronts [6]

The measurement model equation for the extended Kalman filter (EKF) remains nonlinear for both GPS and pseudolite navigation. An EKF linearizes the nonlinear measurement equation by using a first order Taylor series approximation. As the waveforms become more spherical, the measurement nonlinearity becomes more severe and the first order approximation becomes more inadequate. While for GPS signals the approximation error stays small enough to be ignored, pseudolite navigation requires care in handling the large measurement nonlinearities.

The nonlinearity error explained graphically in Figure 2.5 shows a spherical waveform at the receiver location. The uncertainty orthogonal to the line-of-sight from transmitter to receiver only increases the range. This results in a range underestimation. As the waveforms become more spherical, this error becomes more substantial.
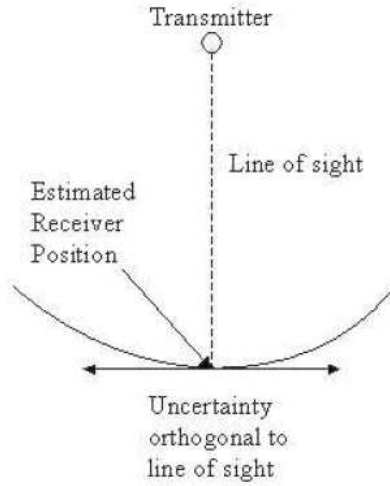
Figure 2.5:   Nonlinear Elongation of Range [6]

This problem typically refers to a nonlinear elongation of measured range and suggests applying nonlinear filtering techniques to enlarge the region of convergence for a Kalman filter. Divergence may occur if the nonlinearity approaches the size of the measurement error.

2.6   LocataNet

A *LocataNet* consists of four or more *LocataLites* geometrically positioned with a single *LocataLite* designated as the master. All other *LocataLites* synchronize with the master via *TimeLoc* (see Section 2.6.3) and allow carrier-phase point positioning of the receiver while in range of the *LocataNet*. Since the *LocataLites* remain synchronized in time, a reference receiver is not necessary. Each *LocataLite* does not necessarily have to be in range of the master due to retransmission by other *LocataLites* in the *LocataNet* [3]. This allows placement of *LocataLites* outside the field of view of the

master, but in possibly better locations to capture receiver movement. The following list describes additional advantages of the *LocataNet* as found in Locata development articles [3]:

- Wireless connectivity - No radio modems or physical wires connect the *LocataLites*, which require 12VDC via batteries or transformer.

- Reduced latency - Carrier point positioning using time synchronized signals from the *LocataLites* allows real-time position computation.

- Intelligent signal transmissions - Standard pseudolites typically use pulsing to prevent jamming and reduce the near-far problem discussed earlier. However, multiple devices may end up transmitting at exactly the same time and cause interference problems. The *LocataNet* precisely controls signal transmissions to ensure the *LocataLites* do not transmit at the same time, preventing interference between *LocataLite* signals.

- Theoretically greater precision - In DGPS the double-differenced observable is formed from four carrier-phase measurements. Assuming all measurements possess equal precision and are uncorrelated, the precision of the double-differenced measurement is two times worse than a single carrier-phase measurement (the basic measurement used by *LocataLites*).

- Time solution - In DGPS the double differencing procedure eliminates the clock biases, while the *LocataNet* allows time estimation with position.

2.6.1 LocataLites . *LocataLites* differ from conventional pseudolites due to several enhancements not typically found on pseudolites. Barnes et.al. [3] describes the *LocataLite* as an "intelligent pseudolite transceiver" due to the software advancements. The main advantage to this flexible approach stems from the ability to enact design changes without hardware revision.

2.6.2 LocataLite composition. To facilitate faster development of the *LocataLite* system, existing GPS hardware provided quick development with small mod-

ifications. The receiver portion utilizes a commercially available GPS chipset with modifications in the signal acquisition, tracking loops, and navigation algorithm. The antennas consist of commercially available patch antennas for the receive portion and a custom 1/4 wave antenna for the master transmitter.

2.6.3 TimeLoc. To achieve carrier-phase point positioning without a reference receiver, *LocataLites* require a high degree of time synchronization. Therefore *TimeLoc* performs this synchronization of all *LocataLites* in a *LocataNet*. The following excerpt from [3] describes the steps to perform *TimeLoc* between *LocataLite* A (the master) and *LocataLite* B (the slave).

1. *LocataLite* A transmits C/A code and carrier signals on a particular PRN code.

2. Receiver section of *LocataLite* B acquires, tracks, and measures the signal (C/A code and carrier-phase) generated by *LocataLite* A.

3. *LocataLite* B calculates the difference between the code and carrier of the received signal and its own locally generated signal. Ignoring propagation errors, the differences between the two signals represent the difference in the clocks of the two devices and the geometric separation between them.

4. *LocataLite* B adjusts its local oscillator using Direct Digital Synthesis (DDS) technology [3] to bring the code and carrier differences between itself and *LocataLite* A to zero. Monitoring the code and carrier differences between *LocataLite* A and B maintains a zero difference.

5. The final stage corrects for the geometrical offset between *LocataLite* A and B by using the known coordinates of the *LocataLites*, thus achieving *TimeLoc*.

The above procedure allows synchronization with inexpensive temperature controlled crystal oscillators (TCXO) instead of expensive atomic clocks. Additionally, this removes the timing issue between *LocataLites* leaving only the time difference between the *LocataNet* and the receiver to resolve.

2.7 Summary

This chapter provided a basic overview of Kalman filter theory including extended Kalman filters. GPS techniques, including carrier-phase differential algorithms, were presented. The section on pseudolites described the challenges and issues of pseudolite navigation, while the section on *LocataLites* outlined differences and advantages of *LocataLites* over standard pseudolites.

2-27

III. Methodology and Algorithm Development

3.1 Overview

This chapter outlines the provided measurements, differencing method, and floating-point filter for determining the position solution of real or simulated data. Additional elements to the baseline filter include the tropospheric correction model, a residual tropospheric error state, and position error states. Lastly, an overview of the developed simulator and simulated errors provide distinction between real and simulated data filter characteristics. Figure 3.1 depicts the overall algorithm.
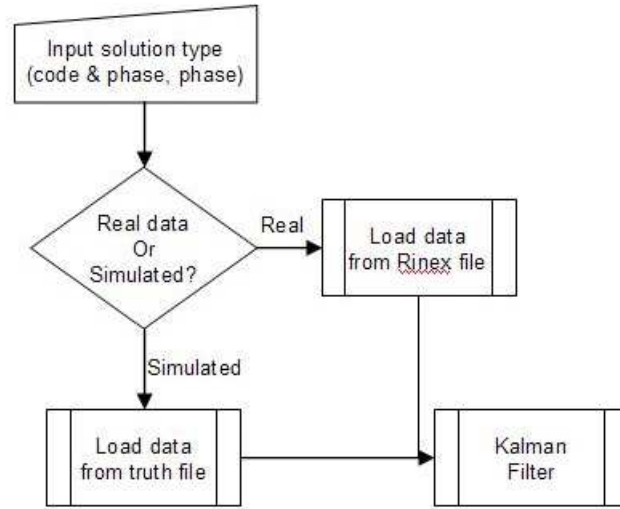
Figure 3.1: Overall filter algorithm

The input flags determine whether code and carrier-phase or carrier-phase only measurements will be used. The filter performs the same functionally with real or simulated data, but loads the appropriate file based on input. The details of the Kalman filter are developed later in this chapter.

3.2 Measurements

Sections 2.4.3 through 2.4.5 developed the standard and single-differenced measurement equations for GPS applications. Those equations require adaptation for

use with *LocataLite* measurements. Since *LocataLite* signals remain lower than the ionosphere, the ionospheric error terms disappear. This results in the following code measurement equation for *LocataLite* application for code (ρ) and carrier-phase (ϕ):

$$\rho = r + c(\delta t_u - \delta t_{LL}) + T + v_\rho \tag{3.1}$$

$$\phi = \lambda^{-1}(r + T + v_\phi) + N \tag{3.2}$$

For code measurements, δt_{LL} denotes the time of the *LocataNet*. For the single-difference carrier-phase from the base (1 below) to each *LocataLite* (k below)

$$\Delta\phi^{1k} = \lambda^{-1}(\Delta r^{1k} + \Delta T^{1k} + v_{\phi^{1k}}) + \Delta N^{1k} \qquad k = 2, 3, \cdots, n \tag{3.3}$$

The superscript term $1k$ represents the measurement from *LocataLite* 1 differenced with the measurement from *LocataLite* k, where k=2 to n. Bear in mind the superscript 1 denotes the *LocataLite* designated as the base, not necessarily *LocataLite* with PRN 1, but labeled as such for convenience. Reference to *LocataLite* 1 assumes base designation for this research, yet in actual testing the base may be any available *LocataLite*. The single-difference clock error in Equation (2.49) is removed due to the *TimeLoc* function discussed in Section 2.6.3. In both Equations (3.1) and (3.2), the multipath term becomes assimilated into the measurement noise term due to the inability to model multipath effectively and simply letting the Kalman filter account for multipath as the dominant measurement noise. GPS navigation is affected by errors in the predicted motion of the satellites, commonly referred to as ephemeris or orbital errors. These errors occur when the receiver uses the imprecise satellite locations for range calculations. *LocataLites* posess a corresponding error due to the imprecise estimates of the *LocataLite* locations. These *LocataLite* position errors and tropospheric delay error terms represent the primary errors of interest for this research.

The following sections describe the process of generating the measurement corrections and state models used in the filter. This entails the *LocataLite* position

errors, followed by the descriptions of measurement noise, SNR deviations, and lastly tropospheric delay. Measurement noise and tropospheric delay error attempt to account for errors to the true ranges. The simulated SNR errors utilized actual SNR measurements for different runs. Position errors affected true positions.

   3.2.1 LocataLite Position Errors. The imprecise estimated positions of the *LocataLites* affect the code and carrier-phase measurement by the same magnitude. The location errors of the *LocataLites* were modeled as biases with an initial zero-mean Gaussian distribution. The horizontal standard deviation of 1 cm and the vertical of 2 cm represent the expected accuracies of precision surveying [13,21]. Table 3.1 specifies the surveyed *LocataLite* positions utilizing DGPS techniques.

Table 3.1:   *LocataLite* Truth Locations in ECEF Coordinates

LocataLite	X (m)	Y (m)	Z (m)
1	-4431516.461	2635737.865	-3743255.799
2	-4431939.3259	2636221.8376	-3742211.8162
3	-4432228.4352	2636339.2064	-37431769.434
4	-4432842.397	2635894.7	-3741362.46
5	-4432209.8086	2635733.7889	-3742244.2687
Origin for ENU	-4432198.51525	2636230.218	-3741880.7353

The errors due to inaccurate positions of the *LocataLites* were not added to the true range, but instead used by the filter in the measurement prediction calculation.

   3.2.2 Measurement Noise. The addition of zero-mean white Gaussian noise to the measurements embodies the dominant multipath as well as the true measurement noise. Measurement noise becomes considerably smaller for carrier-phase measurements than for code measurements, and was modeled with a 2.6 m standard deviation for the code versus a 2 mm standard deviation for the carrier-phase [24].

3.2.3 Tropospheric Delay. The generation of tropospheric delay taken from reference [28] provides a method to calculate low elevation tropospheric delay using temperature, atmospheric pressure, relative humidity, elevation angle, and range. The atmospheric parameters utilized local weather observation stations. The original tropospheric delay calculation for airport pseudolites (APLs) and the reference receiver is given by Equation (1.1) and adaptation for *LocataLites* yields

$$\tau_{LL,u}(R_u, \Delta h_{LL}) = \frac{77.6 P_s \times (42700 - h_s) \times 10^{-6}}{5 T_s \Delta h_{LL}} \left[1 - \left(1 - \frac{\Delta h_{LL}}{42700 - h_s}\right)^5\right] R_u$$
$$+ \frac{N_s \times (13000 - h_s) \times 10^{-6}}{5 \Delta h_{LL}} \left[1 - \left(1 - \frac{\Delta h_{LL}}{13000 - h_s}\right)^5\right] R_u \quad (3.4)$$

with variables defined as

$\tau_{LL,u}$ = tropospheric delay for receiver (meters)

Δh_{LL} = difference in height between *LocataLite* and receiver

h_s = height of the *LocataLite*

R_u = slant range between the pseudolite and user (meters)

P_s = surface pressure (millibars)

T_s = surface temperature (Kelvins)

RH = relative humidity (percent)

N_s = surface refractivity

Both Equations (1.1) and (3.4) present valid solutions for positive and negative elevation angles, but indeterminate for zero elevation angles [28]. The reference did develop equations for zero elevation angles, but placement of the *LocataLites* did not result in zero elevation angles for this research.

3.3 Floating-Point Differential LocataLite Kalman Filter

A post-processed floating-point differential *LocataLite* Kalman filter was modified from the filter developed in reference [24] and adapted for *LocataLite* navigation.

The single-difference operation applied to the carrier-phase measurements allows the removal of the clock error. This section presents the baseline filter development, with modifications for residual tropospheric error and *LocataLite* position errors presented in the next section. The baseline filter calculates position, velocity, acceleration, clock bias, clock drift, and carrier-phase ambiguity estimates for the receiver. The objective of the filter is to produce position, tropospheric scale-factor percentage, and *LocataLite* position error estimates. Before filter processing begins, a pre-processing step determines the number of visible *LocataLites* and a vector of visible *LocataLite* PRNS ordered by SNR quality from which the base *LocataLite* for single-difference operation is selected.

3.3.1 Differential LocataLite Model Equations. A First Order Gauss Markov Acceleration (FOGMA) model defined the three position, three velocity, and three acceleration states of the floating-point differential *LocataLite* Kalman filter. The remaining states consisted of a clock bias and clock drift state and $(n - 1)$ carrier-phase ambiguity states, where n signifies the number of *LocataLites* in view at a particular epoch.

To describe the FOGMA model, the time derivatives of the positions yield the velocities, and the time derivatives of the velocities yield the accelerations. Filter settings allow the position to be expressed in either the Earth-Centered-Earth-Fixed (ECEF) or East-North-Up (ENU) coordinate frame. This research focused on solutions in ENU with the origin located at the position of the first epoch. The following equations represent the dynamics equations for the first nine states, where $x_1 - x_3$ represent the positions, $x_4 - x_6$ represent the velocities, and $x_7 - x_9$ represent the accelerations.

$$
\begin{aligned}
\dot{x}_1 &= x_4 & \dot{x}_4 &= x_7 \\
\dot{x}_2 &= x_5 & \dot{x}_5 &= x_8 \\
\dot{x}_3 &= x_6 & \dot{x}_6 &= x_9
\end{aligned}
\tag{3.5}
$$

The position and velocity states do not include any direct driving noise and their determination relies entirely on other states and observed measurements. The acceleration states, modeled as first order Gauss-Markov processes, are as follows:

$$\dot{x}_7 = (-1/T_a)x_7 + w_{a_1}(t)$$
$$\dot{x}_8 = (-1/T_a)x_8 + w_{a_2}(t) \quad\quad (3.6)$$
$$\dot{x}_9 = (-1/T_a)x_9 + w_{a_3}(t)$$

with associated dynamic driving noise processes given by

$$E\left\{w_{a_1}(t)w_{a_1}(t+\tau)\right\} = E\left\{w_{a_2}(t)w_{a_2}(t+\tau)\right\} = E\left\{w_{a_3}(t)w_{a_3}(t+\tau)\right\}$$
$$= \frac{2\sigma_a^2}{T_a}\delta(\tau) = q_a\delta(\tau) \quad\quad (3.7)$$

The anticipated acceleration maneuvers and time correlations determine the correlation time, T_a, and acceleration variance (or mean square value), σ_a^2. This filter utilizes a T_a set to 0.01 seconds to account for relatively short acceleration maneuvers, and a σ_a of $19.6 m/s^2$ to handle the highest possible accelerations. These values combine to yield a q_a of $76832 \ m^2/sec^5$ and represent tuning parameters for the filter derived from the original modified DGPS filter [24], then tuned for the *LocataNet*.

The ambiguity states, modeled as random walks rather than constant biases, allowed the filter to correct itself if convergence leads to an incorrect value. The cycle ambiguities consist of an additional $(n-1)$ states always at the end of the state vector. The single-differenced carrier-phase ambiguities are defined by:

$$\dot{x}_{12} = w_{\Delta N^{1-2}}$$
$$\dot{x}_{13} = w_{\Delta N^{1-3}}$$
$$\vdots$$
$$\dot{x}_{(11+(n-1))} = w_{\Delta N^{1-n}} \quad\quad (3.8)$$

where PRN 1 is given as the base and n represents the total number of *LocataLites* visible.

The process noise, with statistical characterization as:

$$E\{w_{\Delta N^{bi}}(t)w_{\Delta N^{bi}}(t+\tau)\} = q_N \delta(\tau)$$

$$q_N = 1.1 \times 10^{-7}(\text{cycles}/\sec)^2$$

will yield an increase of approximately 0.1 cycles in the ambiguity standard deviation over a 1 hour period [24]. This will allow the filter to correct itself if it converged to the incorrect value.

The state vector for the floating-point Kalman filter becomes

$$\mathbf{x} = \begin{bmatrix} \mathbf{E} \ \mathbf{N} \ \mathbf{U} \ \dot{\mathbf{E}} \ \dot{\mathbf{N}} \ \dot{\mathbf{U}} \ \ddot{\mathbf{E}} \ \ddot{\mathbf{N}} \ \ddot{\mathbf{U}} \ \mathbf{c_b} \ \mathbf{c_d} \ \boldsymbol{\Delta}\mathbf{N^{1-2}} \ \ldots \ \boldsymbol{\Delta}\mathbf{N^{1-n}} \end{bmatrix}^{\mathbf{T}} \tag{3.9}$$

where

$$x_1 = E = \text{ ENU E position (m)}$$

$$x_2 = N = \text{ ENU N position (m)}$$

$$x_3 = U = \text{ ENU U position (m)}$$

$$x_4 = \dot{E} = \text{ ENU E velocity (m/s)}$$

$$x_5 = \dot{N} = \text{ ENU N velocity (m/s)}$$

$$x_6 = \dot{U} = \text{ ENU U velocity (m/s)}$$

$$x_7 = \ddot{E} = \text{ ENU E acceleration (m/s}^2)$$

$$x_8 = \ddot{N} = \text{ ENU N acceleration (m/s}^2)$$

$$x_9 = \ddot{U} = \text{ ENU U acceleration (m/s}^2)$$

$$x_{10} = c_b = \text{ clock bias (s)}$$

$$x_{11} = c_d = \text{ clock drift (m/s)}$$

$$x_{12} = \Delta N^{1-2} = \text{ single-differenced phase ambiguity (cycles)}$$

$$x_{13} = \Delta N^{1-3} = \text{ single-differenced phase ambiguity (cycles)}$$

$$\vdots$$

$$x_{11+(n-1)} = \Delta N^{1-n} = \text{ single-differenced phase ambiguity (cycles)}$$

The differential equation, similar to Equation (2.1), shows the exclusion of user input represented as

$$\dot{\mathbf{x}}(t) = \mathbf{F}(t)x(t) + \mathbf{G}(t)\mathbf{w}(t) \tag{3.10}$$

3-8

which expands to:

$$
\begin{bmatrix}
\dot{x}_1 \\
\dot{x}_2 \\
\dot{x}_3 \\
\dot{x}_4 \\
\dot{x}_5 \\
\dot{x}_6 \\
\dot{x}_7 \\
\dot{x}_8 \\
\dot{x}_9 \\
\dot{x}_{10} \\
\dot{x}_{11} \\
\dot{x}_{12} \\
\dot{x}_{13} \\
\vdots \\
\dot{x}_n
\end{bmatrix}
=
\begin{bmatrix}
0 & 0 & 0 & 1 & 0 & 0 & 0 & 0 & 0 & 0 & 0 & \cdots & 0 \\
0 & 0 & 0 & 0 & 1 & 0 & 0 & 0 & 0 & 0 & 0 & \cdots & 0 \\
0 & 0 & 0 & 0 & 0 & 1 & 0 & 0 & 0 & 0 & 0 & \cdots & 0 \\
0 & 0 & 0 & 0 & 0 & 0 & 1 & 0 & 0 & 0 & 0 & \cdots & 0 \\
0 & 0 & 0 & 0 & 0 & 0 & 0 & 1 & 0 & 0 & 0 & \cdots & 0 \\
0 & 0 & 0 & 0 & 0 & 0 & 0 & 0 & 1 & 0 & 0 & \cdots & 0 \\
0 & 0 & 0 & 0 & 0 & 0 & \frac{-1}{T_a} & 0 & 0 & 0 & 0 & \cdots & 0 \\
0 & 0 & 0 & 0 & 0 & 0 & 0 & \frac{-1}{T_a} & 0 & 0 & 0 & \cdots & 0 \\
0 & 0 & 0 & 0 & 0 & 0 & 0 & 0 & \frac{-1}{T_a} & 0 & 0 & \cdots & 0 \\
0 & 0 & 0 & 0 & 0 & 0 & 0 & 0 & 0 & 0 & 1 & \cdots & 0 \\
0 & 0 & 0 & 0 & 0 & 0 & 0 & 0 & 0 & 0 & 0 & \cdots & 0 \\
0 & 0 & 0 & 0 & 0 & 0 & 0 & 0 & 0 & 0 & 0 & \cdots & 0 \\
0 & 0 & 0 & 0 & 0 & 0 & 0 & 0 & 0 & 0 & 0 & \cdots & 0 \\
\vdots & \vdots & \vdots & \vdots & \vdots & \vdots & \vdots & \vdots & \vdots & \vdots & \vdots & \ddots & 0 \\
0 & 0 & 0 & 0 & 0 & 0 & 0 & 0 & 0 & 0 & 0 & 0 & 0
\end{bmatrix}
\begin{bmatrix}
x_1 \\
x_2 \\
x_3 \\
x_4 \\
x_5 \\
x_6 \\
x_7 \\
x_8 \\
x_9 \\
x_{10} \\
x_{11} \\
x_{12} \\
x_{13} \\
\vdots \\
x_n
\end{bmatrix}
+
\begin{bmatrix}
0 \\
0 \\
0 \\
0 \\
0 \\
0 \\
w_{a1} \\
w_{a2} \\
w_{a3} \\
w_{a4} \\
w_{a5} \\
w_{\Delta N^{12}} \\
w_{\Delta N^{13}} \\
\vdots \\
w_{\Delta N^{1n}}
\end{bmatrix}
$$

(3.11)

In Equation (3.11), T_a defines the FOGMA acceleration time constant. The $\mathbf{G}(t)$ matrix remains an identity matrix for this research. Recall $\mathbf{Q}$ from Equation (2.22)

defines the process noise and appears as the matrix below.

$$
\mathbf{Q} = \begin{bmatrix}
0 & 0 & 0 & 0 & 0 & 0 & 0 & 0 & 0 & 0 & 0 & 0 & 0 & \cdots & 0 \\
0 & 0 & 0 & 0 & 0 & 0 & 0 & 0 & 0 & 0 & 0 & 0 & 0 & \cdots & 0 \\
0 & 0 & 0 & 0 & 0 & 0 & 0 & 0 & 0 & 0 & 0 & 0 & 0 & \cdots & 0 \\
0 & 0 & 0 & 0 & 0 & 0 & 0 & 0 & 0 & 0 & 0 & 0 & 0 & \cdots & 0 \\
0 & 0 & 0 & 0 & 0 & 0 & 0 & 0 & 0 & 0 & 0 & 0 & 0 & \cdots & 0 \\
0 & 0 & 0 & 0 & 0 & 0 & 0 & 0 & 0 & 0 & 0 & 0 & 0 & \cdots & 0 \\
0 & 0 & 0 & 0 & 0 & 0 & q_a & 0 & 0 & 0 & 0 & 0 & 0 & \cdots & 0 \\
0 & 0 & 0 & 0 & 0 & 0 & 0 & q_a & 0 & 0 & 0 & 0 & 0 & \cdots & 0 \\
0 & 0 & 0 & 0 & 0 & 0 & 0 & 0 & q_a & 0 & 0 & 0 & 0 & \cdots & 0 \\
0 & 0 & 0 & 0 & 0 & 0 & 0 & 0 & 0 & q_c & 0 & 0 & 0 & \cdots & 0 \\
0 & 0 & 0 & 0 & 0 & 0 & 0 & 0 & 0 & 0 & q_d & 0 & 0 & \cdots & 0 \\
0 & 0 & 0 & 0 & 0 & 0 & 0 & 0 & 0 & 0 & 0 & q_N & 0 & \cdots & 0 \\
0 & 0 & 0 & 0 & 0 & 0 & 0 & 0 & 0 & 0 & 0 & 0 & q_N & \cdots & 0 \\
\vdots & \vdots & \vdots & \vdots & \vdots & \vdots & \vdots & \vdots & \vdots & \vdots & \vdots & \vdots & \vdots & \ddots & 0 \\
0 & 0 & 0 & 0 & 0 & 0 & 0 & 0 & 0 & 0 & 0 & 0 & 0 & 0 & q_N
\end{bmatrix}
\tag{3.12}
$$

Table 3.2 summarizes the acceleration mean squared value, time constant, and acceleration noise, along with the phase ambiguity noise values.

Table 3.2: Dynamics Driving Noise Values for Floating-Point Filter

Term	Definition	Value
σ_a^2	Acceleration mean squared value	$(19.6 \ m/sec^2)^2$
T_a	Acceleration time constant	$0.01 \ seconds$
q_a	Acceleration noise strength	$76832 \ m^2/sec^5$
q_N	Phase ambiguity noise strength	$1.1 \times 10^{-7} \ cycles^2/sec$

The DGPS position at first epoch provided a very good first position, resulting in very low initial covariance values for the position states. Conversely, the acceleration and velocity covariances remained higher due to the uncertainty at first epoch.

3-10

The clock bias and drift variance values were taken from [24] since the receiver clock characteristics for the *Locata* closely resemble typical GPS receivers. The initial co-variance matrix is given as

$$
\mathbf{P}(t_0) =
\begin{bmatrix}
\sigma_E^2 & 0 & 0 & 0 & 0 & 0 & 0 & 0 & 0 & 0 & 0 & 0 & 0 & \ldots & 0 \\
0 & \sigma_N^2 & 0 & 0 & 0 & 0 & 0 & 0 & 0 & 0 & 0 & 0 & 0 & \ldots & 0 \\
0 & 0 & \sigma_U^2 & 0 & 0 & 0 & 0 & 0 & 0 & 0 & 0 & 0 & 0 & \ldots & 0 \\
0 & 0 & 0 & \sigma_{\dot{E}}^2 & 0 & 0 & 0 & 0 & 0 & 0 & 0 & 0 & 0 & \ldots & 0 \\
0 & 0 & 0 & 0 & \sigma_{\dot{N}}^2 & 0 & 0 & 0 & 0 & 0 & 0 & 0 & 0 & \ldots & 0 \\
0 & 0 & 0 & 0 & 0 & \sigma_{\dot{U}}^2 & 0 & 0 & 0 & 0 & 0 & 0 & 0 & \ldots & 0 \\
0 & 0 & 0 & 0 & 0 & 0 & \sigma_{\ddot{E}}^2 & 0 & 0 & 0 & 0 & 0 & 0 & \ldots & 0 \\
0 & 0 & 0 & 0 & 0 & 0 & 0 & \sigma_{\ddot{N}}^2 & 0 & 0 & 0 & 0 & 0 & \ldots & 0 \\
0 & 0 & 0 & 0 & 0 & 0 & 0 & 0 & \sigma_{\ddot{U}}^2 & 0 & 0 & 0 & 0 & \ldots & 0 \\
0 & 0 & 0 & 0 & 0 & 0 & 0 & 0 & 0 & \sigma_{c_b}^2 & 0 & 0 & 0 & \ldots & 0 \\
0 & 0 & 0 & 0 & 0 & 0 & 0 & 0 & 0 & 0 & \sigma_{c_d}^2 & 0 & 0 & \ldots & 0 \\
0 & 0 & 0 & 0 & 0 & 0 & 0 & 0 & 0 & 0 & 0 & \sigma_{\Delta N^{12}}^2 & 0 & \ldots & 0 \\
0 & 0 & 0 & 0 & 0 & 0 & 0 & 0 & 0 & 0 & 0 & 0 & \sigma_{\Delta N^{13}}^2 & \ldots & 0 \\
\vdots & \vdots & \vdots & \vdots & \vdots & \vdots & \vdots & \vdots & \vdots & \vdots & \vdots & \vdots & \vdots & \ddots & 0 \\
0 & 0 & 0 & 0 & 0 & 0 & 0 & 0 & 0 & 0 & 0 & 0 & 0 & 0 & \sigma_{\Delta N^{1n}}^2
\end{bmatrix}
\tag{3.13}
$$

with initial covariance values given in Table 3.3.

Table 3.3:   Initial Covariance Values for Floating-Point Filter

Term	Definition	Value
$\sigma_{E,N,U}^2$	Position state variance	$(1\ mm)^2$
$\sigma_{\dot{E},\dot{N},\dot{U}}^2$	Velocity State variance	$(1\ cm/s)^2$
$\sigma_{\ddot{E},\ddot{N},\ddot{U}}^2$	Acceleration state variance	$(384.16\ m/s^2)^2$
$\sigma_{c_b}^2$	Clock bias variance	$(200\ s)^2$
$\sigma_{c_d}^2$	Clock drift variance	$(100\ m/s)^2$
$\sigma_{\Delta N^{1k}}^2$	Phase ambiguity variance	$(\frac{5}{\lambda}\ cycles)^2$

3.3.2 Differential LocataLite Measurement Model. Code, single-differenced carrier-phase measurements, and the DGPS altitude measurement create a $(2n)$ measurement vector (where n represents the number of *LocataLites* available) as input to the floating-point differential *LocataLite* Kalman filter. The filter uses a non-linear measurement model with measurement vector

$$\mathbf{z}(t_i) = [\Delta\phi^{12} \; \cdots \; \Delta\phi^{1n} \; \rho^1_{corr} \; \cdots \; \rho^n_{corr} \; h_{gps}]^T \qquad (3.14)$$

where ρ^1_{corr} is the pseudorange from the receiver to *LocataLite* 1 (the base, not necessarily *LocataLite* with PRN 1 but stated so for convenience), corrected by applying the tropospheric model defined in Equation (3.3). The inclusion of h_{gps} as a measurement represents DGPS height from an external source and allows the filter to overcome the poor geometry of the *LocataNet* during this testing. The filter allows exclusion of the code and height measurements and has the ability to produce solutions based on carrier-phase only; code and carrier-phase only; code, carrier-phase, and height; or carrier-phase and height only. This provides a platform to accommodate varying geometries and capitalize on additional measurements. This also allows the filter to operate with the additional measurements, depending on the type of testing performed.

Recalling the EKF development in Section 2.3 along with Equation (3.2) leads to an expansion of the single-differenced range term and combining the measurement errors yield the carrier-phase equation expressed as

$$\Delta\phi^{1k} = \frac{1}{\lambda} \left[(r^1 - T^1) - (r^k - T^k) \right] + \Delta N^{1k} + v_{\Delta\phi} \quad k = 2, 3, \cdots, n \qquad (3.15)$$

In the preceding equation, T represents the tropospheric delay from the correction model. The $v_{\Delta\phi}$ term represents a white noise, and attempts to account for the combination of the single-differenced measurement noise, multipath, and residual tropospheric delay. The tropospheric delay term in the noise specifies the residual tropospheric delay after a correction model application. Further expanding the range

terms in Equation (3.15) and expressing them in terms of state variables results in

$$\Delta\phi^{1k} = \frac{1}{\lambda}\left[(E^1 - x_1)^2 + (N^1 - x_2)^2 + (U^1 - x_3)^2\right]^{1/2}$$

$$-\frac{1}{\lambda}\left[(E^k - x_1)^2 + (N^k - x_2)^2 + (U^k - x_3)^2\right]^{1/2} \qquad (3.16)$$

$$+\Delta T^{1k} + \Delta N^{1k} + v_{\Delta\Phi} \qquad\qquad k = 2, 3, \cdots, n \qquad (3.17)$$

where E^{1k}, N^{1k}, U^{1k} represent the position of the *LocataLites* indexed by 1 and k.

The partial derivatives for each row of the single-differenced carrier-phase measurements show

$$\left.\frac{\partial h[\mathbf{x}, t_i]}{\partial x_1}\right|_{\mathbf{x}=\hat{\mathbf{x}}(t_i^-)} = \frac{1}{\lambda}\left\{\frac{E^1 - x_1}{[(E^1-x_1)^2+(N^1-x_2)^2+(U^1-x_3)^2]^{1/2}}\right\}$$

$$-\frac{1}{\lambda}\left\{\frac{E^k - x_1}{[(E^k-x_1)^2+(N^k-x_2)^2+(U^k-x_3)^2]^{1/2}}\right\} \qquad (3.18)$$

$$= \frac{1}{\lambda}\left\{e_1^1 - e_1^k\right\}$$

$$\left.\frac{\partial h[\mathbf{x}, t_i]}{\partial x_2}\right|_{\mathbf{x}=\hat{\mathbf{x}}(t_i^-)} = \frac{1}{\lambda}\left\{\frac{N^1 - x_2}{[(E^1-x_1)^2+(N^1-x_2)^2+(U^1-x_3)^2]^{1/2}}\right\}$$

$$-\frac{1}{\lambda}\left\{\frac{N^k - x_2}{[(E^k-x_1)^2+(N^k-x_2)^2+(U^k-x_3)^2]^{1/2}}\right\} \qquad (3.19)$$

$$= \frac{1}{\lambda}\left\{e_2^1 - e_2^k\right\}$$

$$\left.\frac{\partial h[\mathbf{x}, t_i]}{\partial x_3}\right|_{\mathbf{x}=\hat{\mathbf{x}}(t_i^-)} = \frac{1}{\lambda}\left\{\frac{U^1 - x_3}{[(E^1-x_1)^2+(N^1-x_2)^2+(U^1-x_3)^2]^{1/2}}\right\}$$

$$-\frac{1}{\lambda}\left\{\frac{U^k - x_3}{[(E^k-x_1)^2+(N^k-x_2)^2+(U^k-x_3)^2]^{1/2}}\right\} \qquad (3.20)$$

$$= \frac{1}{\lambda}\left\{e_3^1 - e_3^k\right\}$$

$$\left.\frac{\partial h[\mathbf{x}, t_i]}{\partial x_{h_{gps}}}\right|_{\mathbf{x}=\hat{\mathbf{x}}(t_i^-)} = 1 \qquad (3.21)$$

$$\left.\frac{\partial h[\mathbf{x}, t_i]}{\partial x_{\Delta N}}\right|_{\mathbf{x}=\hat{\mathbf{x}}(t_i^-)} = 1 \qquad (3.22)$$

where

$$\mathbf{e}^j = [e_1^j \ e_2^j \ e_3^j] \qquad\qquad j = 1, 2, \cdots, n \qquad\qquad (3.23)$$

provides the unit line-of-sight vectors pointing from the mobile receiver to *LocataLite* j.

When combined, these individual partial derivatives represent one row of the $\mathbf{H}$ matrix

$$\mathbf{H}^{1k} = \left[\frac{1}{\lambda}(\mathbf{e}^1 - \mathbf{e}^k) \ 0 \ 0 \ 0 \ 0 \ 0 \ 0 \ \cdots 1 \cdots 0 \right] \qquad k = 2, 3, \cdots, n \qquad (3.24)$$

where $\frac{1}{\lambda}(\mathbf{e}^1 - \mathbf{e}^k)$ represents the scaled difference vector between two unit line-of-site vectors from the mobile receiver to *LocataLite* 1 and the mobile receiver to *LocataLite* "k". The "1" is placed in the column for the appropriate ambiguity state.

The corresponding rows for the code measurements drop the $\frac{1}{\lambda}$ term and the "1" for the ambiguity states and insert a "1" for the clock state, giving

$$\mathbf{H} = \left[\mathbf{e}^1 \ 0 \ 0 \ 0 \ 0 \ 0 \ 0 \ 1 \cdots 0 \right] \qquad\qquad (3.25)$$

The entire measurement matrix $\mathbf{H}$ is then

$$\mathbf{H} = \begin{bmatrix}
\frac{1}{\lambda}(\mathbf{e}^1 - \mathbf{e}^2) & 0 & 0 & 0 & 0 & 0 & 0 & 0 & 0 & 1 & 0 & \cdots & 0 \\
\frac{1}{\lambda}(\mathbf{e}^1 - \mathbf{e}^3) & 0 & 0 & 0 & 0 & 0 & 0 & 0 & 0 & 0 & 1 & \cdots & 0 \\
\vdots & & \vdots & \vdots & \vdots & \vdots & \vdots & \vdots & \vdots & \vdots & \vdots & \ddots & 0 \\
\frac{1}{\lambda}(\mathbf{e}^1 - \mathbf{e}^n) & 0 & 0 & 0 & 0 & 0 & 0 & 0 & 0 & 0 & 0 & \cdots & 1 \\
\mathbf{e}^1 & & 0 & 0 & 0 & 0 & 0 & 0 & 1 & 0 & 0 & \cdots & 0 \\
\mathbf{e}^2 & & 0 & 0 & 0 & 0 & 0 & 0 & 1 & 0 & 0 & \cdots & 0 \\
\vdots & & \vdots & \vdots & \vdots & \vdots & \vdots & \vdots & \vdots & \vdots & \vdots & \ddots & \vdots \\
\mathbf{e}^n & & 0 & 0 & 0 & 0 & 0 & 0 & 1 & 0 & 0 & \cdots & 0 \\
0 & & 0 & 1 & 0 & 0 & 0 & 0 & 0 & 0 & 0 & \cdots & 0
\end{bmatrix} \qquad (3.26)$$

where superscript "1" represents the base *LocataLite* for n *LocataLites*.

The measurement covariance matrix $\mathbf{R}$ defined in Equation (2.11) and required by the filter represents 5 different types of covariance terms.

- Case 1: Variance of code measurement errors

- Case 2: Variance of phase measurement errors

- Case 3: Variance of height measurement errors

- Case 4: Covariance of two different code measurement errors

- Case 5: Covariance of two different phase measurement errors

The full $\mathbf{R}$ matrix is

$$\mathbf{R} = \begin{bmatrix} \mathbf{R}_{phase} & \mathbf{0} & \mathbf{0} \\ \mathbf{0} & \mathbf{R}_{code} & \mathbf{0} \\ \mathbf{0} & \mathbf{0} & \mathbf{R}_{h_{gps}} \end{bmatrix} \tag{3.27}$$

where the phase variances and covariances denoted by cases 2 and 4 are located in the upper left corner. The code variance and covariances denoted by cases 1 and 3 are placed in the middle, and the height variance is placed in the lower right corner. The off-diagonal terms between the code and carrier-phase covariances represent the cross-covariance of a code and phase measurement, which were assumed sufficiently small and set to zero.

Non-tropospheric components (transmitter location error, multipath, and measurement noise) along with the residual tropospheric error typify the code measurement variances. The standard deviation for the code measurement noise is 2.6 meters [24]. Additionally, the tropospheric contribution to the total standard deviation is sufficiently small and ignored. The single-differenced tropospheric and non-tropospheric standard deviations are 0.004 m^2 for the carrier-phase variance with the covariance terms set to half this value [24]. The following matrix displays the components of the

$\mathbf{R}_{phase}$ matrix.

$$\mathbf{R}_{phase} = \begin{bmatrix} r_{\Delta\phi^{ij},\Delta\phi^{ij}} & r_{\Delta\phi^{ij},\Delta\phi^{ik}} & \cdots & r_{\nabla\Delta\phi^{ij},\nabla\Delta\phi^{ik}} \\ r_{\Delta\phi^{ij},\Delta\phi^{ik}} & r_{\Delta\phi^{ij},\Delta\phi^{ij}} & \ddots & \vdots \\ \vdots & \ddots & \ddots & r_{\Delta\phi^{ij},\Delta\phi^{ik}} \\ r_{\Delta\phi^{ij},\Delta\phi^{ik}} & \cdots & r_{\Delta\phi^{ij},\nabla\Delta\phi^{ik}} & r_{\nabla\Delta\phi^{ij},\nabla\Delta\phi^{ij}} \end{bmatrix} \quad (3.28)$$

The associated $\mathbf{R}_{code}$ matrix is

$$\mathbf{R}_{code} = \begin{bmatrix} r_{\rho^i,\rho^i} & 0 & \cdots & 0 \\ 0 & r_{\rho^i,\rho^i} & \cdots & 0 \\ \vdots & \vdots & \ddots & \vdots \\ 0 & 0 & \cdots & r_{\rho^i,\rho^i} \end{bmatrix} \quad (3.29)$$

and the values for the full $\mathbf{R}$ matrix are shown in Table 3.4.

Table 3.4:   Measurement Covariance Values

Term	Definition	Value
r_{ρ^i,ρ^i}	Code variance error	2.6 m^2
r_{ρ^i,ρ^j}	Code covariance error	0 m^2
$r_{\Delta\phi^{ij},\Delta\phi^{ij}}$	Single-differenced carrier-phase variance error	.004 m^2
$r_{\Delta\phi^{ij},\Delta\phi^{ik}}$	Single-differenced carrier-phase covariance error	.002 m^2
$r_{h_{gps}}$	GPS height measurement variance error	10^{-7} m^2

The $r_{h_{gps}}$ term reflects a "perfect" measurement and therefore only aides the filter, thus the very small variance value, yet large enough not to affect filter convergence. Since the truth comparison for this research is DGPS, identifying the incorporated altitude measurement as perfect is reasonable.

3.3.3 Discrete-Time Models.   For use on a digital computer, conversion of the linear stochastic differential equations requires formulation to describe the equivalent discrete-time system model [17]. The discrete-time state transition matrix

$\boldsymbol{\Phi}(t_{k+1}, t_k)$ for this filter is

$$\boldsymbol{\Phi}(t_{k+1}, t_k) = \boldsymbol{\Phi}(\Delta t) = e^{\mathbf{F}\Delta t} \tag{3.30}$$

where $\Delta t \equiv t_{k+1} - t_k$ which results in the matrix

$$\boldsymbol{\Phi}(t_{k+1}, t_k) = \begin{bmatrix}
1 & 0 & 0 & \Delta t & 0 & 0 & A & 0 & 0 & 0 & 0 & \cdots & 0 \\
0 & 1 & 0 & 0 & \Delta t & 0 & 0 & A & 0 & 0 & 0 & \cdots & 0 \\
0 & 0 & 1 & 0 & 0 & \Delta t & 0 & 0 & A & 0 & 0 & \cdots & 0 \\
0 & 0 & 0 & 1 & 0 & 0 & B & 0 & 0 & 0 & 0 & \cdots & 0 \\
0 & 0 & 0 & 0 & 1 & 0 & 0 & B & 0 & 0 & 0 & \cdots & 0 \\
0 & 0 & 0 & 0 & 0 & 1 & 0 & 0 & B & 0 & 0 & \cdots & 0 \\
0 & 0 & 0 & 0 & 0 & 0 & C & 0 & 0 & 0 & 0 & \cdots & 0 \\
0 & 0 & 0 & 0 & 0 & 0 & 0 & C & 0 & 0 & 0 & \cdots & 0 \\
0 & 0 & 0 & 0 & 0 & 0 & 0 & 0 & C & 0 & 0 & \cdots & 0 \\
0 & 0 & 0 & 0 & 0 & 0 & 0 & 0 & 0 & 1 & \Delta t & \cdots & 0 \\
0 & 0 & 0 & 0 & 0 & 0 & 0 & 0 & 0 & 0 & 1 & \cdots & 0 \\
\vdots & \vdots & \vdots & \vdots & \vdots & \vdots & \vdots & \vdots & \vdots & \vdots & \vdots & \ddots & 0 \\
0 & 0 & 0 & 0 & 0 & 0 & 0 & 0 & 0 & 0 & 0 & 0 & 1
\end{bmatrix} \tag{3.31}$$

where

$$A = T_a^2(e^{-\Delta t/T_a} - 1) + T_a\Delta t$$

$$B = T_a(1 - e^{-\Delta t/T_a})$$

$$C = (e^{-\Delta t/T_a})$$

The discrete dynamics driving noise covariance is given by

$$\mathbf{Q}_d(t_k) = \int_{t_k}^{t_{k+1}} \boldsymbol{\Phi}(t_{k+1}, \tau)\mathbf{G}(\tau)\mathbf{Q}(\tau)\mathbf{G}^T(\tau)\boldsymbol{\Phi}^T(t_{k+1}, \tau)d\tau \tag{3.32}$$

3-17

which, for this filter, results in

$$\mathbf{Q}_{d=} \begin{bmatrix} D & 0 & 0 & E & 0 & 0 & G & 0 & 0 & 0 & 0 & \cdots & 0 \\ 0 & D & 0 & 0 & E & 0 & 0 & G & 0 & 0 & 0 & \cdots & 0 \\ 0 & 0 & D & 0 & 0 & E & 0 & 0 & G & 0 & 0 & \cdots & 0 \\ E & 0 & 0 & K & 0 & 0 & L & 0 & 0 & 0 & 0 & \cdots & 0 \\ 0 & E & 0 & 0 & K & 0 & 0 & L & 0 & 0 & 0 & \cdots & 0 \\ 0 & 0 & E & 0 & 0 & K & 0 & 0 & L & 0 & 0 & \cdots & 0 \\ G & 0 & 0 & L & 0 & 0 & M & 0 & 0 & 0 & 0 & \cdots & 0 \\ 0 & G & 0 & 0 & L & 0 & 0 & M & 0 & 0 & 0 & \cdots & 0 \\ 0 & 0 & G & 0 & 0 & L & 0 & 0 & M & 0 & 0 & \cdots & 0 \\ 0 & 0 & 0 & 0 & 0 & 0 & 0 & 0 & 0 & N & 0 & \cdots & 0 \\ 0 & 0 & 0 & 0 & 0 & 0 & 0 & 0 & 0 & 0 & N & \cdots & 0 \\ \vdots & \vdots & \vdots & \vdots & \vdots & \vdots & \vdots & \vdots & \vdots & \vdots & \vdots & \ddots & 0 \\ 0 & 0 & 0 & 0 & 0 & 0 & 0 & 0 & 0 & 0 & 0 & 0 & N \end{bmatrix} \tag{3.33}$$

wherethese values were taken from reference [24] and are defined as

$$D = \frac{1}{2}T_a^5 q_a(1 - e^{-2\Delta t/T_a}) + T_a^4 q_a \Delta t(1 - 2^{-\Delta t/T_a}) - T_a^3 q_a(\Delta t)^2 + \frac{1}{3}T_a^2 q_a(\Delta t)^3$$

$$E = T_a^4 q_a(\frac{1}{2}e^{-2\Delta t/T_a} - e^{-\Delta t/T_a} + \frac{1}{2}) + T_a^3 q_a \Delta t(e^{-\Delta t/T_a} - 1) + \frac{1}{2}T_a^2 q_a(\Delta t)^2$$

$$G = \frac{1}{2}T_a^3 q_a(1 - e^{-2\Delta t/T_a}) - T_a^2 q_a \Delta t e^{-\Delta t/T_a}$$

$$K = \frac{1}{2}T_a^3 q_a(-e^{-2\Delta t/T_a} + 4e^{-\Delta t/T_a} + 2\frac{\Delta t}{T_a} - 3)$$

$$L = -\frac{1}{2}T_a^2 q_a(-e^{-2\Delta t/T_a} + 2e^{-\Delta t/T_a} - 1)$$

$$M = -\frac{1}{2}T_a q_a(-e^{-2\Delta t/T_a} - 1)$$

$$N = q_N \Delta t$$

3.4 Floating-Point Filter Features

The floating-point filter includes a pre-filtering step, a tropospheric model, and adaptations to improve upon the performance of the baseline filter. These adaptations consisted of estimating errors in the tropospheric model and estimation of *LocataLite* position errors.

3.4.1 Pre-filter. A pre-filter function determined the number of available *LocataLites*, vector of available *LocataLites*, and base *LocataLite* for single-difference operations. The vector of available *LocataLites* was rank ordered by the signal-to-noise (SNR) measurement quality, with the base chosen as the *LocataLite* with the highest average SNR.

3.4.2 Filter Initialization. The state vector of the filter requires initialization before processing begins. For the position states, the ENU origin (0,0,0) serves as an adequate starting point. The velocity and acceleration states are assumed to be zero in all directions, since there is no assumed knowledge of movement at initialization. The clock bias and clock drift states also take on the zero assumption, as well as the tropospheric and position error states if included. This leaves the single-differenced floating-point ambiguities, which employ the following code-carrier difference.

$$N \approx \phi - \frac{\rho}{\lambda} \tag{3.34}$$

For single-differencing, this becomes

$$\Delta N \approx \Delta \phi^{1k} - \frac{\Delta \rho^{1k}}{\lambda} \qquad k = 2, 3, \cdots, n \tag{3.35}$$

3.4.3 LocataNet Adaptation. *LocataLites* possess an SNR measurement for each epoch which provides an indication of measurement quality. Although not ideal, this allowed a level of control to prevent increasingly poor measurements from entering the filter and allowed previously discounted *LocataLites* an avenue for inclusion. Once

the SNR value for a measurement is deemed worthy, the measurement is included in the measurement vector. The current revision of the *LocataNet* inhibits traditional cycle slip detection due to the dominance of the frequency lock loop (FLL) and lack of a true phase lock loop (PLL) (i.e., a loop that attempts to drive the phase difference between incoming and receiver generated values to zero). This also prevents integer ambiguity resolution. Therefore, the SNR measurements determined which *LocataLites* remained in view, or were included/excluded before measurement incorporation and filtering.

When *LocataLites* drop below the SNR threshold, the filter re-initializes the appropriate state estimate and the rows and columns associated with this *LocataLite* in the covariance matrix. For example, if *LocataLites* 1 through 5 retained SNR values above threshold with *LocataLite* 1 as the single-difference base, sample ambiguity state values might be

$$x_{12} = \Delta N^{12} = 150075.54$$
$$x_{13} = \Delta N^{13} = 160805.47$$
$$x_{14} = \Delta N^{14} = 164483.71$$
$$x_{15} = \Delta N^{15} = 127251.37$$

These four ambiguity states would be in states 12 through 15, because the first 11 states represent the 3 position, 3 velocity, 3 acceleration, and 2 clock states. If *LocataLite* 4 falls below the threshold, the new ambiguity vector remains the same, but the ambiguity value (ΔN^{14}) would not be updated until *LocataLite* 4 obtains SNR values above the threshold. The covariance matrix $\mathbf{P}$ also requires adjustment. Consider a case in which the 4-by-4 partition of the ambiguity variances and covariances is

$$\mathbf{P} = \begin{bmatrix} 0.00059357 & 0.00024635 & 0.00031054 & 0.0004863 \\ 0.00024635 & 0.00036501 & 0.0000279 & 0.0001695 \\ 0.00031054 & 0.00002791 & 0.00032214 & 0.00031669 \\ 0.0004863 & 0.0001695 & 0.00031669 & 0.00050136 \end{bmatrix}$$

In order to hold the ΔN^{14} state the second to last row and second to last column are re-initialized. As a result, the covariance becomes

$$P = \begin{bmatrix} 0.00059357 & 0.00024635 & 0 & 0.0004863 \\ 0.00024635 & 0.00036501 & 0 & 0.0001695 \\ 0 & 0 & 1621 & 0 \\ 0.0004863 & 0.0001695 & 0 & 0.00050136 \end{bmatrix}$$

which represents the initialized value of $\left(\frac{5}{\lambda} cycles\right)^2$. The off-diagonal terms for the row and column are set to zero. The measurement vector no longer contains a measurement for *LocataLite* 4, thus requiring a change in **H** as well, removing the corresponding row for the absence of measurement 4. This allows the filter to maintain constant state and covariance sizes without using measurements deemed too poor.

3.4.4 Tropospheric Model Error State. The errors in the tropospheric model include measurement errors in the sensors, atmospheric errors due to ground effects, and the use of estimated positions of the transmitters and receivers. In addition, the model used to predict each of these errors remains imperfect, thus even given perfect measurements, a perfect model does not exist.

The first error source is the set of errors due to imprecise instruments for measuring atmospheric pressure, temperature, and relative humidity. These errors will affect all measurements by roughly the same percentage.

The second error is due to ground effects from foliage and buildings. The height of a typical test mission could be 2500 meters above the earth's surface, so ground effects that only affect the first 25 meters represent 1 percent of the total signal range. However for missions at or near ground, such as landing, the tropospheric effects can be more significant.

The third error is due to estimated positions of the transmitters and receivers to calculate the tropospheric error. Because these errors are in the centimeter range, their effect is almost insignificant to the total error of the tropospheric model.

An additional state added to the filter attempts to account for the remaining tropospheric errors after a model has been applied. This state represents an error percentage for the measurements modeled as a first order Gauss-Markov process. The state is modeled as a percentage to account for the inaccuracies described above which postulate the remaining error is of the same order as the errors found, but some percentage related to the original errors modeled [6]. The resulting measurement model equations become

$$\rho = r + c(\delta t_u - \delta t_{LL}) + T(1 + T_r) + v_\rho \tag{3.36}$$

$$\Delta\phi^{1k} = \frac{1}{\lambda}\left[(r^1 - T^1) - (r^k - T^k)\right] + \Delta N^{1k} + \Delta T^{1k}(T_r) + v_{\Delta\phi} \quad k = 2, 3, \cdots, n \tag{3.37}$$

The tropospheric scale-factor was modeled as a first order Gauss-Markov process

$$\dot{\mathbf{x}}_{12} = (-1/T_t)\mathbf{x}_{12} + w_t(t)$$

with associated dynamic driving noise

$$E\left\{w_t(t)w_t(t+\tau)\right\} = \frac{2\sigma_t^2}{T_t}\delta(\tau) = q_t\delta(\tau) \tag{3.38}$$

The correlation time, T_t, and variance, σ_t^2, are based on the anticipated error percentages and time correlations from [6]. A value of 1 hour (3600 seconds) for T_t to account for typical changes in atmospheric effects and 0.2 (20 percent) for σ_t attempt to handle the "worst case" error percentage. These values were determine via tuning under simulated conditions. The inclusion of the tropospheric scale-factor state augments the state vector, creating

$$\mathbf{x} = \left[\mathbf{E}\ \mathbf{N}\ \mathbf{U}\ \dot{\mathbf{E}}\ \dot{\mathbf{N}}\ \dot{\mathbf{U}}\ \ddot{\mathbf{E}}\ \ddot{\mathbf{N}}\ \ddot{\mathbf{U}}\ \mathbf{c_b}\ \mathbf{c_d}\ \mathbf{T_r}\ \mathbf{\Delta N^{12}}\ \ldots\ \mathbf{\Delta N^{1n}}\right]^{\mathbf{T}} \tag{3.39}$$

where the state and dynamic driving noise are given in Equations (3.42) and (3.43) respectively. Equation (3.18) now includes the following addition of

$$\Delta T_r = \Delta T^{1k}(x_{12}) \tag{3.40}$$

and the resulting $\mathbf{H}$ matrix includes

$$\left.\frac{\partial h[\mathbf{x}, t_i]}{\partial x_{12}}\right|_{\mathbf{x}=\hat{\mathbf{x}}(t_i^-)} = \frac{\Delta T^{1k}}{\lambda} \tag{3.41}$$

   3.4.5   LocataLite Position Error States.   The *LocataLite* position error states (PES) are modeled as random walks, just as the floating-point ambiguities in Section 3.3.1.

$$\dot{x}_{13} = w_{LL_E^1}$$

$$\dot{x}_{14} = w_{LL_N^1}$$

$$\vdots$$

$$\dot{x}_{(11+(n-2))} = w_{LL_E^n} \tag{3.42}$$

$$\dot{x}_{(11+(n-1))} = w_{LL_N^n} \tag{3.43}$$

$$\tag{3.44}$$

where 1 is given as the base and n represents the total number of *LocataLites*. The process noise has an autocorrelation kernel given by

$$E\{w_{LL_E^n}(t)w_{LL_E^n}(t+\tau)\} = q_{LL}\delta(\tau)$$

$$q_{LL} = 5 \times 10^{-11}(\mathrm{m}^2/\sec)$$

This yields

$$\mathbf{x} = \begin{bmatrix} \mathbf{E} \ \mathbf{N} \ \mathbf{U} \ \dot{\mathbf{E}} \ \dot{\mathbf{N}} \ \dot{\mathbf{U}} \ \ddot{\mathbf{E}} \ \ddot{\mathbf{N}} \ \ddot{\mathbf{U}} \ \mathbf{c_b} \ \mathbf{c_d} \ \mathbf{T_r} \ \mathbf{LL_E^1} \ \mathbf{LL_N^1} \ldots \ \mathbf{LL_E^n} \ \mathbf{LL_N^n} \ \mathbf{\Delta N^{12}} \ \ldots \ \mathbf{\Delta N^{1n}} \end{bmatrix}^\mathbf{T}$$

(3.45)

providing the full state vector with all possible states. Updating Equations (3.1) and (3.3) to include the tropospheric scale-factor and the *LocataLite* position errors yields

$$\rho = r + c(\delta t_u - \delta t_{LL}) + T(T_r) + e_{rec}^{LL} \cdot [LL_E \ LL_N \ 0] + v_\rho \qquad (3.46)$$

$$\Delta\phi^{1k} = \lambda^{-1}(\Delta r^{1k} + \Delta T^{1k}(T_r) + \Delta e_{rec}^{LL^{1k}} \cdot [LL_E^1 - LL_E^k \ LL_N^1 - LL_N^k \ 0] + v_{\phi^{1k}}) + \Delta N^{1k}$$

(3.47)

where $e_{rec}^{LL} \cdot [LL_E \ LL_N \ 0]$ represents the *LocataLite* position error vector composed of the east and north *LocataLite* position errors.

3.5   Simulator Design

This research developed a Kalman filter based processing algorithm for calculating position and floating-point ambiguities for the *LocataLites*, as well as an associated simulator for confidence and error analysis. The simulator created perfect measurements (code pseudorange and carrier-phase) which could then be manipulated by known errors of varying type. This allowed quality checking of the Kalman filter in every aspect to ensure live data accuracy remained at a premium. Additionally, investigation of specific error sources such as tropospheric and position error highlighted similar events in live data and enhanced Kalman filter tuning. Lastly the simulator proved a valuable tool in determining *LocataLite* placement in upcoming tests to predict dilution of precision (DOP) values yielding better placement. The overall simulator algorithm is depicted in Figure 3.2.
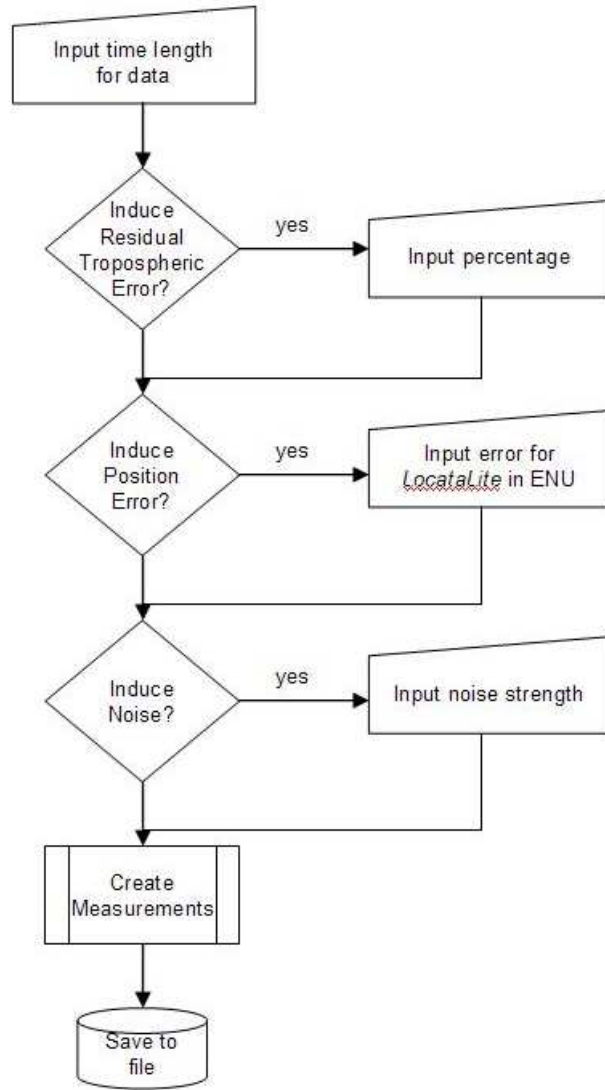
Figure 3.2:   Simulator algorithm

3.5.1 Simulated Measurement Noise.   Using a predetermined trajectory and known *LocataLite* positions allowed creation of perfect pseudorange and carrier-phase measurements. To simulate the noise encountered in real measurements, a zero mean white Gaussian noise with a standard deviation (1-σ) of 0.02 cycles for carrier-phase measurements and 2.6 meters for pseudorange measurements was added.

3.5.2 Simulated Tropospheric Delay.   The simulated tropospheric delay values stem from the same model correcting the measurements in the actual filter for real

measurements. In simulation, the delays in meters are simply added to the perfect pseudorange measurements and ultimately the carrier-phase measurements, which result from dividing the simulated pseudorange measurement by λ.

3.5.3 Simulated Tropospheric Scale-Factor Error. The calculated tropospheric delay terms in meters receive an additional percentage of the calculated tropospheric delay value to simulate the inclusion of the remaining tropospheric delay. For example, if the calculated tropospheric delay for a pseudorange was found to be 7cm, a 3 percent scale-factor error means that 3 percent of 7cm (.21cm) would be added to 7cm resulting in a tropospheric delay value of 7.21cm.

3.5.4 Simulated LocataLite Position Errors. The known locations of the *LocataLites* were simply modified in the E,N, or U direction by small values before the pseudorange and carrier-phase measurement creation. This allowed investigation into specific *LocataLite* position errors and the ability to distinguish errors in a particular *LocataLite* for a particular direction (E,N, or U).

3.6   Chapter Summary

This chapter outlined the Floating Point *LocataLite* Kalman Filter along with associated steps to produce position, velocity, acceleration, and ambiguity terms for a *LocataNet*. Filter preparation included measurement setup, noise characteristics, tropospheric model application, and initialization. Additions to the filter included the tropospheric scale-factor state and position error states for each *LocataLite*.

IV. Results

4.1 Overview

This chapter presents results for both real and simulated data to evaluate algorithm performance. The first section covers simulation parameters and test cases in order to confirm filter operation under perfect conditions with known induced errors. The next section describes simulations designed to mimic real data concerns and evaluates filter performance under these conditions. Finally, an analysis of real data performance and a comparison of simulated performance versus real performance is conducted. The chapter concludes with measurement analysis to determine discrepancies between expected and realized performance.

4.2 Simulation Results With Perfect Measurements

This section describes the simulation trajectory and associated parameters which define filter performance under perfect conditions and known parameters. In order to create a simulation comparable to the real data available for testing, the DGPS track (Figure 4.1) from a test run provides an excellent source to create simulated measurements. The post-processed DGPS solution along with the position of the *LocataLites* allow creation of code pseudorange and carrier-phase measurements. For creating code measurements, the equation is

$$\rho = \sqrt{(x_{LL} - X_{DGPS})^2 + (y_{LL} - Y_{DGPS})^2 + (z_{LL} - Z_{DGPS})^2} + T + v \qquad (4.1)$$

where

$$\rho = \text{pseudorange measurement (meters)}$$

$$x_{LL} = \text{ECEF x position of the } \textit{LocataLite}$$

$$y_{LL} = \text{ECEF y position of the } \textit{LocataLite}$$

$$z_{LL} = \text{ECEF z position of the } \textit{LocataLite}$$

$$X_{DGPS} = \text{ECEF X position of DGPS solution}$$

$$Y_{DGPS} = \text{ECEF Y position of DGPS solution}$$

$$Z_{DGPS} = \text{ECEF Z position of DGPS solution}$$

$$T = \text{error due to tropospheric delay (meters)}$$

$$v_{\rho} = \text{error in pseudorange due to receiver noise (meters)}$$

For this perfect measurement case, the measurement noise (v_{ϕ}) was set to zero. The corresponding carrier-phase measurements are the pseudorange values divided by the wavelength. The tropospheric component for simulations represents values from the application of the tropospheric correction model discussed previously in Section 3.2.3. The filter then applies the same values from the tropospheric correction model during processing, resulting in zero net effect for simulations. Figure 4.1 depicts the simulated trajectory and *LocataLite* positions.
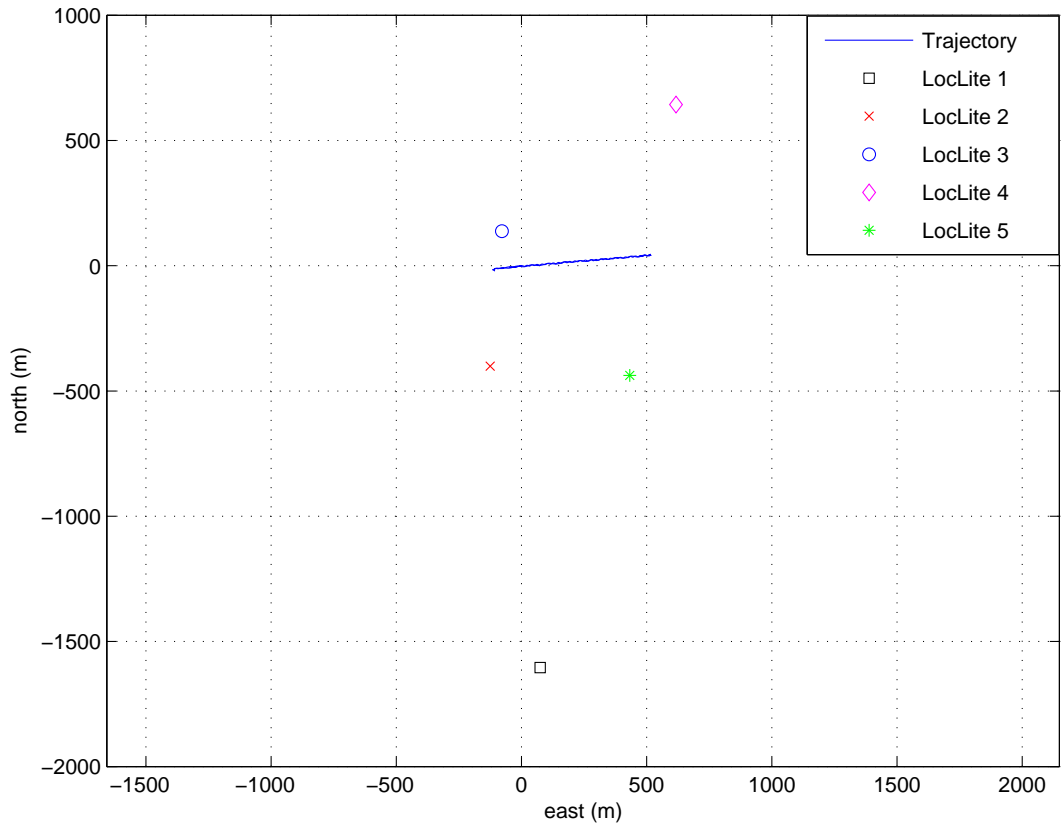
Figure 4.1:   Simulated trajectory and *LocataLite* positions

For the simulations and real data runs in this research, only carrier-phase mea-
surements were used for solutions. The ability to provide both code and carrier-phase
solutions does exist, but the focus remains on carrier-phase solutions due to concerns
about multipath-induced biases in the real pseudorange measurements.
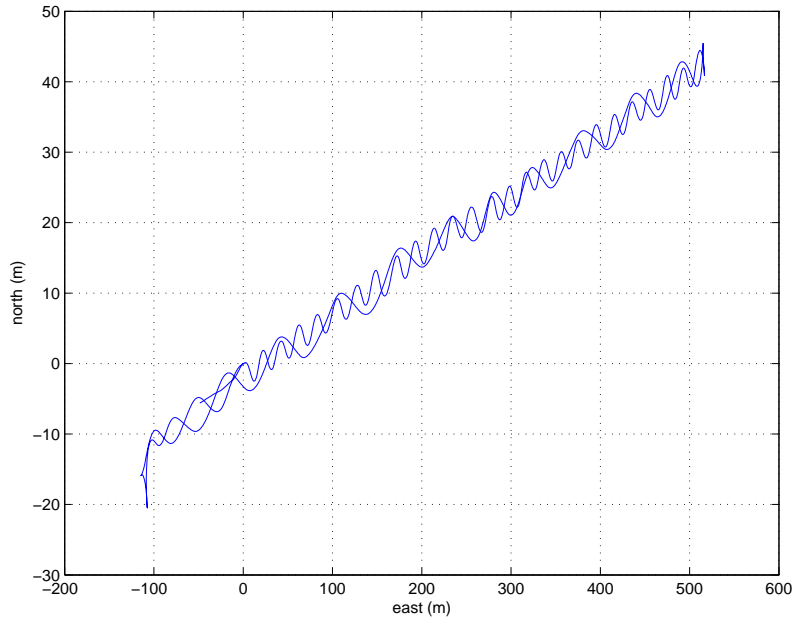
Figure 4.2:   Simulated 2D trajectory with perfect measurements

Figure 4.2 depicts the solution trajectory on a two dimensional (2D) scale, along with the "truth", which cannot be clearly distinguished on this scale. The truth trajectory combines the two GPS trajectories by matching their position solutions to GPS time, and yields the trajectory from which the measurements for simulation are created.

For the horizontal error, Figure 4.3 depicts the error defined as the Euclidian distance between the true and computed positions in the horizontal directions at the same epoch. This metric renders an initial indication of filter quality, clearly depicting that, although perfect measurements may be given to the filter, the filter models are not perfect. Figure 4.4 further defines specific errors in the east and north directions of the ENU frame.
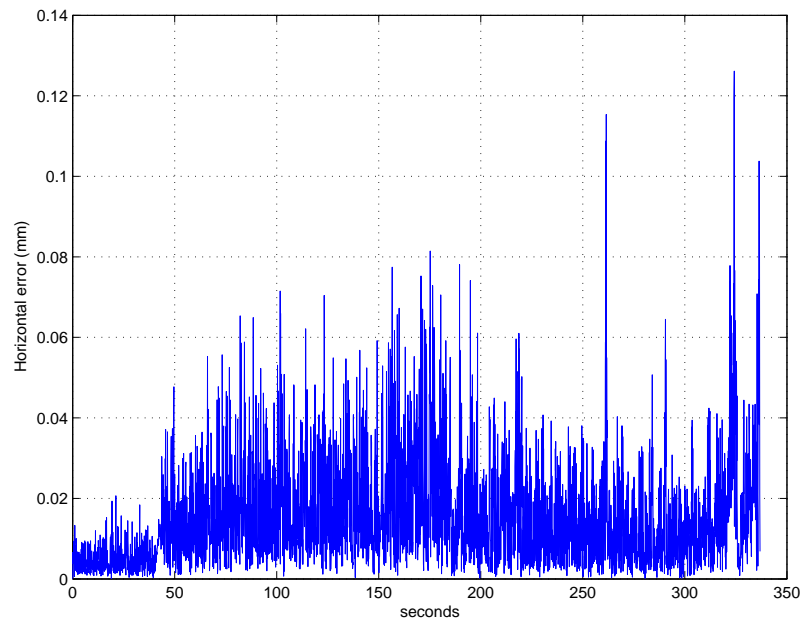
Figure 4.3:   Simulated horizontal error with perfect measurements
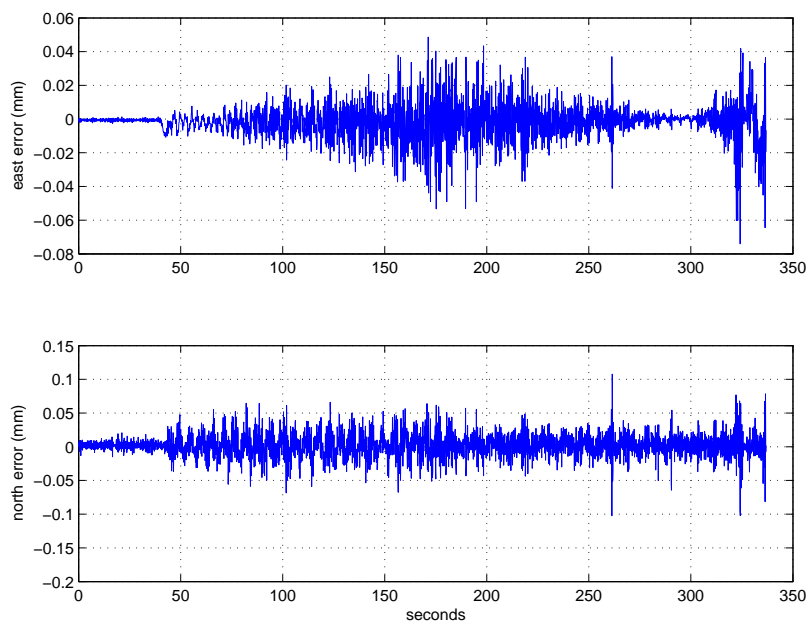
Figure 4.4:   Simulated east and north error with perfect measurements

4-5

Although the figures do not reflect perfect performance given perfect measurements, the filter remained tuned for real data runs and was not re-tuned for perfect measurements. Due to the poor geometry of the *LocataLite* positions, altitude information incorporated as a measurement greatly increases the performance of the filter.

Figures 4.5 and 4.6 represent the same simulation run with the truth altitude incorporated.
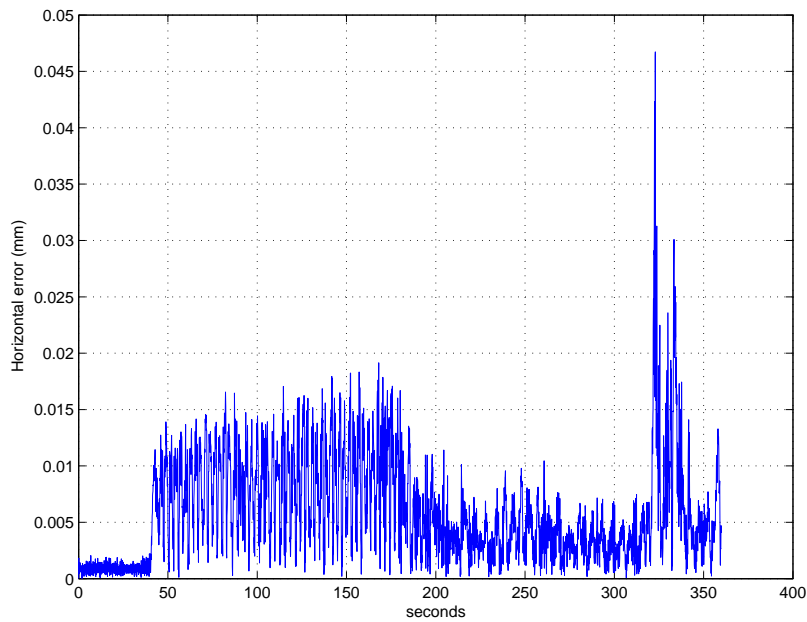
Figure 4.5:   Simulated horizontal error with perfect measurements and known altitude

These figures depict the best level of performance the filter achieved, clearly showing the measurement correlations with the trajectory run. From zero to 40 seconds the vehicle did not move, then began tight back and forth movements along the road until approximately 180 seconds. From 180 to 320 seconds the vehicle changed to a more elongated back and forth movement back down the road. The worst measurement performance lies at the turnaround portion near the end of the test run (320 seconds)

where the geometry becomes the poorest due to the location of the *LocataLites*. These figures represent baseline filter performance for comparison with future simulation runs and real data runs which all include the altitude incorporated as a measurement to help overcome the poor geometry.
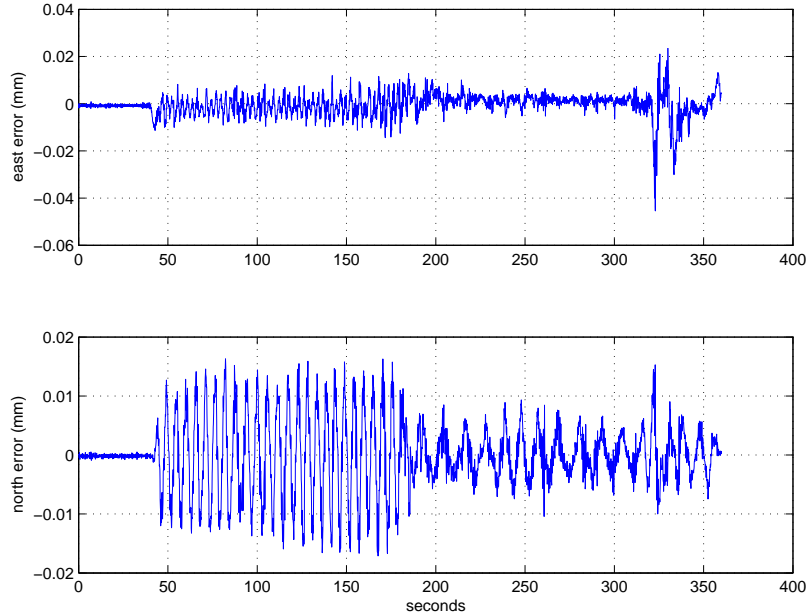
Figure 4.6:   Simulated east and north error with known altitude

4.2.1   Error incorporation in simulations.   Since signal-to-noise ratio (SNR) values provide the metric for determining inclusion or exclusion of a *LocataLite* from the measurement sample, verification of the process under typical conditions is needed. Actual SNR measurements from real data runs provided an excellent source for simulation. Figure 4.7 depicts the SNR values for each *LocataLite* over the test run.
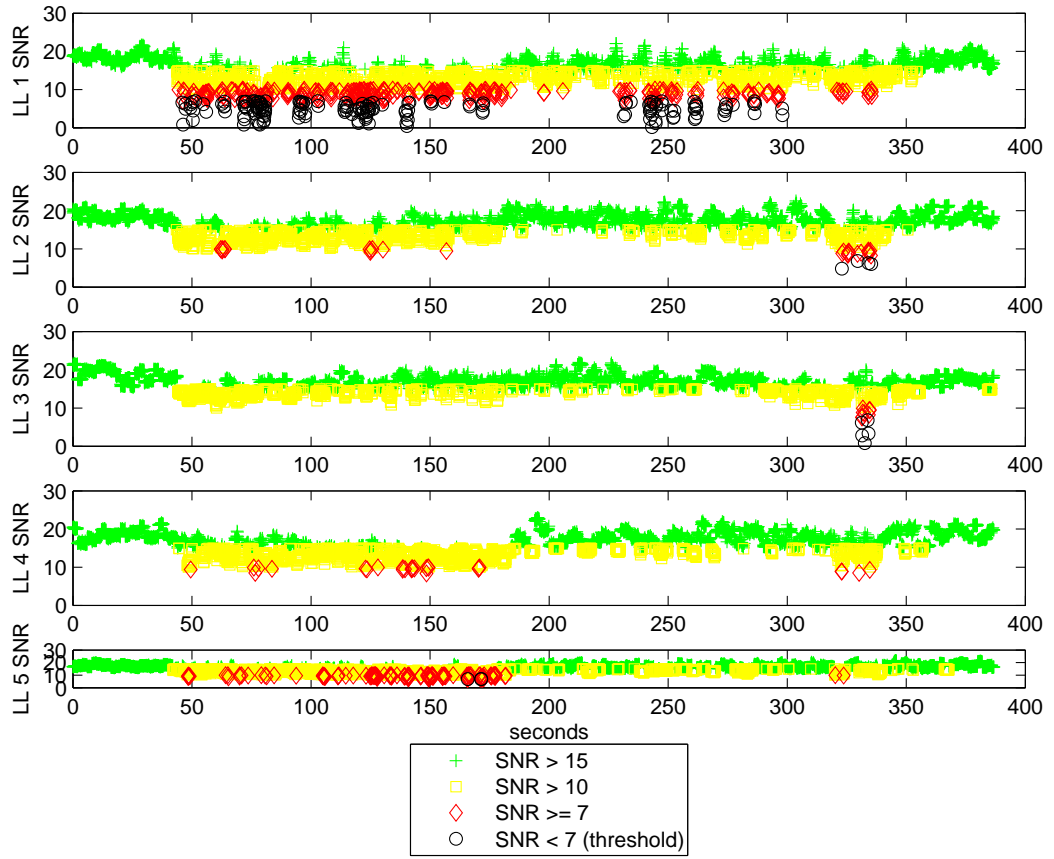
Figure 4.7: Real SNR values used in both simulation and real data runs; measurements with SNR < 7 were not used

When the SNR value for a measurement falls below the threshold value, the measurement is no longer used for the position solution. The measurement vector shrinks to reflect the lost measurement, yet the single-differenced ambiguities are simply reinitialized as in Equation (3.35) until the measurement becomes available again. This allows the state vector to remain the same size for comparable analysis of the ambiguities. While the SNR measurements do not reflect actual cycle slips, they are handled in much the same way.

Figures 4.8 and 4.9 show little difference from figures 4.5 and 4.6, demonstrating effective measurement management.
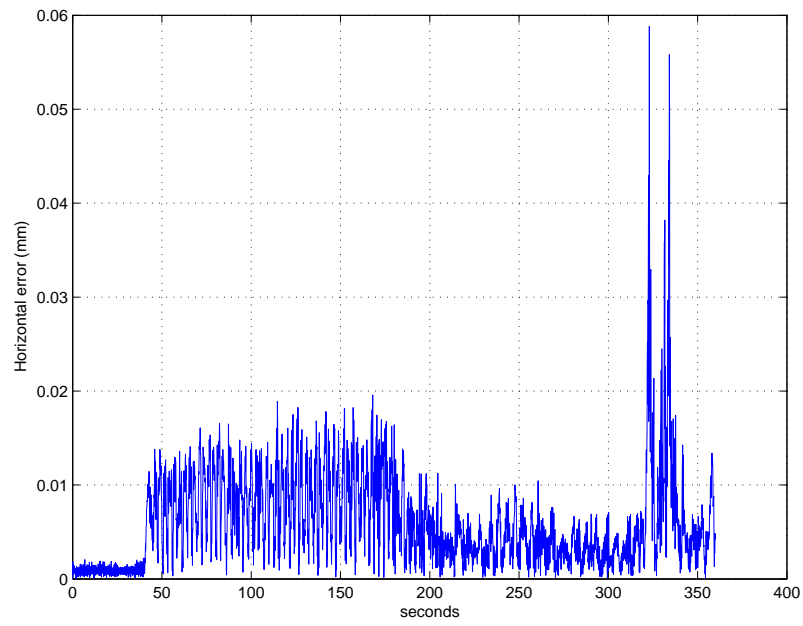
Figure 4.8:   Simulated horizontal error with real SNR values and perfect measurements
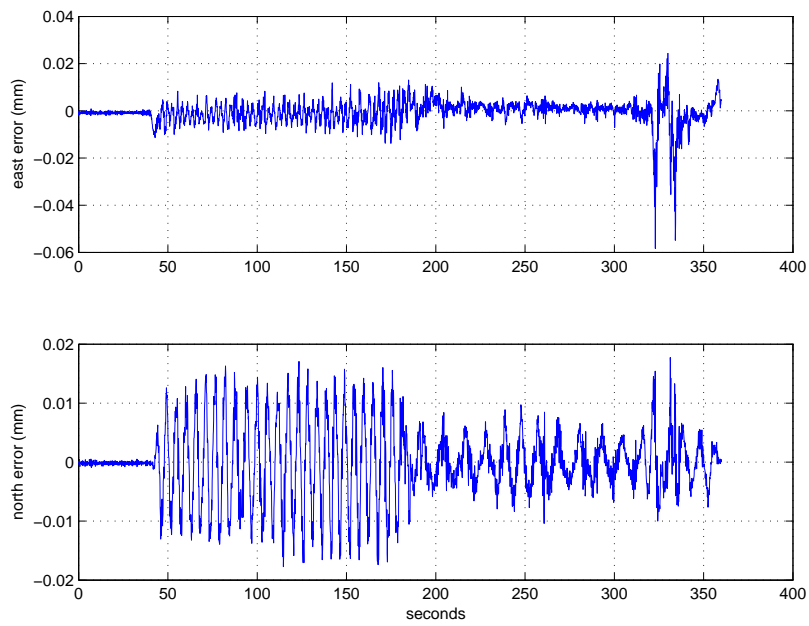
Figure 4.9:   Simulated east and north error with real SNR values

4-9

With this information, all further simulation runs include actual SNR values in an attempt to keep the simulations as close as possible to real data.

4.3 Simulated Results With Added Noise

With confirmation the filter and all included functions work properly, simulations designed to account for real world conditions such as measurement noise, residual tropospheric effects, and position errors were conducted to characterize filter performance. These simulations represent Monte Carlo analysis of the filter in which the filter is measured against "truth" data instead of a truth model (i.e., a higher order linear filter).

4.3.1 Simulated Measurement Noise.   The position errors shown in Figure 4.10 for a ten run Monte Carlo analysis depicts the typical case for added measurement noise consisting of a zero-mean white Gaussian noise with a 1-σ value of 0.02 cycles for carrier-phase measurements.
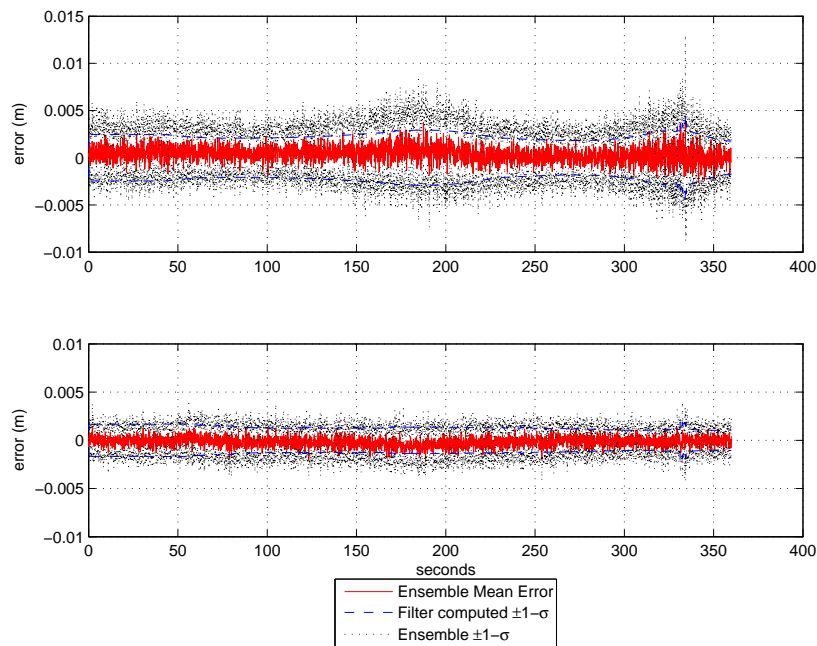
Figure 4.10:   Ten-run Monte Carlo results, position error with no other errors

4-10

The ensemble mean error represents the mean of the errors for all runs at corresponding time indices. The ensemble 1-σ represents the standard deviation of the errors for all runs. The filter-computed 1-σ represents the covariance values in the filter. Clearly measurement noise signifies a large factor by decreasing the accuracy of the filter from tens of micrometers to centimeters. The plot shows good agreement between the ensemble and filter-computed standard deviations, which represents proper tuning values.

4.3.2   Simulated Tropospheric Scale-Factor Error.   As stated in Section 3.5.3, the additional tropospheric delay typifies a percentage of the true tropospheric delay. The additional tropospheric percentage error along with the simulated measurement noise resembles the expected error. Figure 4.11 illustrates a ten-run Monte Carlo analysis for a random tropospheric scale-factor generated as a zero mean Gaussian random variable with zero mean and a 1-σ value of 10 percent.
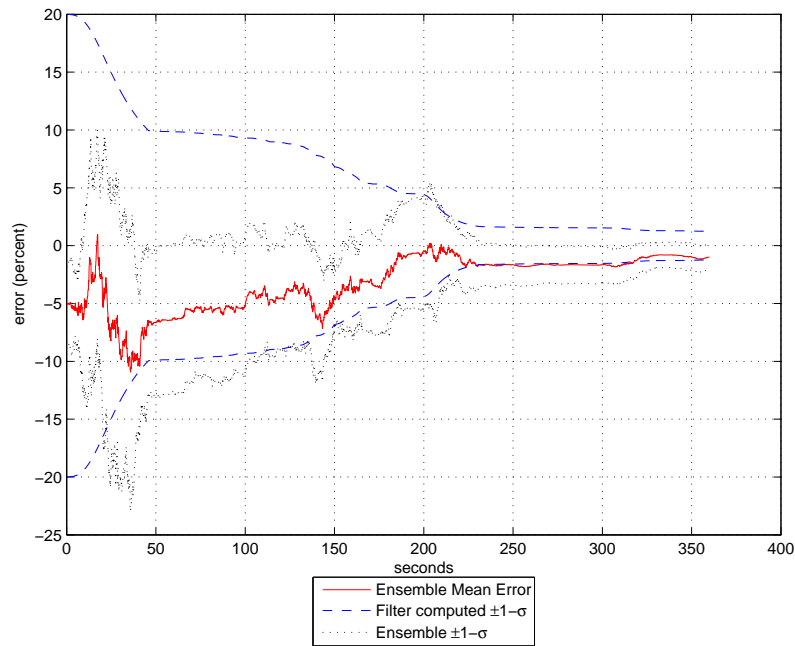
Figure 4.11:   Ten-run Monte Carlo results, tropospheric scale-factor

The ensemble mean represents the mean of all the Monte Carlo runs after the original error percentage has been subtracted. The filter captures a significant portion of the error with some agreement between the filter-computed and ensemble standard deviations.

4.3.3 Simulated LocataLite Position Errors. *LocataLite* position error estimation discussed in Section 3.5.4 requires observability in all directions (E,N, and U) in order to determine the error properly. Even under perfect conditions, the geometry utilized for this research possesses poor vertical characteristics, therefore no attempt was made to estimate vertical position errors. However, estimation for E and N look promising for each *LocataLite* and merited investigation. An initial ten-run Monte Carlo analysis with no position errors revealed Figures 4.12 and 4.13. The initial position error states values were set to zero, assuming no *LocataLite* position error in any direction.
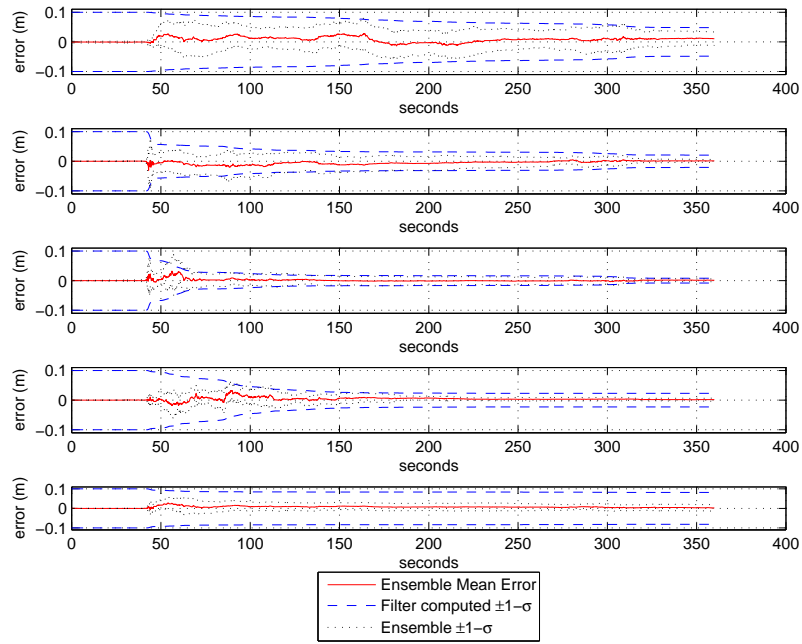
Figure 4.12:   Ten-run Monte Carlo results, *LocataLite* east position error estimates with no *LocataLite* position errors, plot order *LocataLite* 4,2,3,5,1
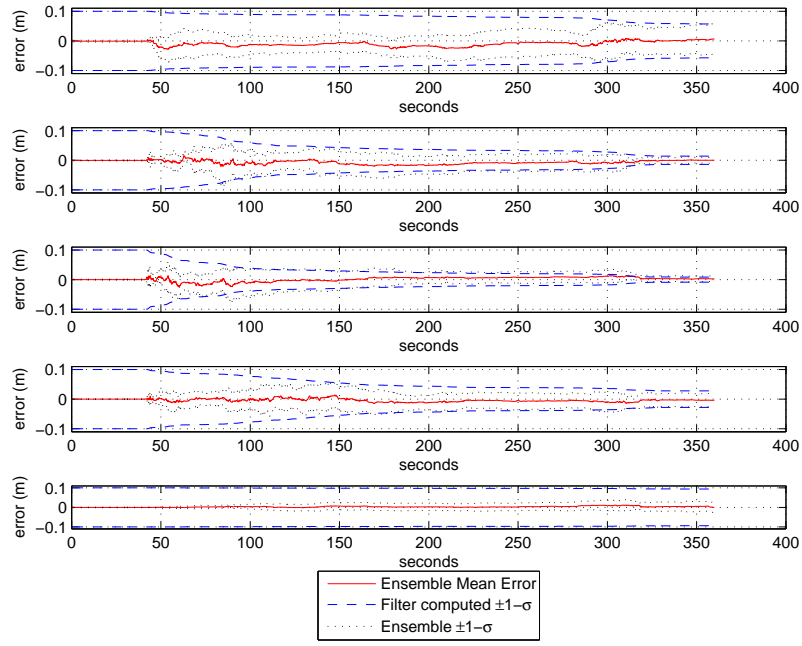
Figure 4.13: Ten-run Monte Carlo results, *LocataLite* north position error estimates with no *LocataLite* position errors, plot order *LocataLite* 4,2,3,5,1

Figures 4.12 and 4.13 provide insight into whether the error will be distinguishable or not using these state estimates. In the easting plot, the collapse of the filter-computed standard deviations shows promise of properly estimating an easting error in *LocataLites* 2, 3, and 5, since the ensemble standard deviations collapse as well. The filter-computed standard deviations show *LocataLite* 4 clearly indicates a lack of observability in the state, while *LocataLite* 1 shows some improvement but not enough to estimate the error with confidence. For the northing error, the confidence is less for all *LocataLites*. *LocataLites* 2 and 3 still show some confidence, but *LocataLites* 1, 4, and 5 remain difficult to estimate.

In order to estimate the *LocataLite* position errors deemed distinguishable, the filter sets the indistinguishable states to zero. To accomplish this, the values in the **H** matrix must be manually set to zero for *LocataLites* 4 and 1 in the east direction, and 4, 5, and 1 in the north direction. This allows the filter to compute the *LocataLite*

4-13

position error estimates in the *LocataLites* without attempting to estimate position errors in those determined to be indistinguishable.

LocataLites 2, 3, and 5 shown in Figures 4.14-4.18 provide the *LocataLite* position error estimates for a ten-run Monte Carlo using zero mean Gaussian random variables with 1-σ values of 10cm. Recall that *LocataLite* 5 in the north direction is not being estimated.
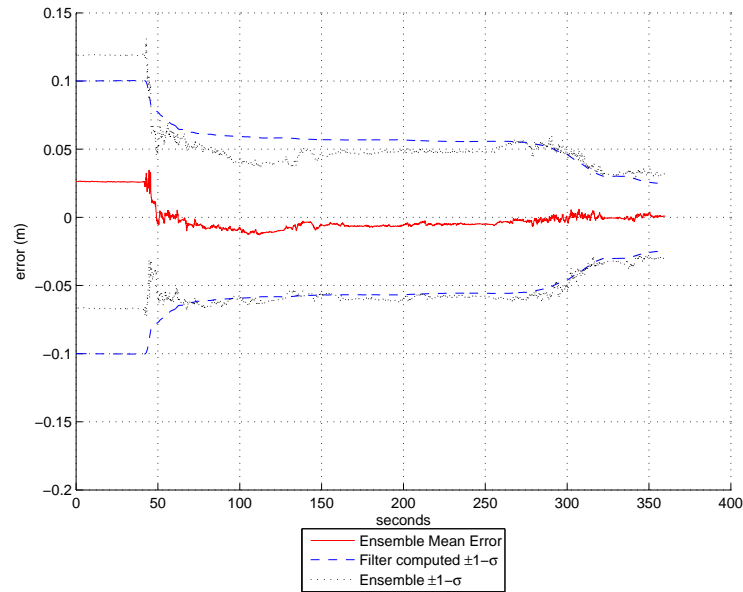
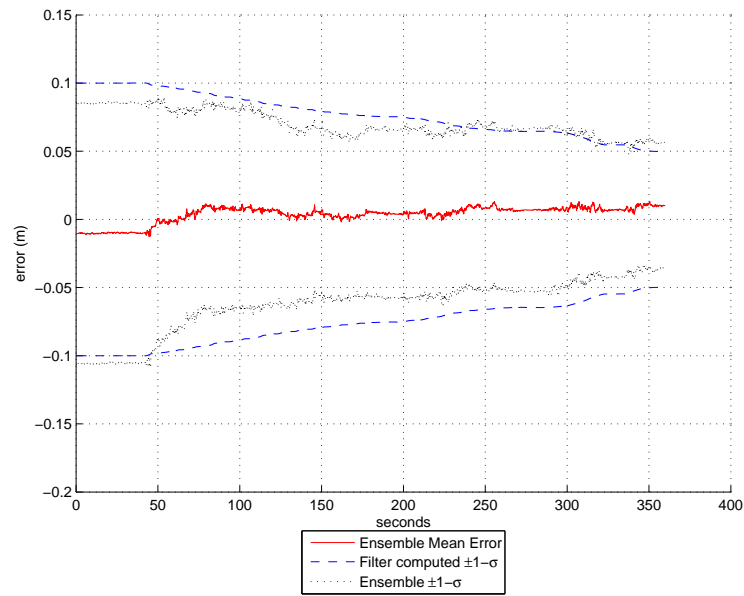

Figure 4.14:   Ten-run Monte Carlo results, *LocataLite* 2 estimated east position error

4-14

Figure 4.15:   Ten-run Monte Carlo results, *LocataLite* 2 estimated north position error
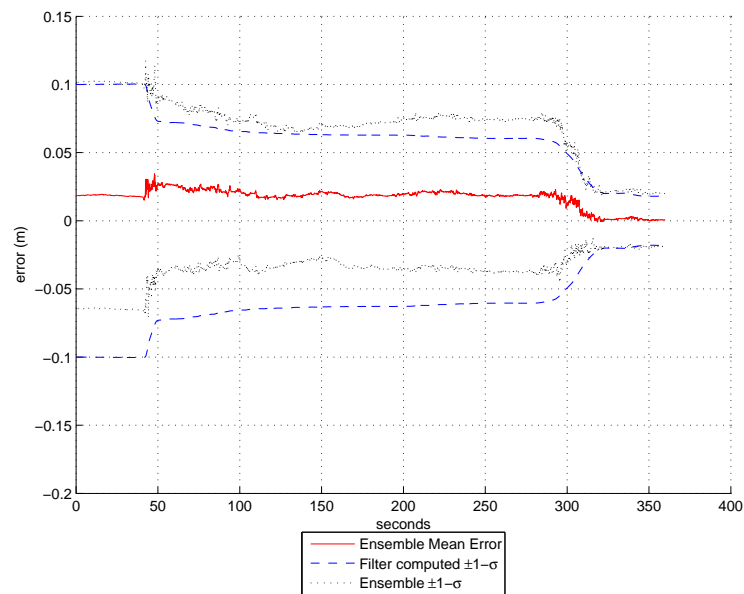
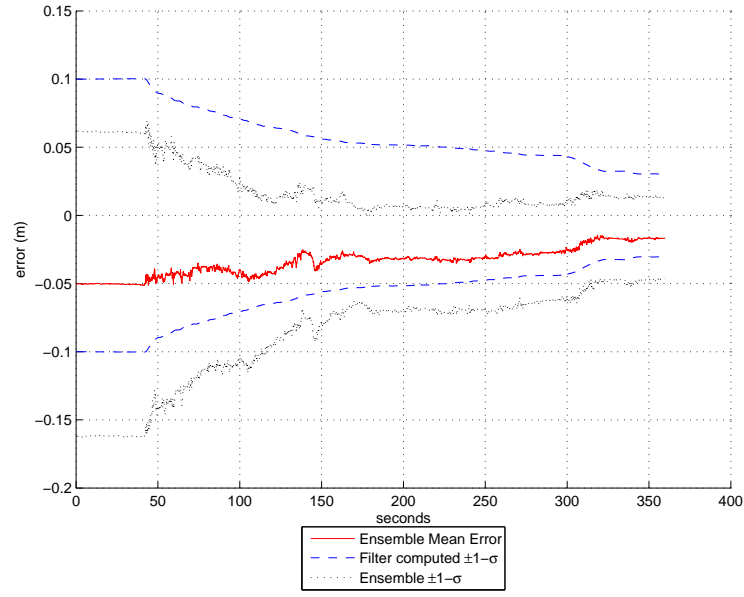Figure 4.16:   Ten-run Monte Carlo results, *LocataLite* 3 estimated east position error

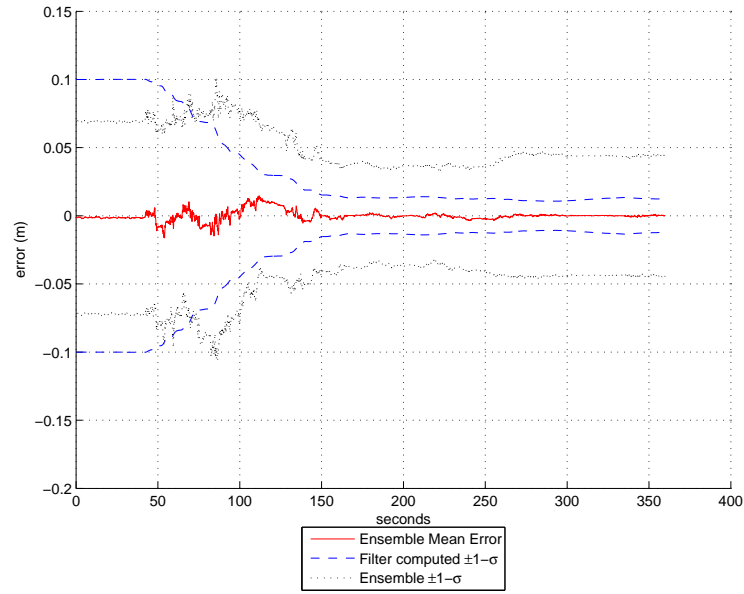Figure 4.17:   Ten-run Monte Carlo results, *LocataLite* 3 estimated north position
error

Figure 4.18:   Ten-run Monte Carlo results, *LocataLite* 5 estimated east position
error

4-16

The *LocataLite* position error estimates demonstrate the ability to resolve varying *LocataLite* position errors with reliable accuracy. The filter-computed and ensemble standard deviations display good agreement, indicating suitable tuning parameters.

This information requires the first filter run with the position error states (PES) to be used for analysis only, to determine which *LocataLites* and directions will be distinguishable. Then the indistinguishable *LocataLites* will be "locked down" in the filter to prevent them from affecting the error estimates. Similar performance could be achieved by using an optimal smoother, but is not included in this research.

4.3.4 Tropospheric Scale-Factor and LocataLite Position Errors. The final Monte Carlo analysis attempts to resolve both the tropospheric scale-factor and the *LocataLite* position errors at the same time. Potentially, this represents the complete solution for error mitigation and maximized performance. Figures 4.19-4.24 depict the simultaneous estimation of the tropospheric scale-factor and the *LocataLite* position errors.
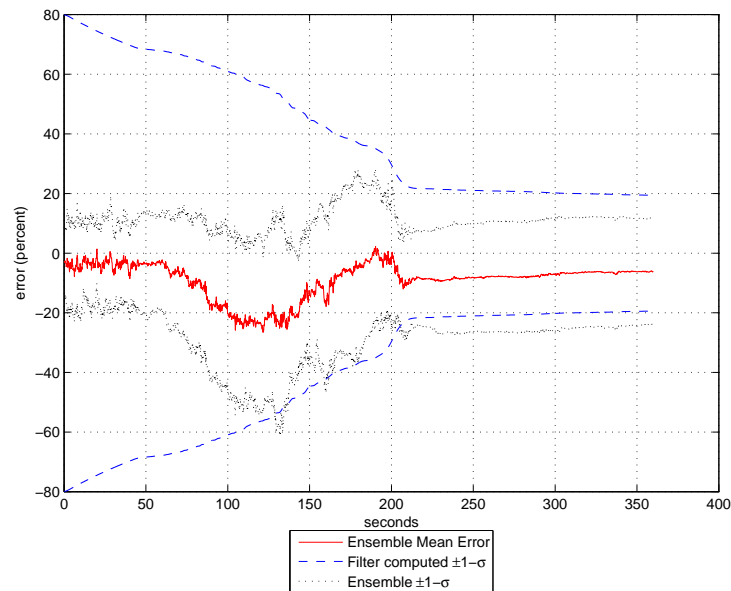

Figure 4.19:   Ten-run Monte Carlo results, estimated tropospheric scale-factor error
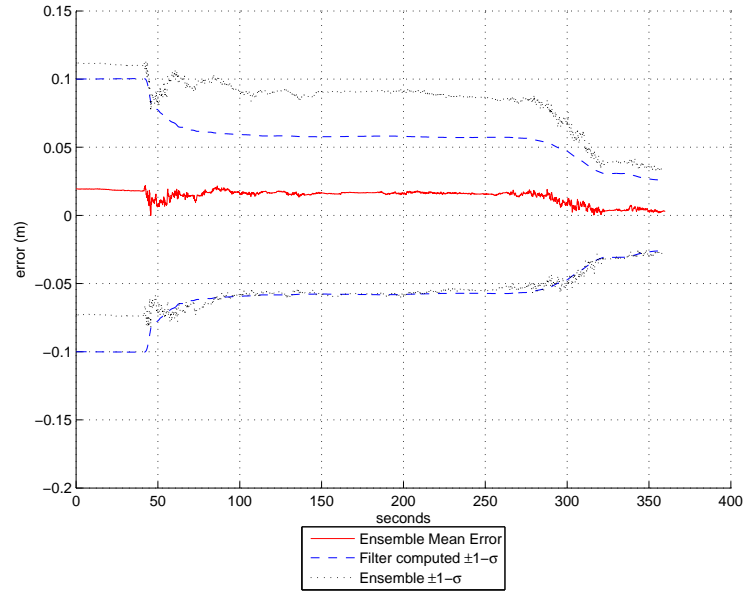
Figure 4.20:   Ten-run Monte Carlo results, *LocataLite* 2 estimated east position error, tropospheric scale-factor included
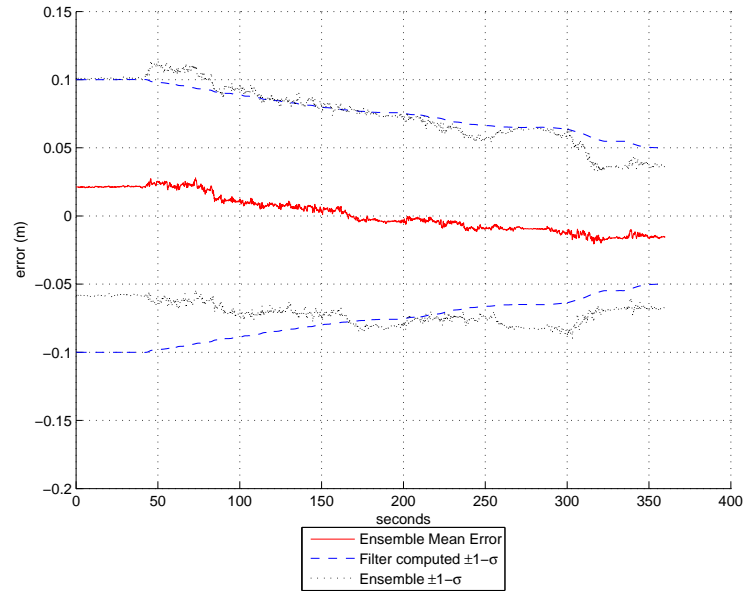

Figure 4.21:   Ten-run Monte Carlo results, *LocataLite* 2 estimated north position error, tropospheric scale-factor included
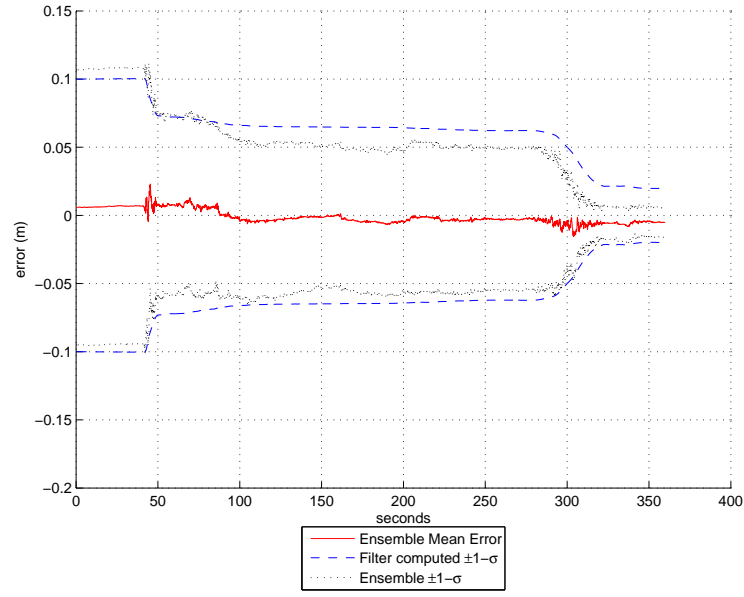
4-18

Figure 4.22: Ten-run Monte Carlo results, *LocataLite* 3 estimated east position error, tropospheric scale-factor included
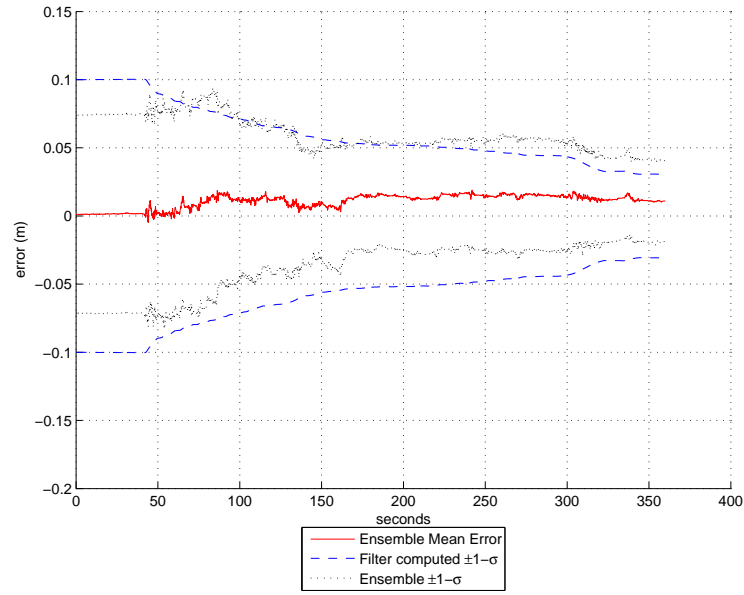

Figure 4.23: Ten-run Monte Carlo results, *LocataLite* 3 estimated north position error, tropospheric scale-factor included
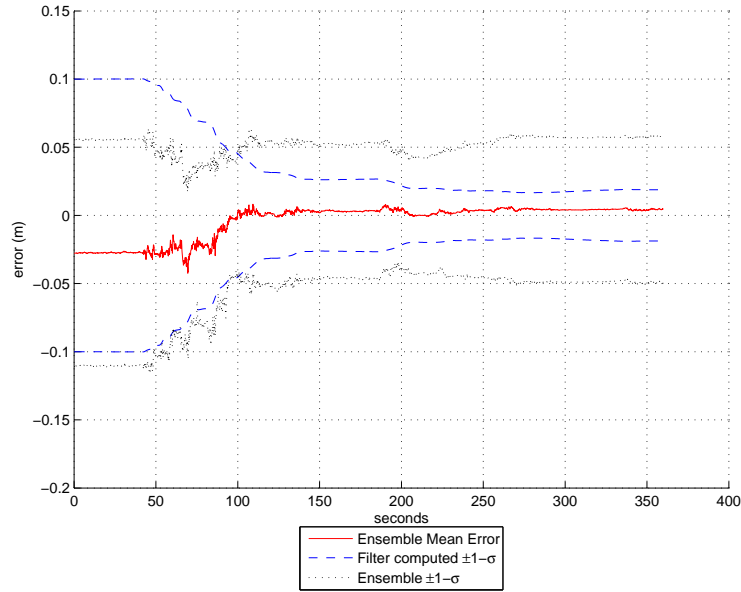
Figure 4.24: Ten-run Monte Carlo results, *LocataLite* 5estimated east position error, tropospheric scale-factor included

While the filter does resolve the errors to a reasonable level, performance in all estimated states is degraded compared to estimating the tropospheric scale-factor and *LocataLite* position errors separately. Closer inspection of the filter-computed and ensemble standard deviations for Figure 4.11 and 4.19 exposes a severe lack of ability to estimate the tropospheric scale-factor while simultaneously estimating the *LocataLite* position errors. For this particular data set, the *LocataLite* position errors must be estimated before attempting to estimate the tropospheric scale-factor error. This will be supported in the real data performance shortly. With the information derived from these simulations, the focus now shifts to real data concerns and implementing the techniques used in simulation thus far to maximize real data performance.

4.4   Real Data Performance

Real data measurement solutions require comparison with an independent source such as DGPS. The remainder of this section describes the DPGS solution as well as the *LocataNet* solutions utilizing the various methods simulated above.

4.4.1 Differential GPS Solutions. During real data runs, two independent GPS receivers provided reference data for comparison with *LocataNet* solutions. Figure 4.25 depicts the antenna placement on the rover vehicle, showing the relative position of the antennas to one another. The antennas were placed on the same horizontal plane on top of the rover vehicle, a Mazda B2200 pickup.
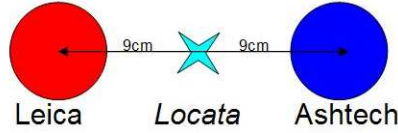

Figure 4.25: Antenna placement for all real test runs

Furthermore, Table 4.1 defines the post-processed accuracy of the Leica and Ashtech GPS receivers utilizing DGPS techniques with carrier-phase measurements [13, 21]. The combination of these independent, post-processed, DGPS solutions provides the "truth" trajectory for comparing *LocataNet* solutions. While these solutions show excellent agreement during the entire run, the table shows some uncertainty still exists in the "truth". Therefore the position solutions provided in the rest of this section signify quality solutions, yet they cannot genuinely be referenced as the true positions and true position errors. However, for this research it will considered the truth reference.

Table 4.1: DGPS accuracies using post-processed carrier-phase measurements

Type	Horizontal	Vertical
Leica Static	3mm + 0.5ppm	6mm + 0.5ppm
Leica Kinematic	1cm + 1ppm	2cm + 1ppm
Ashtech Static	5mm + 1ppm	1cm + 1ppm
Ashtech Kinematic	1cm + 1ppm	2cm + 1ppm

Examining the trajectory more closely shows how the solution relates to the two DGPS solutions, along with the reference truth created by combining the Ashtech and Leica DGPS solutions. Figure 4.26 depicts the start and end of the real data run
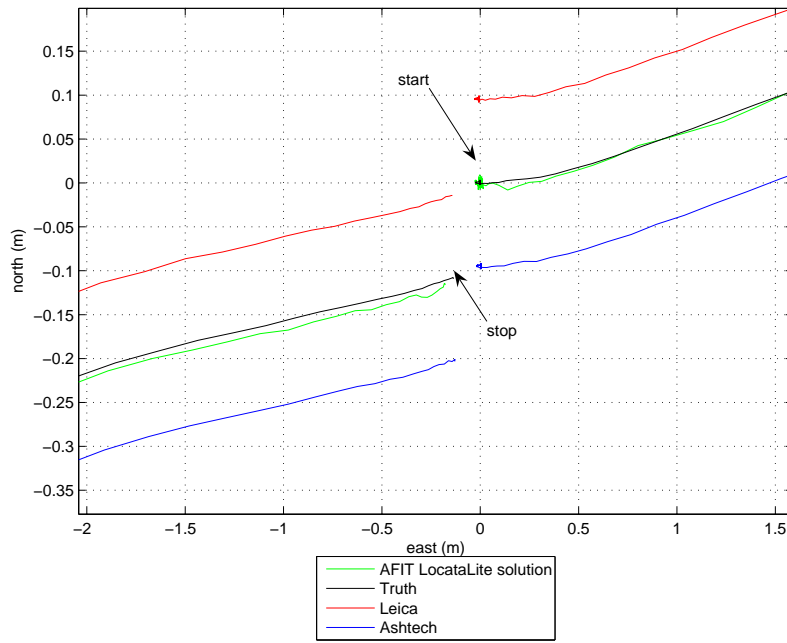
Figure 4.26:   Close up of start/stop position depicting Ashtech and Leica DGPS solutions compared to the AFIT *LocataLite* solution using real measurements and reference truth

and shows excellent agreement between all solutions. Looking forward to Figures 4.30 and 4.31, the largest error occurs during the turnaround point of the run highlighted in Figure 4.27. Even closer inspection of the first turnaround point (and the largest error) reveals the small error between the filter solution and reference truth. Analyzing the other turnaround point in Figure 4.28 renders similar results, even though it corresponds to the poorest geometry as seen in the simulations.
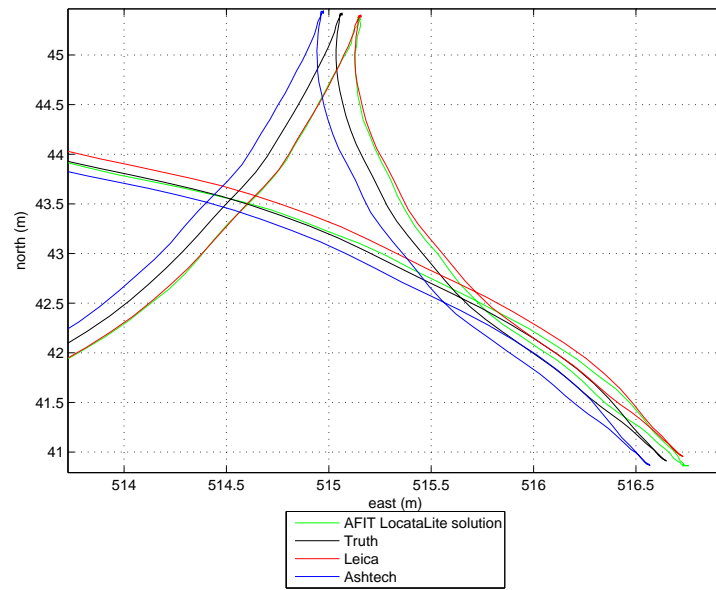
Figure 4.27:   First turnaround point, highlighting largest error using real measurements
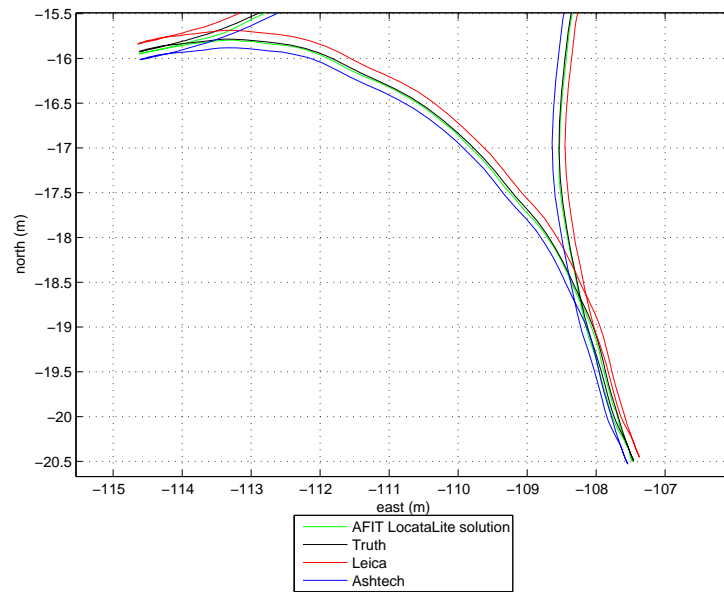

Figure 4.28:   Second turnaround point, corresponding to poorest geometry during testing using real measurements

These figures provide a good indication of how the AFIT *LocataLite* solution compares to the various DGPS solutions offered. Inspecting the position error versus time leads to further error reduction using the tropospheric correction model, the tropospheric scale-factor and *LocataLite* position error techniques explored in simulation.

4.4.2   Solution Error Generation.   In order to compare the real data measurements with DGPS accurately, the time difference between the *LocataNet* solution and the DGPS solution must be resolved. This is accomplished by interpolating the DGPS solution to match the *LocataNet* solution, adjusting for the time bias. In order to check the alignment of the solutions, the velocity is plotted against the error between the solution and the truth reference. From this plot, the timing alignment can be inferred.
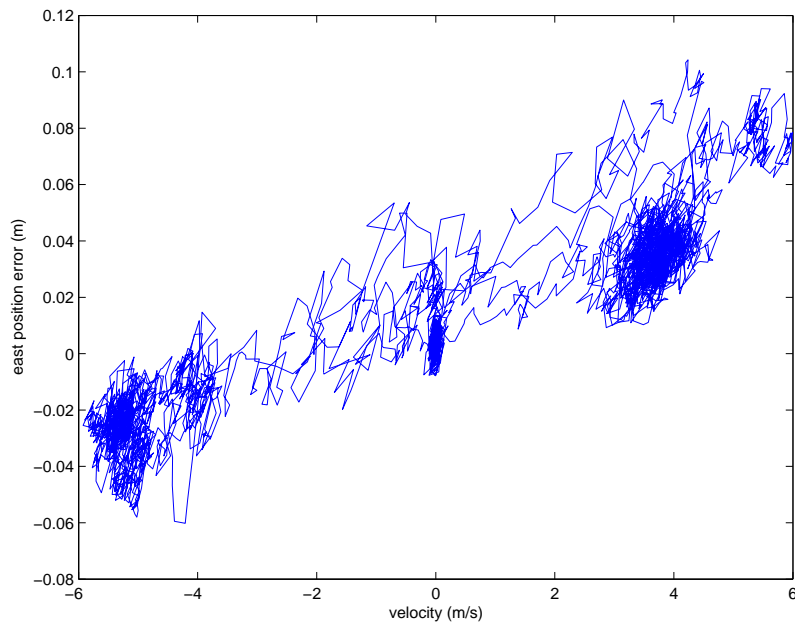

Figure 4.29:   Velocity vs. east position error between AFIT *LocataLite* solution and DGPS

Figure 4.29 depicts an alignment error of 10ms indicated by the general slope of the plot. To correct for this error, a time bias is applied during interpolation of the DGPS solution until the plot shows a zero slope in Figure 4.30.
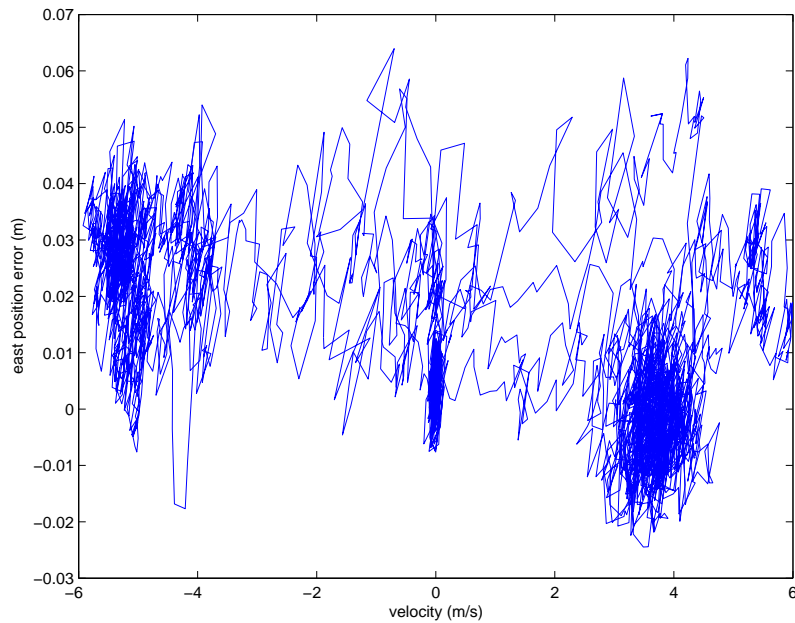

Figure 4.30:   Velocity vs. east position error between AFIT *LocataLite* solution and DGPS, 10ms correction applied

While not perfect, the procedure provides an effective method for time alignment between the two solutions. The corresponding position solution error plots using the altitude information without the tropospheric correction model show results for real measurements. In addition, Figure 4.32 characterizes the overall solution performance via a single figure encompassing the entire error of the AFIT *LocataLite* solution, the horizontal error plot.
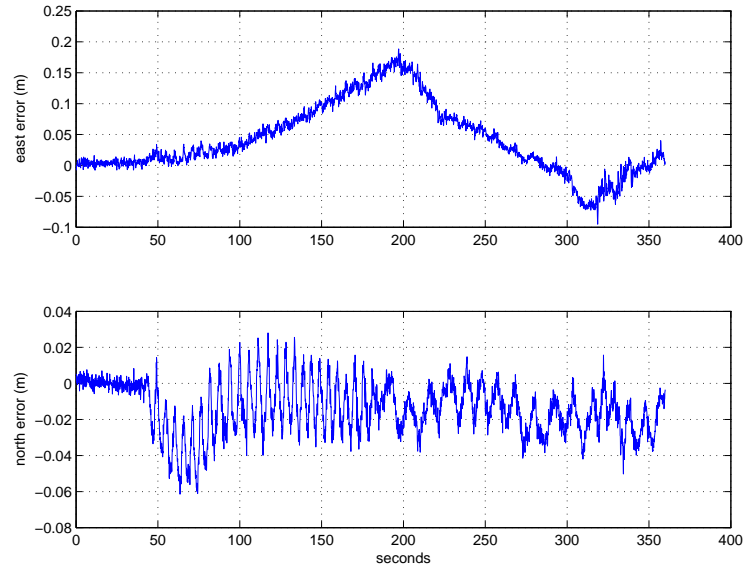
Figure 4.31:   East and north position error of AFIT *LocataLite* solution as compared to DGPS without tropospheric corrections using real measurements
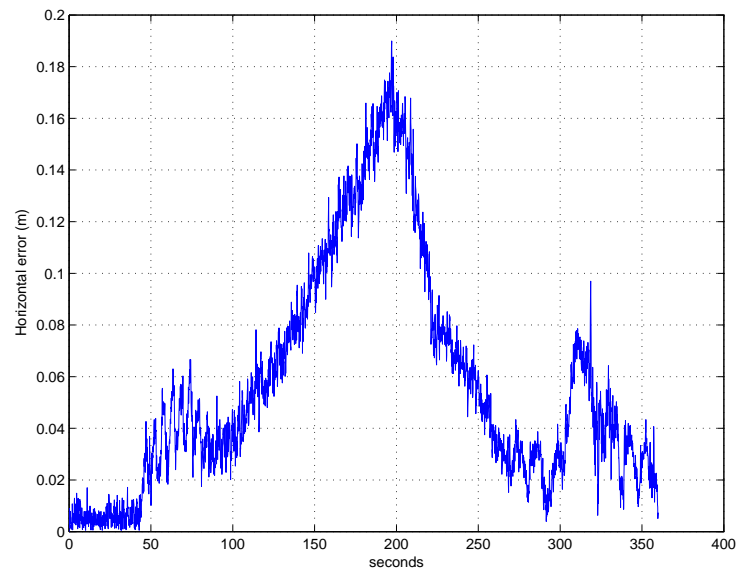

Figure 4.32:   Horizontal error of AFIT *LocataLite* solution as compared to DGPS without tropospheric corrections using real measurements

4-26

Correcting the measurements using the tropospheric correction model detailed in Section 3.2.3 provides much better solutions, shown below in Figures 4.33 and 4.34.

Figure 4.33:   East and north position error for *Locata* generated and AFIT generated solutions as compared to DGPS with tropospheric corrections using real measurements

The *Locata* generated solution depicted in Figures 4.33 and 4.34 was provided from the *Locata* Corporation and represents a post-processed carrier-phase solution with tropospheric corrections via a modified Hopfield model and no measurement differencing. Comparison to this solution provides an independent metric to gauge filter performance.
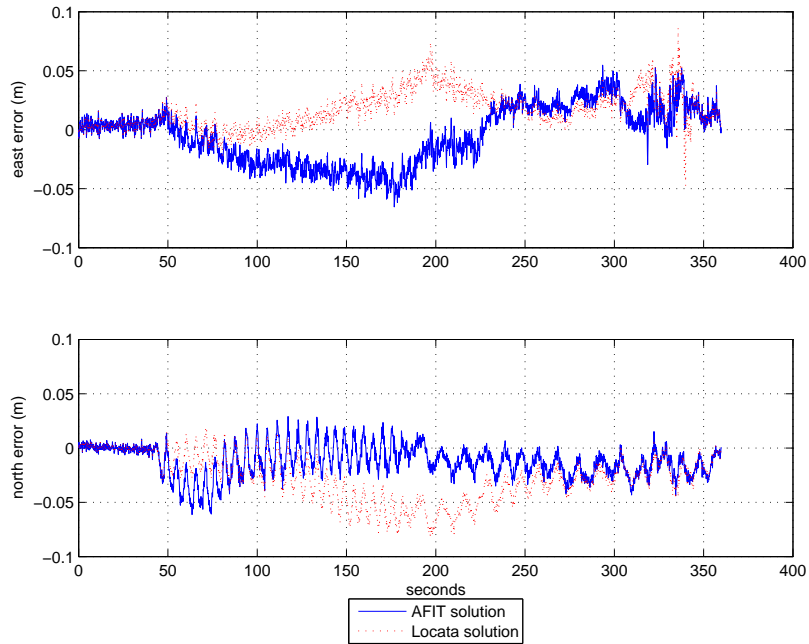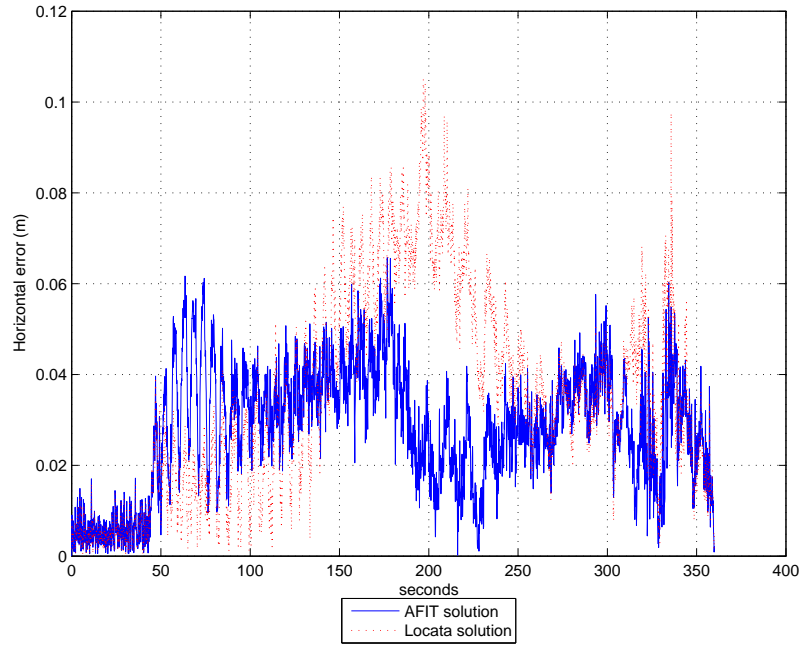
Figure 4.34:   Horizontal error between *Locata* generated and AFIT generated solutions as compared to DGPS with tropospheric corrections using real measurements

The application of the low elevation tropospheric correction model reduces the overall error to just over 6cm in the horizontal error while maintaining values of ±5cm in the east and north respectively. The solid improvement in solution performance justifies the tropospheric correction model, which will receive further validation later in this chapter. Now, given the quality position solution obtained thus far, further error reduction techniques can be applied.

Table 4.5 near the end of this chapter provides the mean and standard deviations for Figures 4.33 and 4.34, as well as the rest of the position error plots throughout this chapter. This permits a purely statistical comparison of the position error plots to supplement the numerous figures.

4.4.3   Tropospheric Scale-Factor State.   The tropospheric scale-factor state attempts to model the remaining tropospheric error not captured using the tropospheric correction model. In simulation, the error state performed very well in the

4-28

noisy environment, able to delineate the additional error in all cases. For real data measurements, Figure 4.35 depicts the remaining tropospheric scale-factor percentage estimated by the filter applying the same tuning parameters of 2×10^{-6} for the process noise (q_t) and 10 percent for the initial standard deviation.
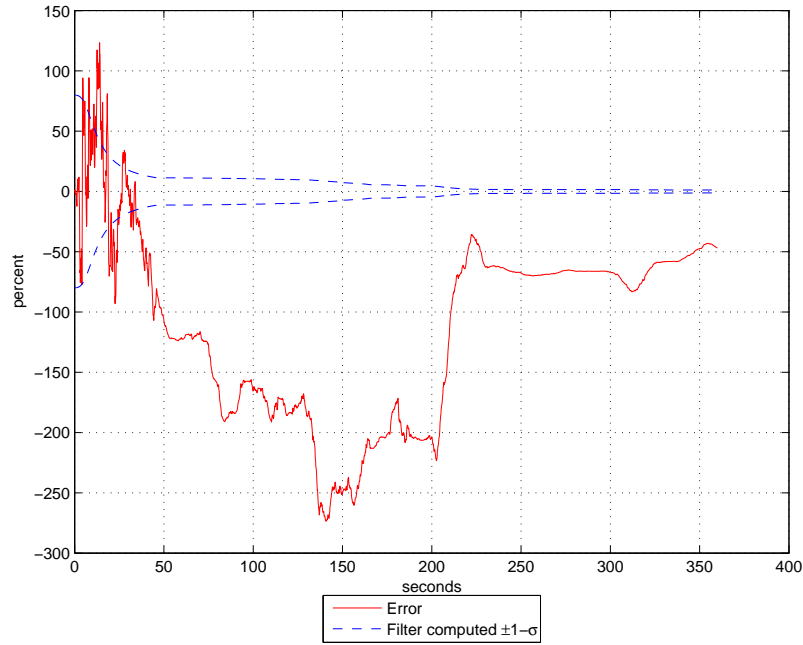
Figure 4.35:   Estimated tropospheric scale-factor percentage with real measurements and initial tuning

This obviously exceeds the maximum of 10 percent expected during simulation. The immediate reaction of increasing the initial standard deviation to 50 percent did not fix this anomaly. The next step included increasing the process noise to allow the filter to compensate for the anomaly. This also did not improve estimation and actually allowed the state to become divergent. No amount of tuning yielded a result with any confidence. Since this error clearly requires more investigation, it will be addressed after correcting the *LocataLite* position errors.

4.4.4   LocataLite Position Error States.   As stated in Section 4.3.3, the indistinguishable position error states (PES) remain at zero to allow proper estimation

of the remaining PES. Figures 4.36 and 4.37 depict the position error estimates for *LocataLites* 2, 3, and 5.
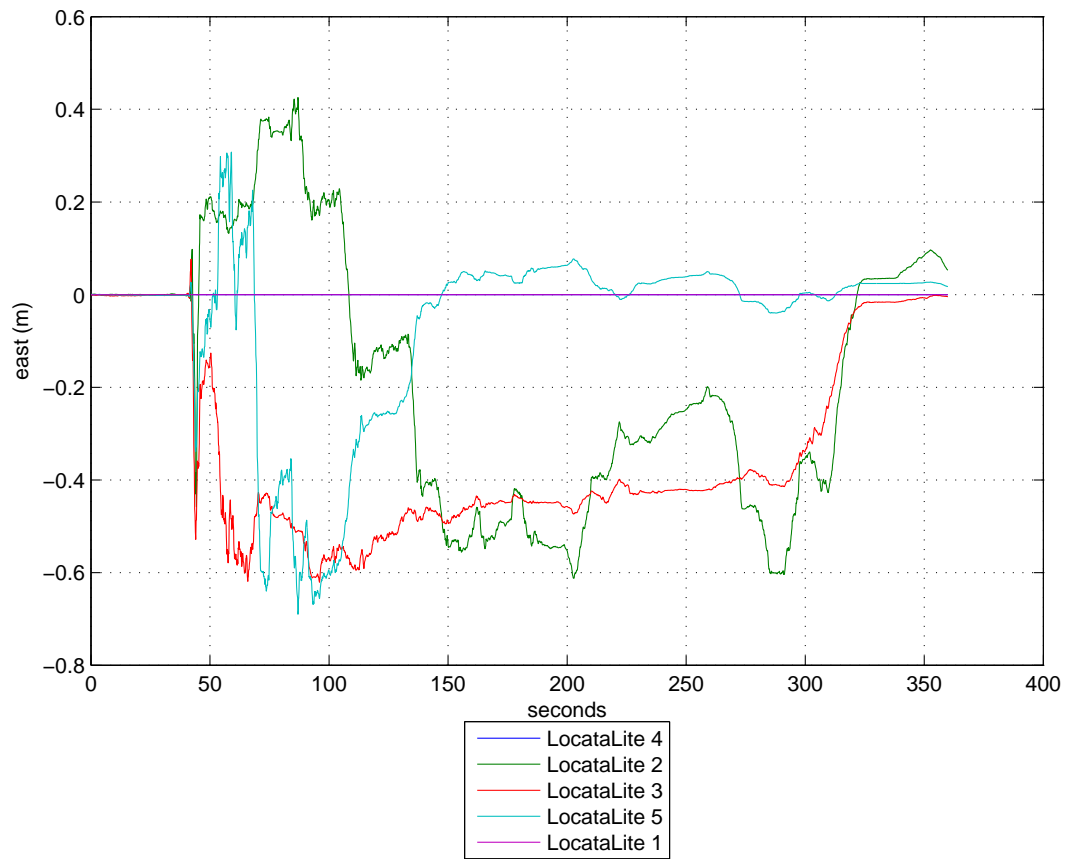
Figure 4.36:   East *LocataLite* position error estimates for *LocataLites* 2, 3, and 5, *LocataLites* 1 and 4 remain at zero, with real measurements
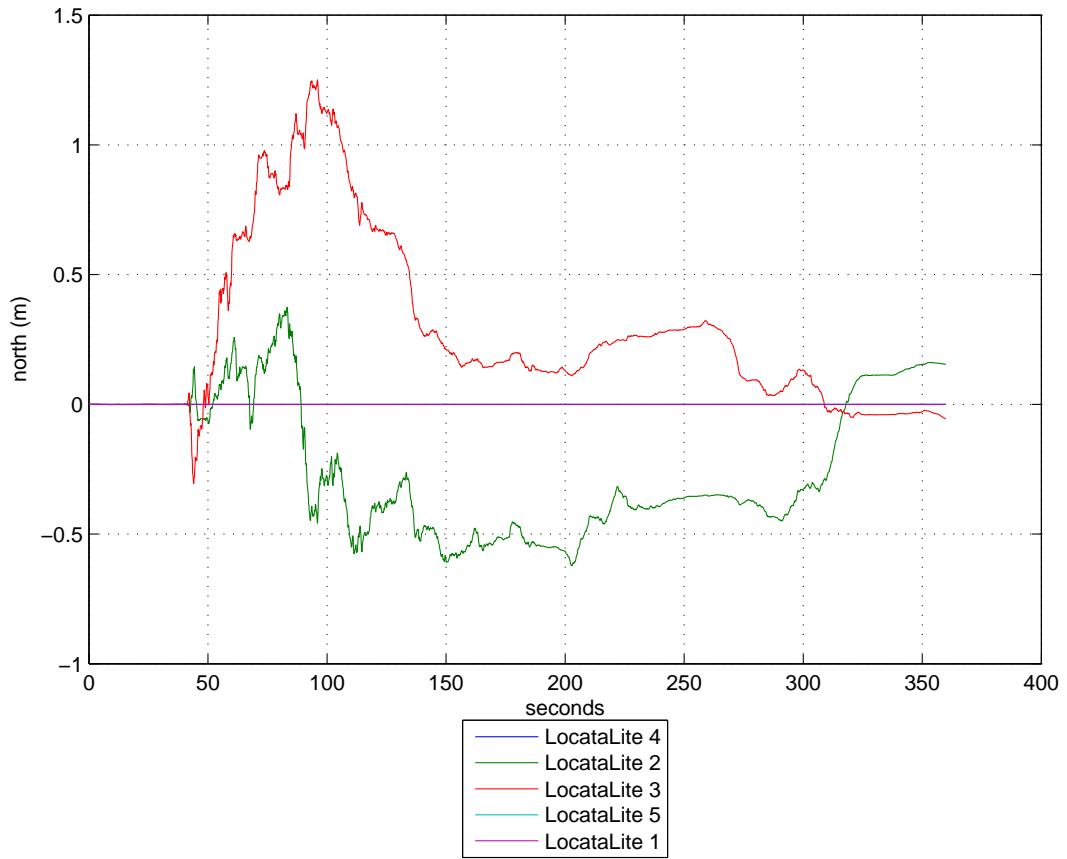
Figure 4.37: North *LocataLite* position error estimates for *LocataLites* 2 and 3, *LocataLites* 1, 4, and 5 remain at zero, with real measurements

The order of the *LocataLite* position errors (4,2,3,5,1) signifies the rank order of measurement quality established before measurements enter the filter. After subsequent runs allowing the filter to find the entire position error, the corrections in Table 4.2 were applied.

Table 4.2: *LocataLite* estimated position errors at end of the run (cm)

LocataLite	East	North	East 1-σ	North 1-σ
2	-5.13379	-14.52001	0.23662	0.40417
3	0.59678	5.16921	0.19721	0.33255
5	-1.87257	0	0.19372	10

This yielded Figures 4.38 and 4.39.

Figure 4.38: East and north position error with real measurements and corrected *LocataLite* positions
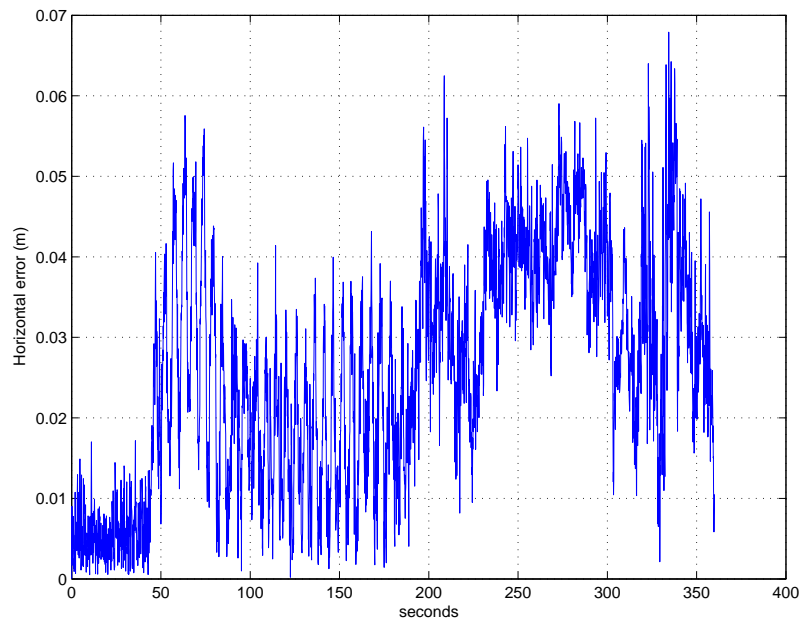
Figure 4.39: Horizontal error with real measurements and corrected *LocataLite* positions

While not drastically improved, close comparison with Figures 4.33 and 4.34 show improvement, especially in the east direction. Since post-pro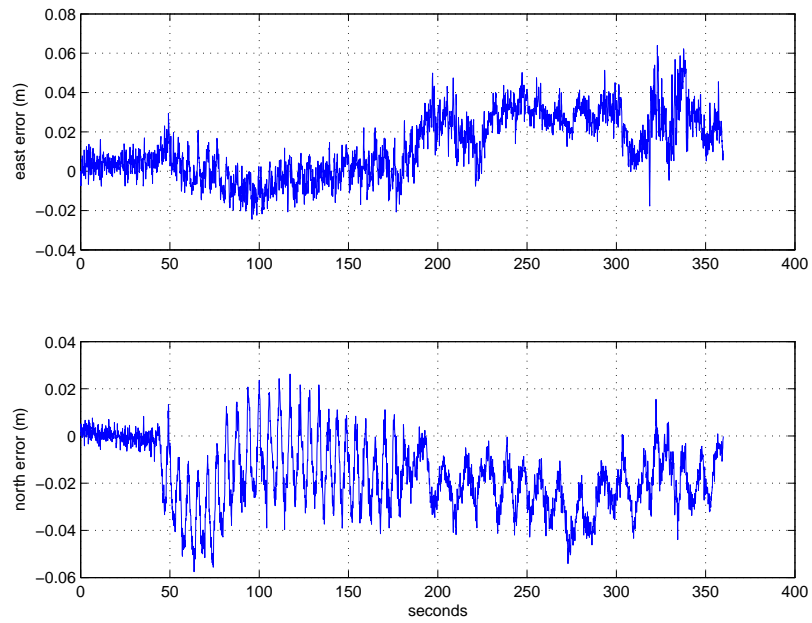cessed static DGPS provides very accurate surveying measurements, these results appear valid. Although a few of the *LocataLite* position error estimates greatly surpass the limits stated in Table 4.1, several factors may contribute to this error. These factors include the antenna placement difference between the GPS used for surveying and the *Locata* used for measurement, human error when making the corrections during placement, and environmental factors such as kangaroos, wombats, and sheep since the antenna bases were not permanently mounted. Therefore some repositioning may have occurred after surveying.

4.4.5   Tropospheric Scale-Factor Revisited.   After applying the position corrections for *LocataLites* 2, 3, and 5, another attempt at estimating the tropospheric

scale-factor was made. This time the filter estimated a value much closer to the expected value from simulations, as seen in Figure 4.40.
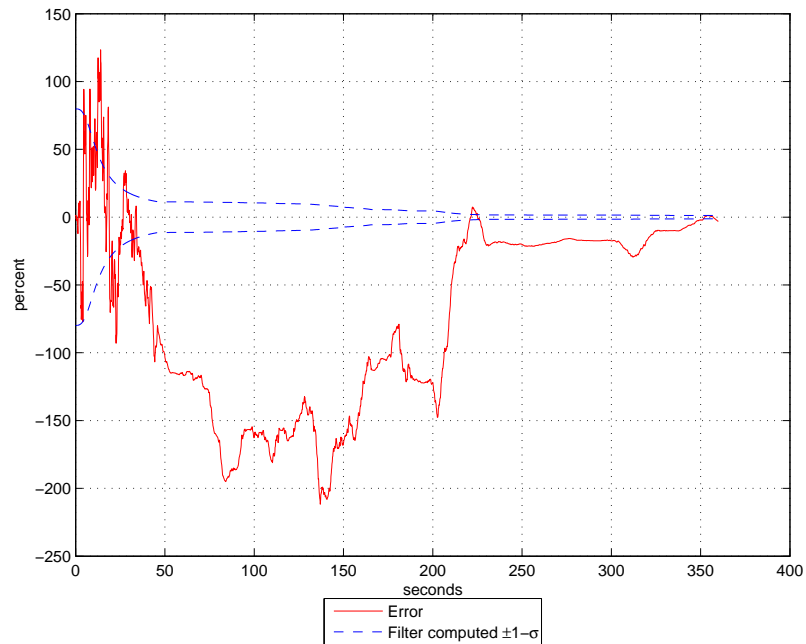
Figure 4.40:   Estimated tropospheric scale-factor percentage with real measurements and corrected *LocataLite* positions

Although a large deviation outside the filter-computed standard deviation exists, this provides a more expected value of 5 percent. This large deviation, seen in both the tropospheric scale-factor estimation and the *LocataLite* position error estimation eludes to an observability problem throughout the test run. This will be addressed later in this chapter. Applying this adjustment to the tropospheric corrections yields
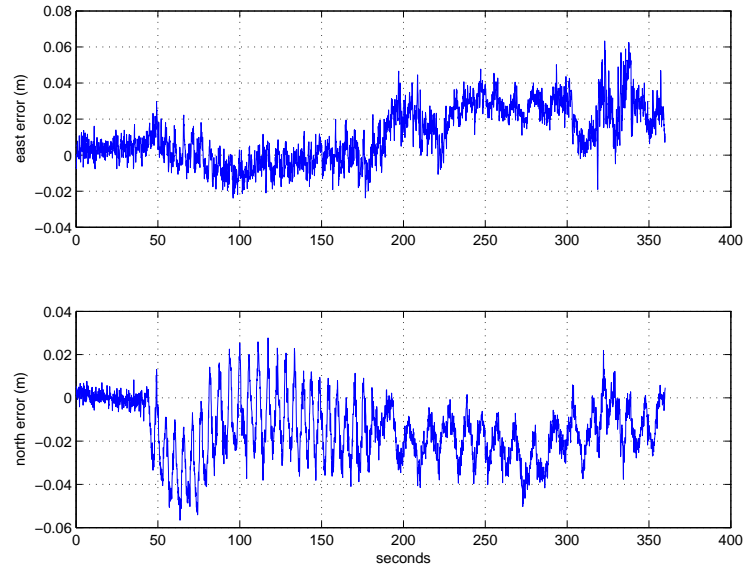
Figure 4.41:   East and north error with real measurements, corrected *LocataLite* positions, and tropospheric corrections adjusted by 5 percent
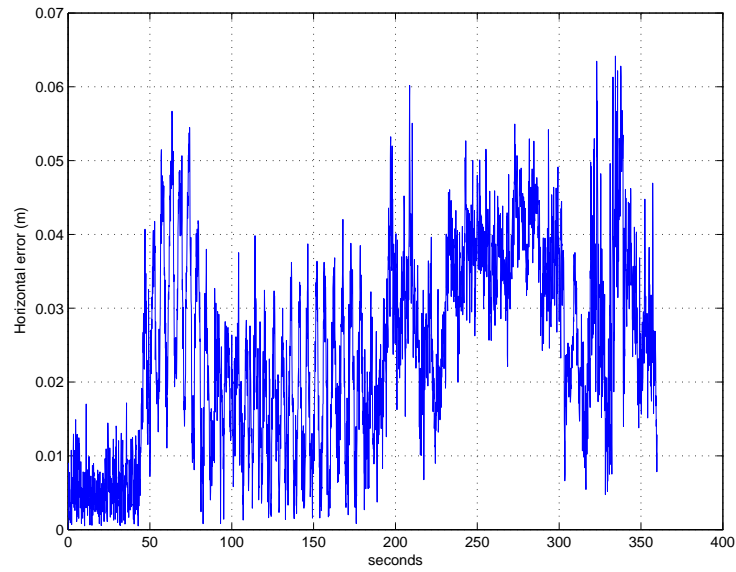
Figure 4.42:   Horizontal error with real measurements, corrected *LocataLite* positions, and tropospheric corrections adjusted by 5 percent

4-35

Figures 4.41 and 4.42. Although the improvement is very minor, this justifies the incorporation of the tropospheric scale-factor state to obtain the additional error not captured by the tropospheric correction model.

As a cursory check, a simulation with known *LocataLite* position errors was performed, attempting to estimate only the tropospheric scale-factor. The results from this simulation closely resembled Figure 4.35 which uses real measurements. This further warrants the estimation of the *LocataLite* position errors as the first error resolution technique to be performed because the tropospheric scale-factor state cannot overcome the inclusion of the *LocataLite* position errors for this scenario.

4.4.6   Tropospheric Scale-Factor and LocataLite Position Errors Simultaneously Estimated.   For completeness, an attempt at resolving all of the postulated errors simultaneously resulted in poor performance as foreseen in simulation. Table 4.3 provides the estimated *LocataLite* corrections, similar in all aspects to Table 4.2.

Table 4.3:   *LocataLite* estimated position errors at end of the run (cm) with simultaneous tropospheric scale-factor estimation

LocataLite	East	North	East 1-σ	North 1-σ
2	-5.99671	-16.26633	0.26173	0.46593
3	0.096462	4.34814	0.20776	0.34625
5	-1.53553	0	0.46856	10

Figures 4.43 and 4.45 closely resemble Figures 4.36 and 4.37, yet Figure 4.45 portrays a tropospheric scale-factor error of 28 percent, with little confidence.
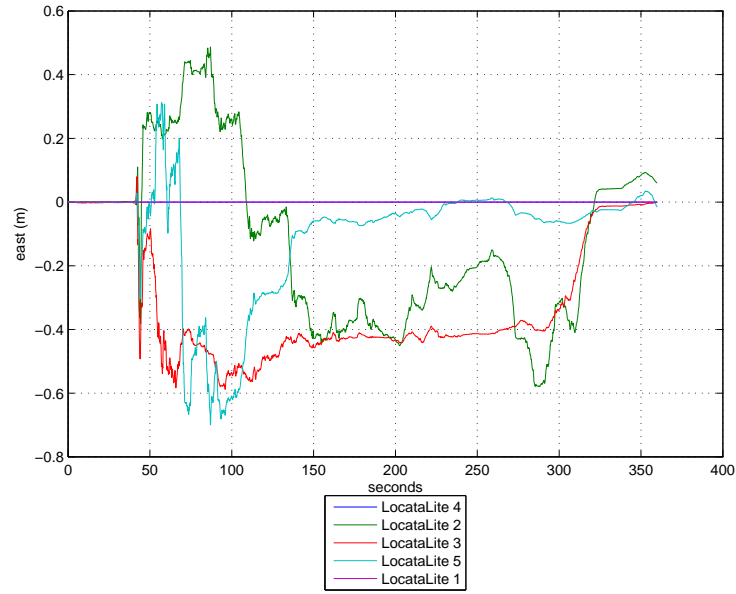
Figure 4.43: East *LocataLite* position error estimates with real measurements and simultaneous tropospheric scale-factor estimation
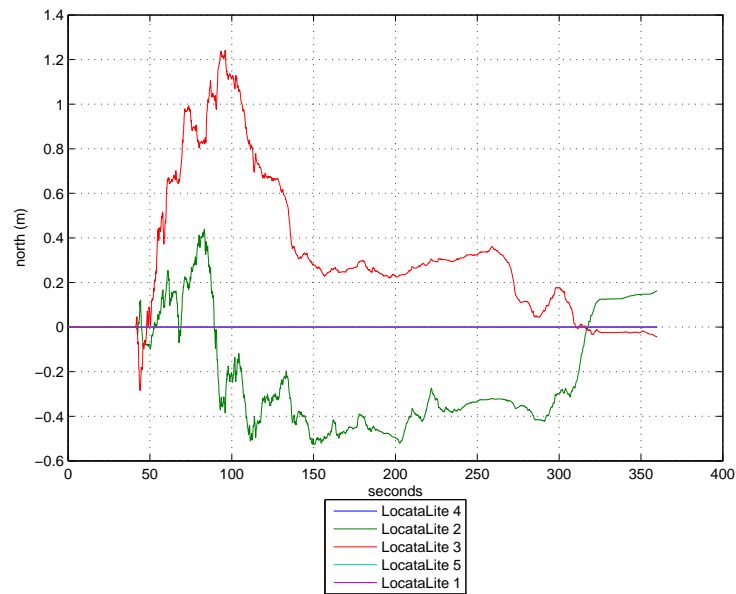
Figure 4.44: North *LocataLite* position error estimates with real measurements and simultaneous tropospheric scale-factor estimation

4-37
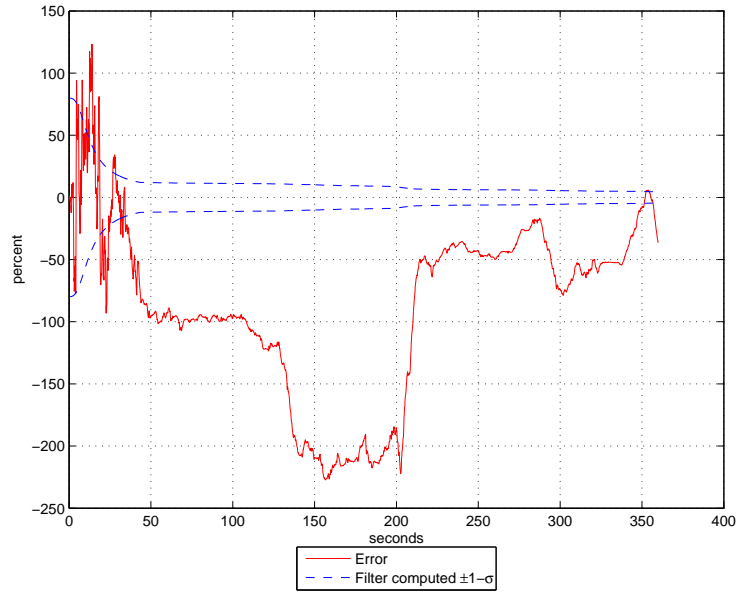
Figure 4.45: Estimated tropospheric scale-factor error with real measurements and simultaneous *LocataLite* position error estimation

Running the filter with these *LocataLite* position errors and the 28 percent adjustment to the tropospheric correction values produced a poor position solution. This promotes resolving the *LocataLite* position errors before attempting to estimate the tropospheric scale-factor. While this constitutes the proper technique for this scenario, test setups with better observability may allow simultaneous estimation.

4.4.7 Alternate Runs. Corroboration of these findings requires investigating more than one measurement run. A quick overview of an alternate run typifies the results found for all alternate runs. The following data represents an alternate run performed under similar conditions on the same test road, within 15 minutes of the run investigated thus far. Figures 4.46, 4.47, and 4.48 show a typical alternate trajectory and the corresponding position error plots.
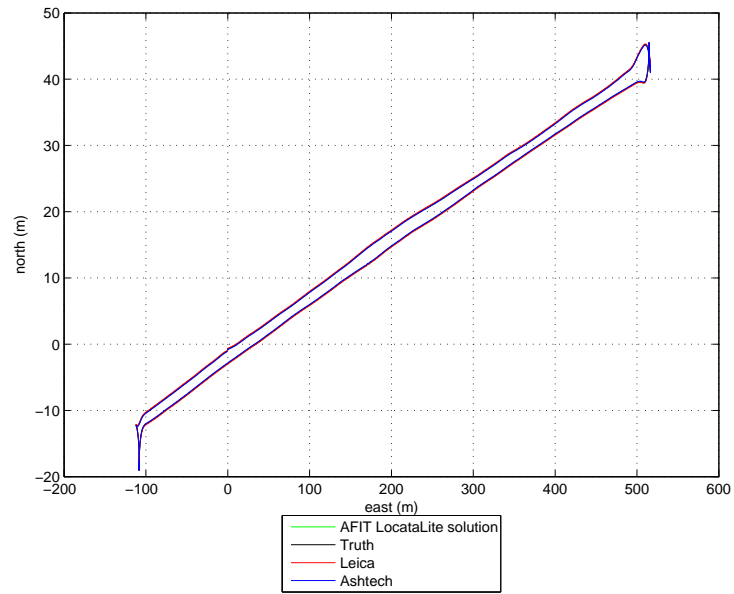
Figure 4.46:   Alternate trajectory with real measurements
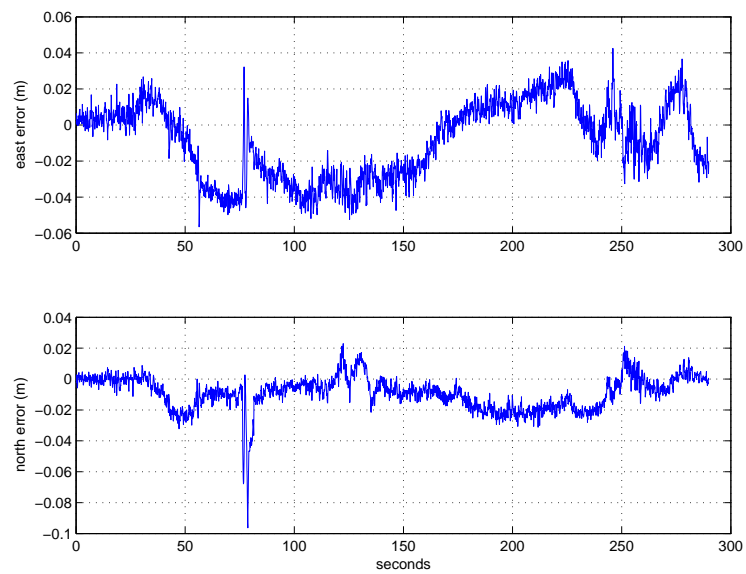
Figure 4.47:   East and north error with real measurements, no *LocataLite* position error state estimation, or tropospheric scale-factor estimation, alternate run

4-39
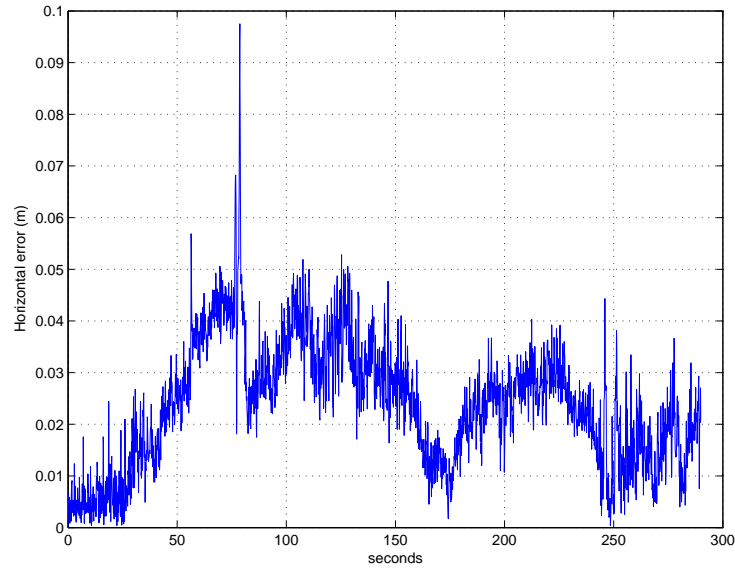
Figure 4.48:   Horizontal error with real measurements, no *LocataLite* position error state estimation, or tropospheric scale-factor estimation, alternate run

Figures 4.46-4.48 signify similar accuracy level and deviations, with the exception of the large spike at approximately 80 seconds into the run. This results from a discrepancy within the SNR measurements, for which the SNR value shows the measurement is good, while closer inspection reveals a cycle slip is still occurring [1]. While important, this detail is not the focus of this research and will not be investigated further.

Since estimating the *LocataLite* position errors was deemed the proper first step, the same technique applied to this alternate run yields the following Figures 4.49 and 4.50.
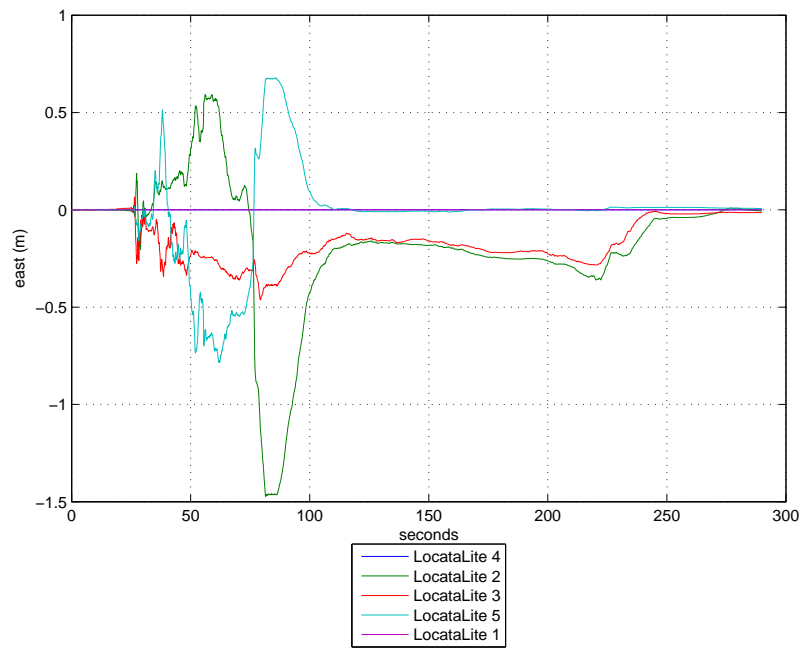
Figure 4.49:   East position error estimates with real measurements, alternate run
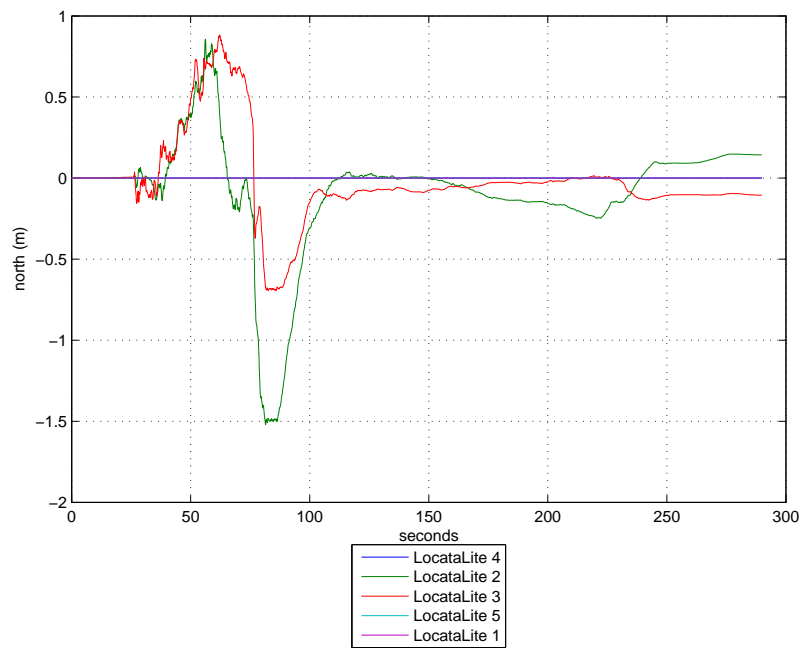
Figure 4.50:   North position error estimates with real measurements, alternate run

4-41

After applying the initial corrections and making a second run, Table 4.3 contains the applied corrections.

Table 4.4:   *LocataLite* estimated position corrections at end of alternate run (cm)

LocataLite	East	North	East 1-σ	North 1-σ
2	.55314	-14.33998	0.19937	0.35396
3	1.42812	10.61069	0.19763	0.30942
5	-0.72241	0	0.16107	10

In comparison to Table 4.2, the values to do not match for all *LocataLites* in all directions. *LocataLite* 2 in the north direction has similar results, but the similarities end there. This distinctly indicates the *LocataLite* position error states are estimating more than the *LocataLite* position errors. Applying these estimates as corrections to the *LocataLite* positions does improve the position solution and allow the estimation of the tropospheric scale-factor state. Therefore their application is merited, but more investigation is required.

Now estimating the tropospheric scale-factor reveals Figure 4.51, and adjusting the tropospheric correction values by the estimated 5.83 percent yields Figures 4.52 and 4.53. Here the comparisons to Figures 4.47 and 4.48 are not as easily discernible. Close inspection exposes that Figure 4.52 contains solutions more closely centered on zero error, but no real reduction in the position error at any point in either direction. However, the process does strengthen the validity of the tropospheric scale-factor percentage since estimates for both runs were very close (5 and 5.83 percent).
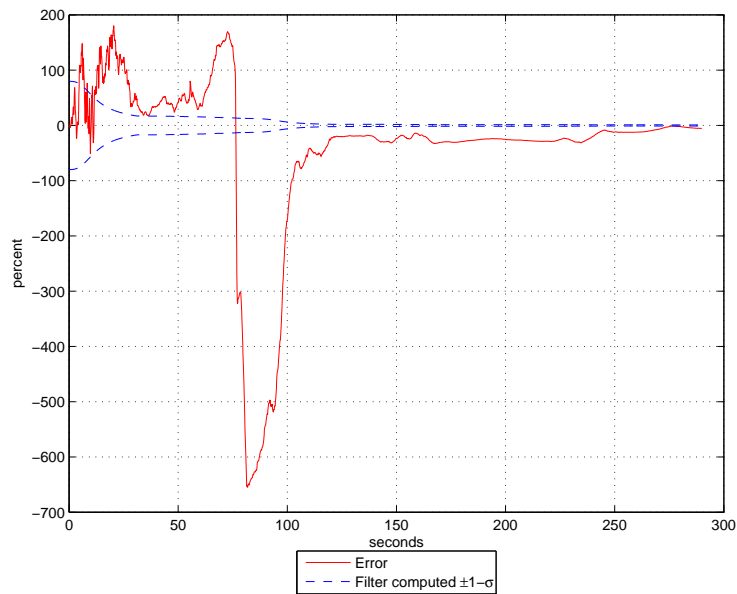
Figure 4.51:   Estimated tropospheric scale-factor with real measurements and *Lo-cataLite* positions corrected, alternate run
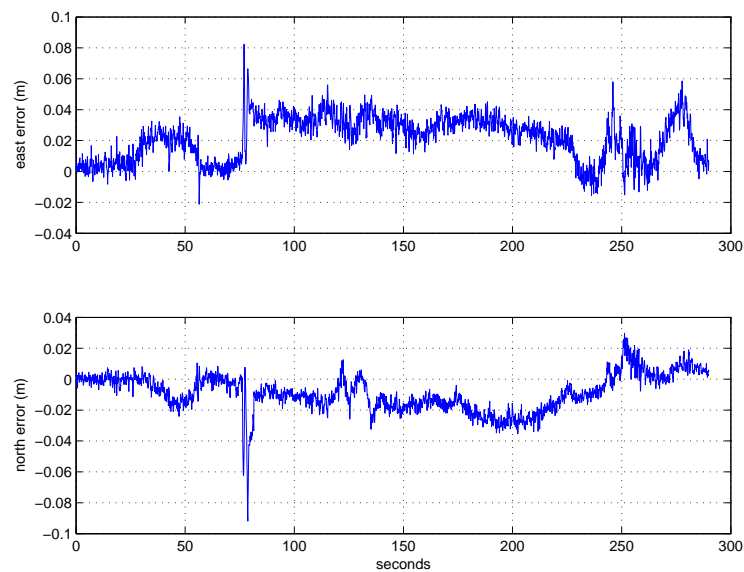
Figure 4.52:   East and north error with real measurements, *LocataLite* positions corrected, and tropospheric corrections adjusted by 5.83 percent, alternate run
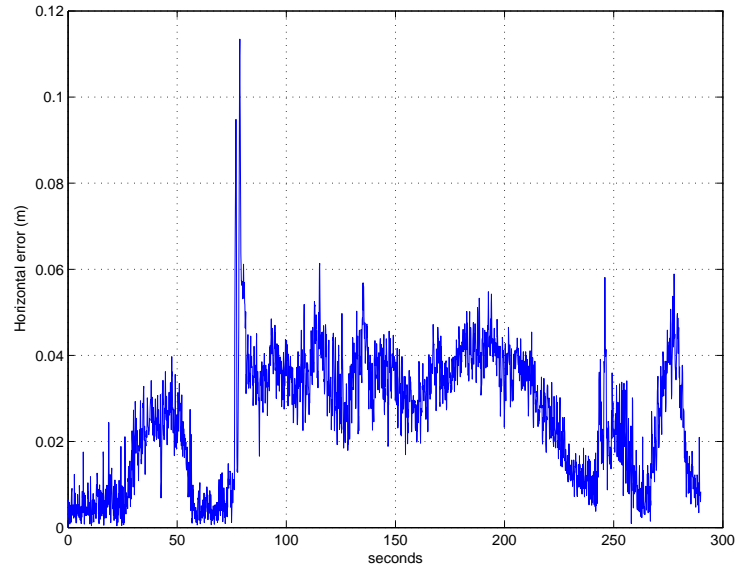
Figure 4.53: Horizontal error with real measurements, *LocataLite* positions corrected, and tropospheric corrections adjusted by 5.83 percent, alternate run

In order to evaluate the many runs and their statistics, Table 4.5 outlines the mean and standard deviations for the multitude of error plots shown. The 2D term signifies the horizontal error, shortened for convenience.

Table 4.5: Temporal statistics for position error plots

Figures	East mean	East 1-σ	North mean	North 1-σ	2D mean	2D 1-σ
4.33, 4.34	-0.44cm	2.44cm	-1.23cm	1.44cm	2.81cm	1.36cm
4.38, 4.39	1.35cm	1.45cm	-1.46cm	1.39cm	2.49cm	1.34cm
4.41, 4.42	1.12cm	1.43cm	-1.45cm	1.39cm	2.43cm	1.33cm
4.47, 4.48	-0.86cm	2.10cm	-0.90cm	1.08cm	2.38cm	1.20cm
4.52, 4.53	2.15cm	1.43cm	-0.89cm	1.19cm	2.60cm	1.45cm

4.4.8   Error analysis.   Throughout the real data sets, the tropospheric scale-factor estimate and the *LocataLite* position error estimates deviate significantly from the expected values before providing near suitable estimates towards the end of the

4-44

run. This deserves an explanation pertaining to the errors and why this happens in real data and not simulation. Equations (3.46) and (3.47) provided the pseudorange and carrier-phase measurement equations with all errors included. Since all solutions employed single-differenced carrier-phase measurements, the error in the carrier-phase measurement (neglecting the white noise term) can be expressed as

$$error_\phi = \lambda^{-1}(\Delta T^{1k}(T_r) + \Delta e_{rec}^{LL^{1k}} \cdot [LL_E^1 - LL_E^k \ LL_N^1 - LL_N^k \ 0]) + \Delta N^{1k} \quad k = 2, 3, \cdots, n$$

(4.2)

where T_r and $[LL_E^1 - LL_E^k \ LL_N^1 - LL_N^k \ 0]$ represent the estimated states in the EKF. Including the time dependence in Equation (4.2) yields

$$error_\phi(t) = \lambda^{-1}(\Delta T^{1k}(t)(T_r) + \Delta e_{rec}^{LL^{1k}}(t) \cdot [LL_E^1 - LL_E^k \ LL_N^1 - LL_N^k \ 0]) + \Delta N^{1k} \quad (4.3)$$

In order for the filter to estimate T_r and $LL_E^1, LL_E^k, LL_N^1, and LL_N^k$ with any confidence, there must be sufficient change in $\Delta T^{1k}(t)$ and $e_{rec}^{LL^{1k}}(t)$. Due to the low dynamics of the rover vehicle during the test runs, this doesn't happen until the second turnaround when the rover heads straight to the start point and maintains a high velocity. Figures 4.36, 4.37, 4.43, and 4.44 show this explicitly starting at approximately 320 seconds, and Figures 4.49 and 4.50 corroborate this for the alternate runs which maintain a high velocity throughout much of the run.

4.5 Measurement Analysis

In order to ascertain the difference between expected and realized performance, a rigorous measurement analysis highlights variants between real measurements used to compute the position solution, and the values the measurements should possess. To conduct this analysis, actual measurements used for position solutions were compared against the corresponding "truth" measurement. This "truth" measurement was comprised of the true range calculated between each *LocataLite* and the DGPS solution as in Equation (4.1), without the T or v terms, then divided by the wavelength. Based upon the accuracy of DGPS over the short baselines involved in this

test, it is estimated that the truth measurement has an accuracy on the order of 1cm ($\approx \frac{1}{12}$ cycle). For measurement comparison, Equation (4.2) describes the difference between real data measurements and the truth measurement:

$$\Delta\phi_{actual} - \Delta\phi_{calc} = \Delta\phi_{diff} \qquad (4.4)$$

where $\Delta\phi_{diff}$ represents the unknown integer ambiguity and all the measurement errors mentioned previously. Therefore the comparison focuses on the *changes* in these external factors and shows any large deviations. Measurements discounted due to poor SNR values are not computed in these values, since they were not used to determine the position solution. However, their location is marked by the red dots which also indicate the re-initialization of the floating-point ambiguities. Figures 4.56-4.59 depict $\Delta\phi_{diff}$ after subtracting the first value in the vector to remove the bias due to the cycle ambiguity.
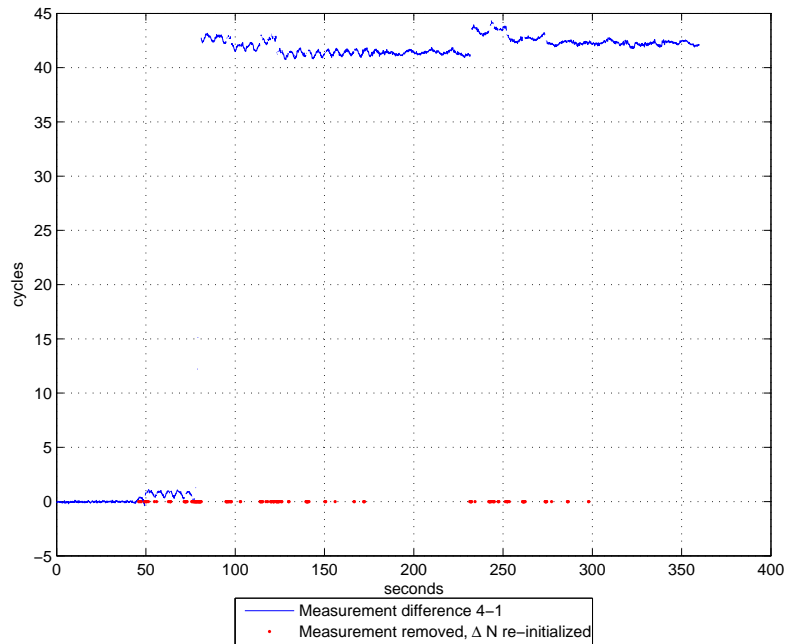
Figure 4.54:   Measurement differences between actual measurements ($\Delta\phi^{41}$) and calculated ranges, ambiguity bias removed
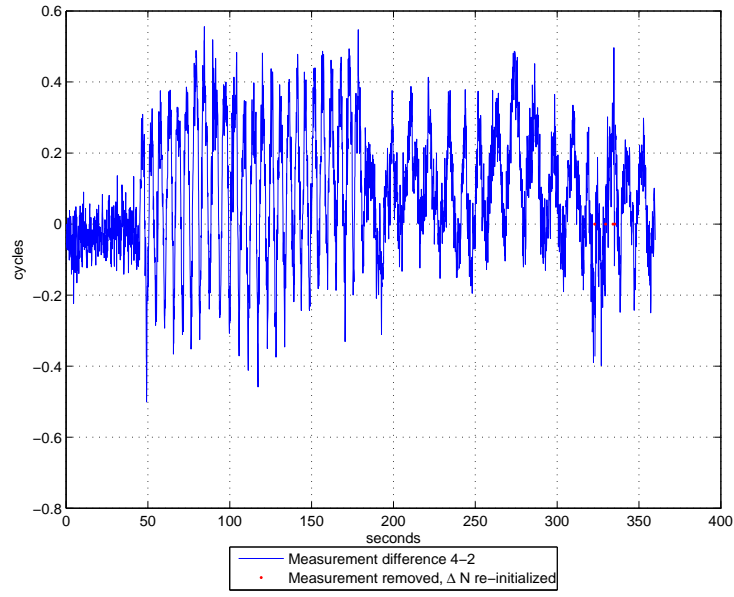
Figure 4.55: Measurement differences between actual measurements ($\Delta\phi^{42}$) and calculated ranges, ambiguity bias removed
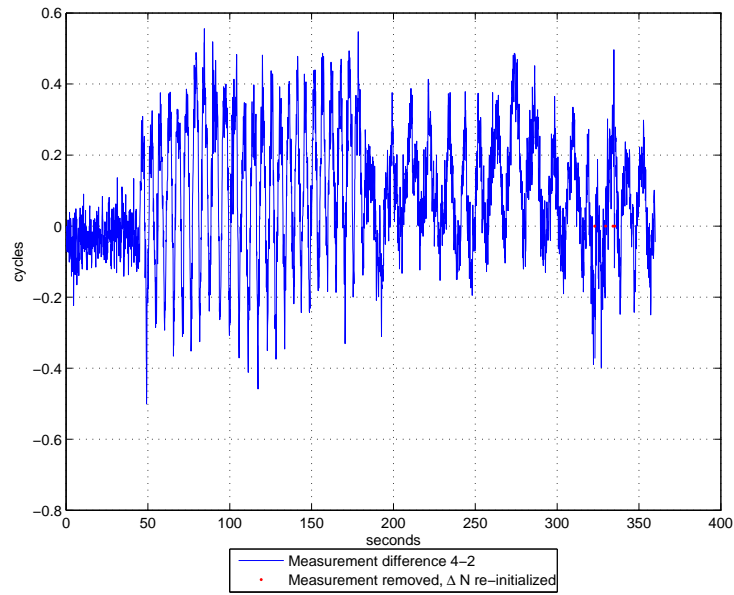
Figure 4.56: Measurement differences between actual measurements ($\Delta\phi^{43}$) and calculated ranges, ambiguity bias removed
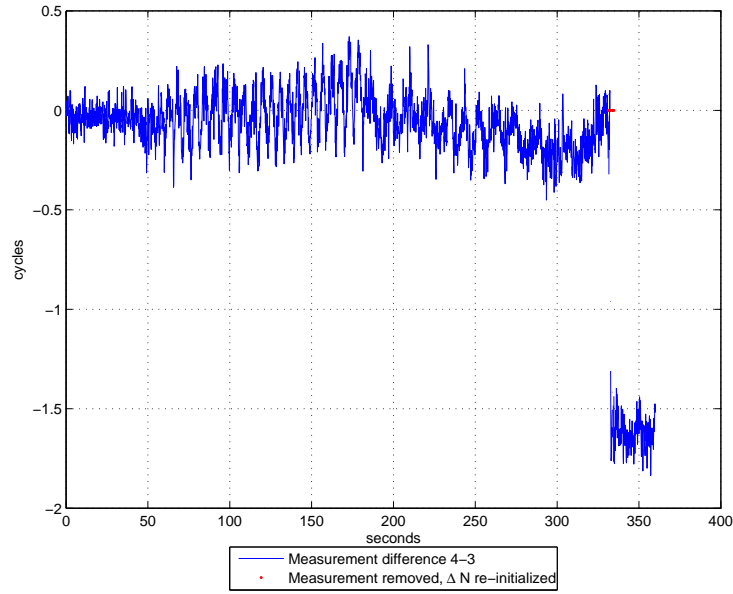
Figure 4.57: Measurement differences between actual measurements ($\Delta\phi^{45}$) and calculated ranges, ambiguity bias removed

Ideally, the difference should be zero or nearly zero for all cases. However the figure clearly shows deviations attributed to large changes in ΔN, yet re-initialization occurs at these transitions to mitigate their effect. These figures distinctly show a relationship between the position errors seen previously and the measurement differences. Additionally, closer inspection of each figure shows a general trend of movement away from the zero line. If an imaginary line were drawn through the center of the difference line, it would be slightly curved. This alludes to phase movement in the measurements, not enough to be labeled a cycle slip, but enough to cause additional measurement error.

Inspecting the accelerations for both the filter-computed and DGPS inferred acceleration renders enlightening results. The acceleration values in the north direction look surprisingly similar to the north position errors. Overlaying the north acceleration and the north position error plots on Figure 4.58 suggest the tracking loop in the receiver is susceptible to acceleration errors.

4-48
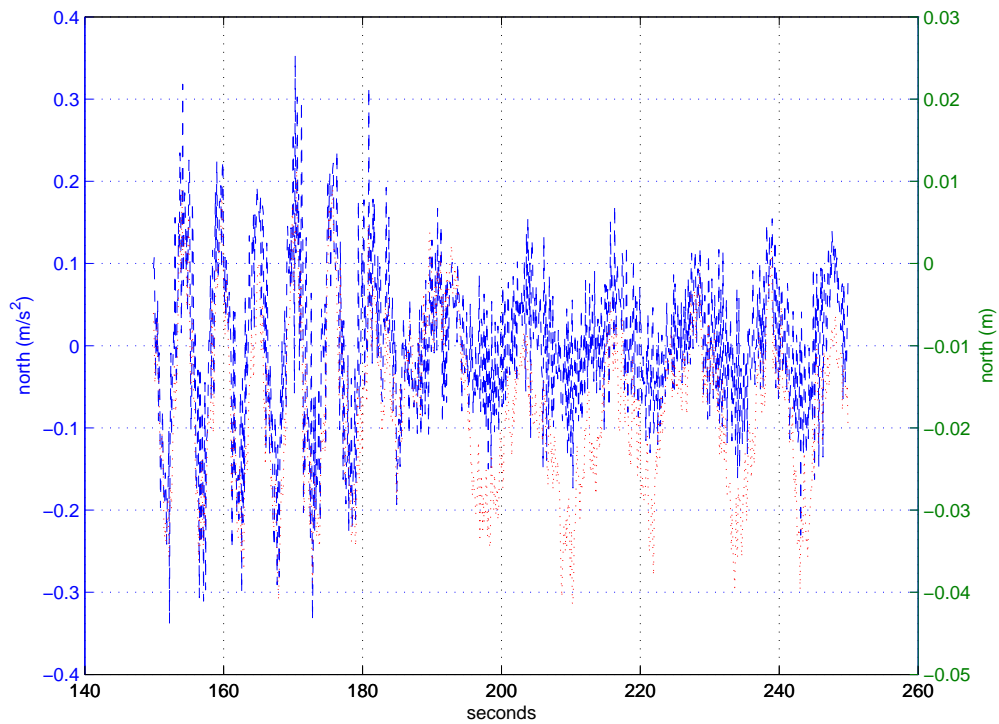
Figure 4.58: Overlay of acceleration (solid blue line) and position error (dotted red line) with respective y-axis values

The tracking control loop allows the receiver to maintain measurement lock during movement. The order and type of the tracking control loop determine the response to different types of input. The order dictates the response characteristics of the tracking control loop, while the type determines the steady-state error characteristics. For the data given, the tracking loop most likely consists of a second-order type-two system with a low bandwidth for smooth response. A type-two system can effectively track the acceleration input, but will always have a steady-state error dependent on the system. This explains the north position error closely resembling the north acceleration. Ultimately, this susceptibility to acceleration signifies the most prominent source of the remaining error for the position solution.

4.6   Summary

This chapter explored the filter confirmation, simulation performance, and real data performance under many scenarios. The simulated and real data sections highlighted the difference in expected and realized values for the tropospheric scale-factor percentage and the *LocataLite* position error states. The greatest discovery for unresolved errors came during measurement analysis by pinpointing the susceptibility to acceleration.

V. Conclusions and Recommendations

5.1   Overview

This research presented the theory, models, simulation results, and real data results for a *LocataLite*-based positioning system. Previous research indicated pseudolites can be used successfully for positioning and ambiguity resolution. This research concentrated on the ability to obtain centimeter level accuracy using the *LocataNet* and resolving the various error sources inherent in the system.

The baseline algorithm consisted of an extended Kalman filter using single-differenced carrier-phase measurements. Filter enhancements included a low elevation tropospheric correction model, a tropospheric scale-factor state, and *LocataLite* position error states.

5.2   Conclusions

A single run of the filter using perfect measurements provided confirmation of all aspects of position solution, tropospheric scale-factor, and *LocataLite* position error state estimation. Filter performance was analyzed using noisy measurements typical of those expected for measurements in the real data environment. Simulations allowed Monte Carlo analysis of postulated errors such as the tropospheric scale-factor and *LocataLite* position error states in a noisy, yet controlled environment.

The floating-point filter yielded position solutions within 1cm under simulated conditions with noisy measurements, altitude aiding, and tropospheric delay corrections applied. This became the baseline solution against which all future simulated and real data solutions were compared. Monte Carlo analysis of the tropospheric scale-factor with a zero mean white Gaussian random variable with 1-σ of 10 percent in the measurements demonstrated excellent ability to estimate the error accurately. Monte Carlo simulations for the *LocataLite* position errors yielded excellent response after examining the filter-computed covariances to determine which *LocataLites* and directions would be distinguishable by the filter. For those deemed indistinguishable,

forcing the states to remain at zero allowed proper estimation of the other *LocataLite* position error states. Simultaneous estimation of the *LocataLite* position errors and the tropospheric scale-factor proved futile, producing poor estimation in all aspects. Additionally, the filter-computed covariances showed little confidence in the estimates.

Filter solutions using real data measurements offered solutions within 6cm of DGPS with measurement correction using the tropospheric correction model from Section 3.2.3. This accuracy was verified by analyzing multiple measurement runs yielding very similar results. Estimating the tropospheric scale-factor generated more questions by producing an estimate quite different from expected. Although disconcerting at first, revisiting this estimation after correcting the positions of the *LocataL-ites* discovered that the gross difference was attributed to the inaccuracies of the *LocataLite* positions. A corresponding simulation of the same environment, estimating the tropospheric scale-factor with *LocataLite* position errors, revealed quite similar estimation performance. From this point on, the *LocataLite* position errors were resolved before attempting tropospheric scale-factor estimation. This information was also substantiated using real measurement data from several runs. This highlights the need to resolve the *LocataLite* position errors before other error analysis is performed. Unfortunately, *LocataLite* position errors encountered in real data runs did not correlate well between measurement runs. This creates an abnormality in which the *LocataLite* position errors are "perceived" due to some unresolved measurement error. Although every effort was made to ensure the positions of the *LocataLites* did not change between measurement runs, there exists some uncertainty. At the time of testing, there existed a temperature controlled crystal oscillator (TCXO) problem which could produce measurement errors depending on wind conditions. This item has since been resolved, but may account for differing *LocataLite* position errors between real data measurement runs. Final measurement analysis revealed the north position error closely resembles the north acceleration, suggesting a susceptibility in the receiver tracking loop to acceleration. This represents a significant portion of the unresolved position error and must be analyzed to refine the position solution.

5.3 Contributions

This thesis provided several contributions advancing techniques in error estimation required for a navigation reference system. The following list identifies these contributions:

- The greatest contribution lies in the validation of the low elevation tropospheric correction model for real data measurements. The inclusion of this model allows tropospheric delay corrections for both positive and negative elevation angles, paramount for the *LocataNet*. This improved the position solution by 12cm for the horizontal position error and delivered the largest melioration for the goal of position accuracy.

- The difficulty of simultaneously evaluating both *LocataLite* position errors and the tropospheric scale-factor was brought to light. In both simulated and real data, attempting to estimate the tropospheric scale-factor with unresolved *LocataLite* position errors caused filter divergence. Without first resolving the *LocataLite* position errors, the filter does not have enough information to distinguish the errors properly, resulting in poor estimates for all.

- Pinpointing the relationship between the acceleration and the position error delivers a fundamental handicap the *Locata* system must overcome to improve accuracy. Since the system ultimately projects using the *LocataNet* for flight testing and landing, a steady-state acceleration error of zero is required.

- Resolving *LocataLite* position errors enhanced accuracy, accounting for errors in DGPS surveying, human factors, and environmental hazards. This also satisfies the conditions needed to resolve the tropospheric scale-factor.

- The tropospheric scale-factor state accounted for errors in the tropospheric correction model, such as observed temperature, pressure, and relative humidity values. The improvement tendered an additional position improvement in some areas and furnished the best overall position solution after accounting for the *LocataLite* position errors.

5-3

5.4   Recommendations

The filter in this research performed very well in resolving *LocataLite* position errors and the tropospheric scale-factor in simulation. The real data performance left unresolved errors and motivates further research in resolving the persisting error difference between the AFIT *LocataLite* solution and DGPS. The following recommendations offer suggestions for future endeavors.

- Increase the number of *LocataLites* available for positioning, paying particular attention to the geometry of the setup. Depending on the terrain, vertical placement will be the most challenging since very tall towers represent a logistical and environmental challenge. The greater the height of the tower, the more susceptible to wind conditions and surveying errors it will become. Since the ultimate goal targets landing scenarios, the placement of such towers will pose additional concerns near the proximity of the runway. However, this will help alleviate the need for altitude aiding and establish the *LocataNet* as a stand-alone system.

- Widen the test range to allow testing using aircraft flight trajectories. This will vastly improve the geometry and permit investigation into other errors, unobtainable in this research. However, the susceptibility to acceleration in the receiver tracking loop must be resolved first.

- Specific testing of the *LocataLite* position error estimation capability within a controlled environment and known position errors. Careful attention to surveying position and accuracy between DGPS and the *LocataNet* would allow known position errors to be induced during real data measurements. Optimally, the *LocataNet* would allow all *LocataLites* in all directions to be distinguishable.

- Implement a Multiple Model Adaptive Estimation (MMAE) algorithm for determining position solutions. Since trajectories and dynamics can vary greatly, an MMAE algorithm would provide solution robustness without retuning the filter for specific situations.

- Develop a method to detect cycle slips for carrier-phase measurements to replace the use of SNR measurements for measurement quality determination. This will increase measurement accuracy and ultimately, position accuracy.

- Incorporate an optimal smoother to help resolve the *LocataLite* position errors and tropospheric scale-factor. This may allow the simultaneous estimation which was unsuccessful in this research and supplant the ad-hoc technique used.

Bibliography

1. Amt, John. *Methods For Aiding Height Determination In Pseudolite-Based Reference Systems Using Batch Least-Squares Estimation*. MS thesis, AFIT/GE/ENG/06-03, Air Force Institute of Technology, March 2006.

2. Barnes, Joel, Rizos Chris Kanli Mustafa. "Indoor industrial machine guidance using Locata: a pilot study at BlueScope Steel," *Proceedings of the 2004 Annual Meeting of the ION* (Dayton, OH, June 2004).

3. Barnes, Joel, Rizos Chris Wang Jinling. "Locata: A New Positioning Technology for High Precision Indoor and Outdoor Positioning," *Proceedings of ION GPS/GNSS 2003* (Portland, OR, September 2003).

4. Bouska, Terry J, Raquet John F. "Tropospheric Model Error Reduction in Pseudolite-Based Positioning Systems," *Proceedings of ION GPS/GNSS 2003* (Portland, OR, September 2003).

5. Bouska, Terry J., Raquet John F. Maybeck Peter S. "The Use of Optimal Smoothing and Nonlinear Filtering in Pseudolite-Based Positioning Systems," *Proceddings of the 2003 Annual Meeting of the ION* (Albuquerque, NM, June 2003).

6. Bouska, Terry L. *Development and Simulation of a Pseudolite-Based Flight Reference System*. MS thesis, AFIT/GE/ENG/03-03, Air Force Institute of Technology, March 2003.

7. Brown, Alison, Van Diggelen Frank Kelecy Thomas. "Flight Test Results Using Carrier Phase Kinematic Solutions for Aircraft Precision Approach and landing," *SPN*, *1*:19–27 (1995).

8. Changdon, Kee. "Precise Calibration of Pseudolite Positions in Indoor Navigation System," *Proceedings of ION GPS-95* (Anaheim, CA, September 1995).

9. Chen, D. "Fast Ambiguity Search Filter (FASF): A Novel Concept for GPS Ambiguity Resolution," *Proceedings of ION GPS-93* (Salt Lake City, UT, September 1993).

10. Cobb, H. Stewart. "Precision Landing Tests with Improved Integrity Beacon Pseudolites," *Proceedings of ION GPS-95* (Palm Springs, CA, September 1995).

11. Dai, Liwen. "Pseudolite applications in positioning and navigation: Modeling and geometric analysis," *Proceedings of ION GPS-2001*, 482–489 (Salt Lake City, UT, September 2001).

12. Fukushima, S., Yoshihara T. Suga S. "Evaluation of a Tropospheric Correction Model for Airport Pseudolite," *Proceedings of ION GNSS-2004* (Long Beach, CA, September 2004).

13. Geosystems, Leica. *Leica GPS1200 Technical Data*. Leica Geosystems AG, 2005.

14. Hebert, Jeffrey M. *Velocity Determination for an Inverted Pseudolite Navigation Reference System*. MS thesis, Air Force Institute of Technology, 1995.

15. Henzler, Jens, Weiser Martin. "Using Pseudolites as a Flightlanding System," *Proceedings of the 1999 Annual Meeting of the ION* (Cambridge, MA, June 1999).

16. Lee, Hung Kyu, Wang Jinling Rizos Chris Barnes Joel. "Analysis of Pseudolite Augmentation for GPS Airborne Applications," *Proceedings of ION GPS-2002* (Portland, OR, September 2002).

17. Maybeck, Peter S. *Stochastic Models, Estimation, and Control, Volume 1, 141-1*. Mathematics in Science and Engineering. Arlington, Virginia: Navtech Book and Software Store, 1994.

18. Maybeck, Peter S. *Stochastic Models, Estimation, and Control, Volume 2, 141-2*. Mathematics in Science and Engineering. Arlington, Virginia: Navtech Book and Software Store, 1994.

19. Misra, Pratap and Per Enge. *Global Positioning System Signals, Measurements, and Performance* (First Edition). Ganga-Jamuna Press, 2001.

20. Monda, Eric W., Lightsey E. Glenn Key Kevin. "An Investigation of GPS Pseudolite Based Relative Navigation," *American Astronautical Society, 03-529* (2003).

21. Navigation, Thales. *Z-Xtreme Survey System*. Thales Navigation, Inc, Santa Clara, CA, 471 El Camino Real, Santa Clara, CA 95050, 2001.

22. Ndili, Awele. "GPS Pseudolite Signal Design," *Proceedings of ION GPS-94* (Salt Lake City, UT, September 1994).

23. Raquet, John F. *Class notes to EENG 533*. Air Force Institute of Technology.

24. Raquet, John F. *Class notes to EENG 633*. Air Force Institute of Technology.

25. Raquet, John F., Lachapelle G. Qiu W. and C. Pelletier. "Development and Testing of a Mobile Pseudolite Concept for Precise Positioning," *NAVIGATION: Journal of the Institute of Navigation, 43*:149–165 (1996).

26. Stone, Jonathan M., LeMaster Edward A. Powell J. David Rock Stephen. "GPS Pseudolite Transceivers and their Applications," *Proceedings of the 1999 National Technical Meeting of ION* (San Diego, CA, January 1999).

27. Teunissen, P. "The Least-Squares Ambiguity Decorrelation Adjustment: A Method for Fast GPS Integer Ambiguity Estimation," *Journal of Geodesy, Springer-Verlag, 70*:65–82 (1995).

28. Van Dierendonck, A.J. *Local Differential Tropospheric Delay Corrections*. Technical Report, Internal Memo for RTCA Special Committee 159 Working Group 4, August.

29. Zhang, JiHong. *Investigations into the Estimation of Residual Tropospheric Delays*. MS thesis, University of Calgary, 1999.

7

Vita

Captain Jeremiah A. Shockley grew up in Holdenville, Oklahoma where he graduated Valedictorian from Holdenville High School and married his wife in 1992. He enlisted in the US Air Force as a Communications-Computer Systems operator and received his first assignment to Hickam AFB, Hawaii. While in Hawaii he attended Hawaii Pacific University.

After three years he received an assignment to Scott AFB, IL, where he attended Belleville Area College. During this assignment he welcomed the birth of his daughter, and was awarded acceptance into the Airman's Education and Commissioning Program (AECP).

This program allowed him to complete his undergraduate studies at the University of Oklahoma in Norman, Oklahoma where he graduated with a Bachelor of Science Degree in Electrical Engineering in 2000. He received his commission through Officer Training School (OTS) at Maxwell AFB, Alabama later that year.

His next assignment at Yokota AB, Japan, included three years of radio frequency (RF) engineering and design for the 315 Intelligence Squadron. An assignment to Maxwell-Gunter AFB as a Network Engineer for one year allowed time to apply for a graduate program. In September 2004 he entered the Graduate School of Engineering and Management, Air Force Institute of Technology. Upon graduation, he will be assigned to the 746th Test Squadron, 46th Test Group, Holloman AFB, NM where he will continue work with GPS and pseudolite navigation systems.

Permanent address: 2950 Hobson Way
Air Force Institute of Technology
Wright-Patterson AFB, OH 45433

VITA-1

REPORT DOCUMENTATION PAGE

Form Approved
OMB No. 0704–0188

The public reporting burden for this collection of information is estimated to average 1 hour per response, including the time for reviewing instructions, searching existing data sources, gathering and maintaining the data needed, and completing and reviewing the collection of information. Send comments regarding this burden estimate or any other aspect of this collection of information, including suggestions for reducing this burden to Department of Defense, Washington Headquarters Services, Directorate for Information Operations and Reports (0704–0188), 1215 Jefferson Davis Highway, Suite 1204, Arlington, VA 22202–4302. Respondents should be aware that notwithstanding any other provision of law, no person shall be subject to any penalty for failing to comply with a collection of information if it does not display a currently valid OMB control number. **PLEASE DO NOT RETURN YOUR FORM TO THE ABOVE ADDRESS.**

1. REPORT DATE *(DD–MM–YYYY)*	2. REPORT TYPE	3. DATES COVERED *(From — To)*
23–03–2006	Master's Thesis	Sept 2004 — Mar 2006

4. TITLE AND SUBTITLE

ESTIMATION AND MITIGATION
OF UNMODELED ERRORS FOR A
PSEUDOLITE BASED REFERENCE SYSTEM

5a. CONTRACT NUMBER

DACA99–99–C–9999

5b. GRANT NUMBER

5c. PROGRAM ELEMENT NUMBER

6. AUTHOR(S)

Jeremiah A. Shockley, Capt, USAF

5d. PROJECT NUMBER

5e. TASK NUMBER

5f. WORK UNIT NUMBER

7. PERFORMING ORGANIZATION NAME(S) AND ADDRESS(ES)

Air Force Institute of Technology
Graduate School of Engineering and Management
2950 Hobson Way
WPAFB OH 45433-7765

8. PERFORMING ORGANIZATION REPORT NUMBER

AFIT/GE/ENG/06-51

9. SPONSORING / MONITORING AGENCY NAME(S) AND ADDRESS(ES)

746th Test Squadron AFMC
Capt Terry Bouska
1644 Vandergrift Rd
Holloman AFB, NM 88330
Comm: (505) 679-1772 DSN:349-1771

10. SPONSOR/MONITOR'S ACRONYM(S)

11. SPONSOR/MONITOR'S REPORT NUMBER(S)

12. DISTRIBUTION / AVAILABILITY STATEMENT

Approval for public release; distribution is unlimited.

13. SUPPLEMENTARY NOTES

14. ABSTRACT

Current flight reference systems rely heavily on the Global Positioning System (GPS), causing susceptibility to GPS jamming. Additionally, an increasing number of tests involve jamming the GPS signal. A need exists to develop a system capable of GPS-level accuracy during these outages. One promising solution is a ground-based pseudolite system capable of delivering sub-centimeter level accuracy, yet operating at non-GPS frequencies. This thesis attempts to determine the unknown errors in the *Locata* system, one such pseudolite-based system, to achieve the accuracy required. The development of a measurement simulation tool along with a Kalman filter algorithm provides confirmation of filter performance as well as the ability to process real data measurements and evaluate simulated versus real data comparatively. The simulation tool creates various types of measurements with induced noise, tropospheric delays, pseudolite position errors, and tropospheric scale-factor errors. In turn, the Kalman filter resolves these errors, along with position, velocity, and acceleration for both simulated and real data measurements, enabling error analysis to pinpoint

15. SUBJECT TERMS

Pseudolite, *LocataLite*, Global Positioning System, GPS, Differential Global Positioning System, DGPS, Kalman Filter, Nonlinear Filtering, Tropospheric Delay

16. SECURITY CLASSIFICATION OF:			17. LIMITATION OF ABSTRACT	18. NUMBER OF PAGES	19a. NAME OF RESPONSIBLE PERSON
a. REPORT	b. ABSTRACT	c. THIS PAGE			Raquet, John F., Ph.D., AFIT
U	U	U	UU	137	**19b. TELEPHONE NUMBER** *(include area code)* (937) 255–3636, ext 4580

Standard Form 298 (Rev. 8–98)
Prescribed by ANSI Std. Z39.18